CHALMERS

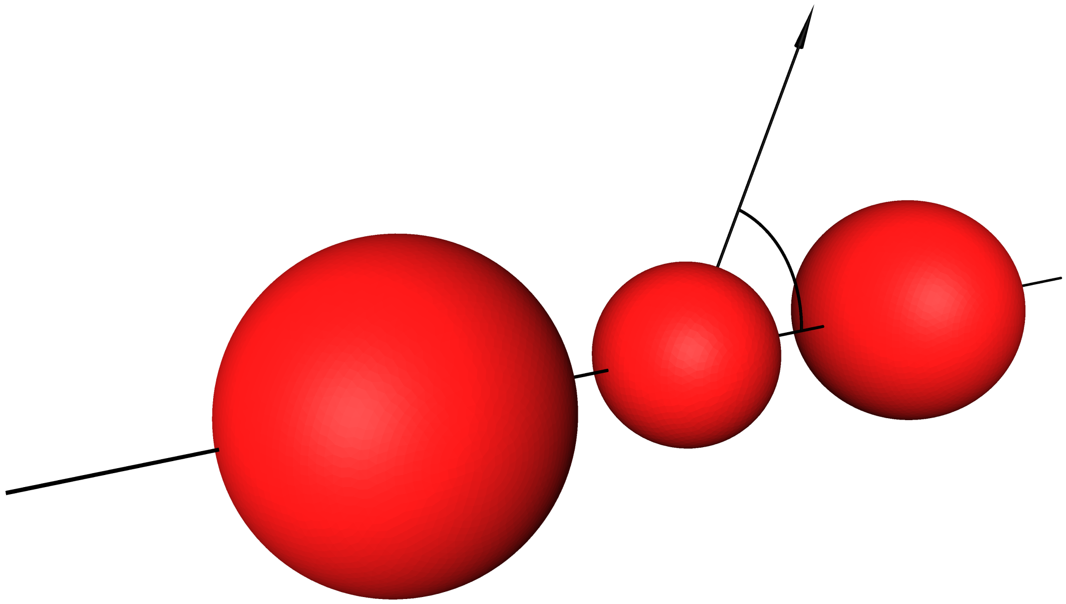

Experimental and theoretical refutation of Collinear Cluster Tri-partition

Thesis for the degree of Master of Science in Physics

PATRIC HOLMVALL

Department of Fundamental Physics
Subatomic Physics Group
CHALMERS UNIVERSITY OF TECHNOLOGY
Gothenburg, Sweden 2014

THESIS FOR THE DEGREE OF MASTER OF SCIENCE IN PHYSICS

Experimental and theoretical refutation of Collinear Cluster Tri-partition

PATRIC HOLMVALL

INSTITUT LAUE-LANGEVIN
Supervisor:
Dr. Ulli Köster

CHALMERS
Examiner:
Prof. Thomas Nilsson

Science Divsion
Nuclear and Particle Physics Group
INSTITUT LAUE-LANGEVIN

Department of Fundamental Physics
Subatomic Physics Group
CHALMERS UNIVERSITY OF TECHNOLOGY

Gothenburg, Sweden 2014

Experimental and theoretical refutation of Collinear Cluster Tri-partition
PATRIC HOLMVALL

Supervisor: Dr. Ulli Köster, DS-NPP, Institut Laue-Langevin
Examiner: Prof. Thomas Nilsson, Department of Fundamental Physics, Chalmers

ISSN 1652-8557
Department of Fundamental Physics
Subatomic Physics Group
Chalmers University of Technology
SE-412 96 Gothenburg
SWEDEN
Telephone: +46 (0)31-772 1000

Cover:
Schematic view of three collinear particles.

Printed by Chalmers Reproservice
Gothenburg, Sweden 2014

Experimental and theoretical refutation of Collinear Cluster Tri-partition
Thesis for the degree of Master of Science in Physics
PATRIC HOLMVALL
Department of Fundamental Physics
Subatomic Physics Group
Chalmers University of Technology

ABSTRACT

A new mode of nuclear fission has been reported by the FOBOS collaboration, called Collinear Cluster Tri-partition (CCT). The claim is based on indirect observation via missing-energy events, measuring binary coincidences in thermal neutron-induced fission of ^{235}U, and spontaneous fission of ^{252}Cf. The events were interpreted as perfectly collinear emission of three heavy fragments. The proposed CCT seems to be an astonishing new aspect of nuclear fission, theoretically difficult to reconcile with traditional fission models, and experimentally surprising since the relatively high yield of 0.5 % of such events should have shown up in previous experiments. These claims call for an independent verification with a different experimental technique.

This thesis reports on direct searches for CCT events in thermal neutron-induced fission of ^{235}U, which should manifest as a considerable excess yield around nuclear masses $A \approx 68$–70 and $A \approx 34$–36, compared to known binary fisson events. The experiments were performed with the fission fragment spectrometer LOHENGRIN at the high flux reactor of Institut Laue-Langevin. This spectrometer provides excellent mass and energy resolution and allows for clean measurements down to relative fission yields of 10^{-10}. The known ^{70}Ni yield in binary fission was confirmed, and a new upper limit of the ^{68}Ni yield in binary fission was estimated. No indication of CCT events was found. The result of the experiments sets an upper limit on the order of 10^{-9} per fission for CCT events with $A \approx 68$–70 and $A \approx 34$–36, which is more than 5 orders of magnitude below the yields claimed by the FOBOS collaboration.

In addition, theoretical calculations and simulations have been performed to make sure that the LOHENGRIN experiments cover a sufficient and representative range of kinetic energies of possible CCT fragments. The calculations also show that CCT is an improbable event in low-energy fission.

In conclusion, the experimental results presented in this thesis clearly rule out the existence of CCT far below the level previously claimed, and the theoretical examination demonstrates that current models cannot explain the experimental interpretations as CCT by the FOBOS collaboration.

Keywords: Collinear Cluster Tri-partition, CCT, Ternary Fission, Nuclear Fission.

Contents

1 Introduction

Science aims to provide us with a better understanding of the world that we live in. A scientific model that is commonly used for this purpose is particle physics, in which everything around us is composed of particles. Physicists try to classify the particles by their most fundamental constituents, the elementary particles, a tradition that dates back to the ancient Greeks. The atom was long thought to be the most elementary particle, until the discovery of the nucleus, which itself was later found to be composed of the nucleons (protons and neutrons). The list goes on, and today we know of a number of elementary particles, with the most recent addition being the Higgs boson. Everything that we observe is a consequence of processes involving the interactions between the particles and the different states that they can exist in. Which of the processes and states are allowed is governed by symmetries and conservation laws. Processes are classified into different categories of physics, mainly based on which interactions are involved. Nuclear fission for example, is governed by the nuclear and the Coulomb interaction between the nucleons.

In the nuclear fission process, heavy nuclei split into several smaller charged fragments. The tightest bound[1,2] system is known to be ^{62}Ni. As more nucleons are added to make heavier nuclei, the average binding energy per added nucleon decreases. Eventually the system seeks a more energetically favourable shape by deforming. At some point, the deformation becomes so severe that the repulsive Coulomb force overcomes the attractive nuclear force, and the system breaks up (scissions). Fission can either occur spontaneously, or be induced by nuclear reactions. To better understand nuclear fission, thousands of experimental and theoretical studies have been carried out since its discovery[3,4,5] 75 years ago. Like the nuclear interaction however, nuclear fission still proves to be a great mystery in many aspects.

The nuclear fission process usually produces two charged fragments, in which case it is called binary fission. Once every few hundred fissions however, a third light charged fragment is formed as well, in a process known as ternary fission. Ternary fission was initially of great interest since the additional fragment, known as the ternary particle, was expected to carry vital information about the scission configuration, possibly being able to unravel some of the mysteries of the fission reaction mechanism. Detailed investigation showed that in 90% of the case, the third fragment was an alpha particle (^{4}He), in 9% a heavier helium or hydrogen, and in less than 1% a particle with charge $Z > 2$, with rapidly decreasing yields for higher Z and mass A[6]. The heaviest particles found in for example ^{235}U(n$_{\mathrm{th}}$,f) is ^{22}O with yields of $3\cdot10^{-9}$[7]. For ternary particles with a size comparable to the other two fragments, called true ternary fission, only upper limits of the yield exist in low-energy fission, of roughly 10^{-10}[8,9].

In 2010 claims of experimental observation of ternary $^{34-36}$Si and ^{48}Ca from the reactions ^{235}U(n$_{\mathrm{th}}$,f) and ^{252}Cf(sf), respectively, were published[10]. A surprisingly high yield of about 0.5% per fission was reported, which is even higher than the ternary alpha yield, contradicting what has been generally accepted since the 1940s. More surprising, however, was the fact that almost the exact same yield was reported in two completely different fission channels, and for two very different ternary particles, with widely varying charges and masses. The decay was dubbed “Collinear Cluster Tri-partition” (CCT), since it was argued that all three fragments were emitted perfectly collinear along the same fission axis, and that its discovery had eluded previous experiments since two of the fragments look like a sum event to a detector.

The claim was based on non-detection of the ternary particle, by missing energy from binary coincidences measured with the fission fragment spectrometer FOBOS[11]. The fragment masses were reconstructed from measured velocities and energies, and a peak of a sum mass lower than the fissioning system was apparent in the mass-versus-mass and mass-difference spectra. This was interpreted as collinear tri-partition, where one of the fragments was scattered due to an asymmetry of the setup, corresponding to the target backing blocking the flight path to one of the detectors.

This surprising result triggered a series of theoretical papers [12,13,14,15] that tried to explain the process and calculate the most probable mass splits and energies. However, any new surprising experimental result also calls for an experimental verification with an independent method.

This is possible with the LOHENGRIN fission fragment recoil separator, located at the high-flux neutron reactor of Institut Laue-Langevin in Grenoble, France. LOHENGRIN is a single-arm spectrometer that covers a small solid angle of a fission target, and separates the fission fragments according to their mass and kinetic energy over ionic charge ratios (A/q and E/q, respectively), with a combination of magnetic and electric fields [16,17]. The instrument is currently the most sensitive spectrometer for measurement of neutron-induced fission products, enabling accurate studies of fission yields down to 10^{-10} [18,19].

LOHENGRIN detects only one fragment per fission event, due to its small solid angle acceptance. Perfectly collinear fragments are separated from each other by magnetic and electric fields, not satisfying simultaneously the given A/q and E/q separator conditions. The spectrometer is therefore not used to measure coincidence events in ternary fission directly, but rather events that can be distinguished kinematically from binary fission. Inversely, if at a given yield level no events are detected at LOHENGRIN, it provides a stringent upper limit on the production of these fragments in whatever fission configuration. Hence, a non-observation at LOHENGRIN allows refuting experimental claims of CCT.

1.1 Purpose and scope of the thesis

Nuclear physics is an important field in many aspects. Without the nuclear reactions in the sun, there would be no life on earth. Nuclear fission provides our society with electricity, with steady and reliable neutron sources for probing the inner structure of matter, and with medical treatment and diagnostics, just to mention a few applications.

Better knowledge of the nuclear fission mechanism is therefore required to better understand the world that we live in. This knowledge also has direct technical applications in society, and is essential for building safer and cleaner nuclear reactors. Just recently, several groups in the NEA (Nuclear Energy Agency) discussed how to reduce nuclear physics uncertainties in fission product yields to the sub-percent level. Therefore, verifying or refuting the 0.5% effect interpreted as CCT is very important in many aspects.

This thesis reports on experiments performed at the LOHENGRIN spectrometer, which exclude the previously published results with more than 5 orders of magnitude, by observing an upper limit of the yield of the reported fragments on the order of 10^{-9}. Theoretical calculations and simulations are done to aid the interpretation of the experimental results by deriving possible kinetic energies of the reported fragments. The theory and simulations also highlight several contradictions in the CCT hypothesis. The CCT interpretation of the FOBOS data, which from now on is referred to as the “CCT model”, is excluded as a likely origin since it assumes fission of low fissility nuclei, and because it is based on energetically unfavourable reactions with implausible conditions. It is further shown that if these conditions are alleviated, CCT would very easily have been detected by several experiments before.

1.2 Outline of the thesis

Section 2 provides a general overview of the nuclear fission process. The most relevant theoretical models for this work are introduced, especially the Liquid Drop Model and the Shell-Correction Method (Sec. 2.1). Some experimentally observed properties of nuclear fission are presented, like mass asymmetry, kinetic energy distributions, excitation energy and neutron multiplicities (Sec. 2.3). These properties are important since they are frequently discussed in the thesis. They are also very similar in character to those observed in ternary fission, which is then described in greater detail (Sec. 2.4). There are many theoretical models that try to explain ternary fission, but few that are successful in describing more than a few select observables. The models used in binary fission are limited in their application to ternary fission, as they fail to account for the ternary particle. A detailed review of different models is not given. Instead, generally accepted predictions are summarized (Sec. 2.5), along with experimental results of yields (Sec. 2.6) and other observables (Sec. 2.7). The section ends with a brief discussion of "true ternary fission" and Collinear Cluster Tri-partition (Sec. 2.8).

The FOBOS detector setup is analysed in detail (Sec. 3), to better understand how Collinear Cluster Tri-partition could be conceived, or how it could be misinterpreted missing-energy or anomalous time-of-flight events (incorrectly converted into missing-mass events). Several possible sources of the latter are presented (Sec. 3.3), based on the FOBOS detector setup.

The kinematics section studies the phase space of possible kinetic energies of the reported CCT fragments, analytically from momentum and energy conservation in a kinematic frame, and with Monte Carlo simulations solving the equations of motion in a dynamical frame. The analytical calculations are in very good agreement with the simulations, as well as with other literature[14]. The full analysis shows that the kinetic energies for the fission fragments compatible with CCT are covered by the LOHENGRIN experiments. The results highlight several problems with the CCT model (Sec. 4.6). Although the full process has a high Q-value, the intermediate steps are energetically very unfavourable. In order for CCT to be possible, a set of implausible conditions has to be satisfied. Furthermore, it is shown that if these conditions are met, then FOBOS should have seen a completely different signature, and several previous experiments would have observed CCT.

The LOHENGRIN spectrometer setup is described (Sec. 5) with details on individual modules. The instrument calibration procedure (Sec. 5.2) and the general steps involved in obtaining the yields from the raw count rates in the data analysis (Sec. 5.3) are explained. More details on these steps are given in the LOHENGRIN experiments result section (Sec. 5.4). The results shows an upper limit of the yields on the order of 10^{-9}, which is more than a 5 orders of magnitude exclusion of the previous result published by the FOBOS collaboration.

The discussion section treats the experimental results, the existence of CCT and an analysis of the FOBOS result (Sec. 5.5).

Finally, the entire thesis is summarized and concluded (Sec. 6), and an outlook is given (Sec. 7).

A glossary of commonly used phrases is found in the end of the thesis. Appendices treat CCT kinematics in ^{252}Cf(sf) (App. A), calculations of tip distances at scission (App. B), area and uncertainties of fitting the Normal and Skew-Normal distributions (App. C) used in the data analysis of the LOHENGRIN experiments, as well as simulations with SRIM[20] (App. D) and Geant4[21,22] (App. E).

2 Nuclear fission

Heavy nuclei are known to split into smaller charged fragments in a process known as nuclear fission. The process is mainly a consequence of the gradual decrease in average binding energy per nucleon, that nuclei heavier than ^{62}Ni experience[1,2]. Breaking up these heavy nuclear systems liberates large amounts of energy, of roughly 200 MeV. This energy mainly goes into kinetic and excitation energy of the resulting fragments, and partly into the emission of mostly neutrons and gamma radiation. Although very exo-energetic, the process is usually prevented by a potential barrier. Some systems can transcend this barrier spontaneously via tunneling, while others have to be excited, for example by nuclear reactions. Fission usually proceeds into two charged fragments, in which case it is called binary fission. The formation of three charged fragments is called ternary fission, and occurs once every few hundred binary fissions, with the third particle in 99% of the cases being a hydrogen or helium isotope. This thesis investigates the existence of a special kind of ternary fission, called Collinear Cluster Tripartition (CCT), in the channels ^{235}U(n$_{\text{th}}$,f) and ^{252}Cf(sf). In CCT, all three fragments are of comparable size and emitted perfectly collinear along the fission axis. This section starts by discussing briefly the theoretical models used in general nuclear physics, how they are applied to binary fission, and ends with experimental results. A more thorough investigation of the properties of ternary fission will then be discussed, with the conclusion that the two processes share very similar experimental results, but have to be treated with completely different theoretical models.

2.1 The Liquid Drop Model

Experimental indication of nuclear fission was found in 1938 by Hahn and Strassmann[3,4]. It was later interpreted by Meitner and Frisch[5], who explained the process qualitatively within the framework of the Liquid Drop Model (LDM). The LDM uses a macroscopic treatment of the nucleus as a uniformly charged liquid drop. The model was used to predict nuclear binding energies and Q-values (net energy liberated), making it possible to discern which decay modes and nuclear reactions are allowed. The LDM could also explain many of the gross features of the nucleus, like the valley of stability in the chart of nuclides. Bohr and Wheeler[23] further developed this explanation and applied it to nuclear fission, introducing terms like fissility and the fission barrier. The fissility is a representation of the competition between the repulsive and attractive forces between the nucleons. It is mathematically defined as the ratio of the Coulomb to surface energy in a nucleus

$$\frac{E_C}{2E_S} \propto \frac{Z^2}{A}, \tag{1}$$

and measures the tendency of the system to fission. The fission barrier is defined as the potential energy effective along the most favorable deformation path to fission of a compound system. The barrier can be illustrated by plotting the deformation energy as a function of deformation (see Fig. 1). The ground state lies in a potential well delimited by the fission barrier. If a nucleus manages to get past the barrier and reach a sufficiently high deformation, it scissions. If the barrier is thin enough, the state might tunnel through it, in which case the system is said to be unstable against spontaneous fission. By adding excitation energy, fission of a heavy nucleus can be induced. The height and width of the fission barrier decreases with increased fissility.

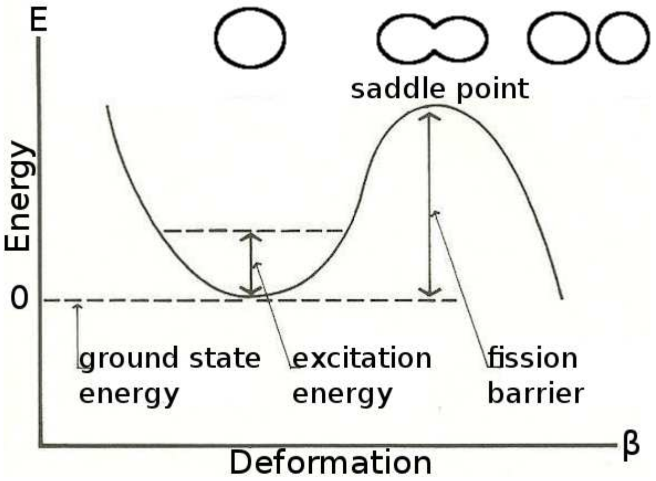

Figure 1: Deformation energy as a function of deformation. The ground state lies in the well delimited by a potential barrier, the height of which is called the fission barrier. Corresponding shapes are shown qualitatively above the curve.

2.2 The Shell-Correction Method

The extended liquid drop model fails to account for the experimentally observed asymmetric mass distribution of the fission fragments (one light and one heavy fragment) in actinide nuclei, as well as the non-spherical ground states of some stable nuclei, the existence of superheavy nuclei, and the observed nucleon magic numbers. These properties were understood to be a consequence of the single-particle energies in the nuclear shell model[24,25], which summarizes the mutual interaction between the nucleons in an average mean field shell-model potential. This potential contains a spin-orbit interaction and a spherical central potential part. The wave functions and single-particle energy levels of the nucleons are then found as solutions of the Schrödinger equation. The shell-model has its own shortcomings, as it is an approximate mean field model, e.g. it fails to accurately describe heavily deformed systems with high surface-to-volume ratio. Furthermore, the results on a large scale are much less accurate than those obtained with the LDM combined with semi-empirically adjusted parameters. A major contribution to theoretical nuclear physics was made by Strutinsky[26], who successfully combined the LDM with shell-effects in his macroscopic-microscopic model, called the shell-correction method (SCM). The SCM correctly predicted a small prolate deformation in the ground state of the actinides, the potential energy dependence of the elongation, and most of the magic numbers. The model also predicted the appearance of multiple maxima in the potential energy barrier. Between these maxima lie local minima, corresponding to different nuclear states of the fissioning system, called fission isomers. The deformation energy of the elongation depends on the multipole orders of the deformation, and spans a multi-dimensional landscape. If the excitation energy is low enough, the decay will follow energetically favorable channels in the landscape as the system makes its saddle-to-scission descent, effectively probing the different states of the potential-energy surface. These fission channels affect the yields and final mass and kinetic energy distributions of the fragments. The final nuclear observables are thus tightly linked to the nuclear structure of the compound system. Some key experimental results of these observables are presented in the following section.

2.3 Binary fission data

The experimental results in binary fission that are most relevant for this thesis are the mass distribution between the two fragments, the kinetic and excitation energy distributions and the emission rates of neutrons. The yield as a function of the fragment mass is seen in Fig. 2.

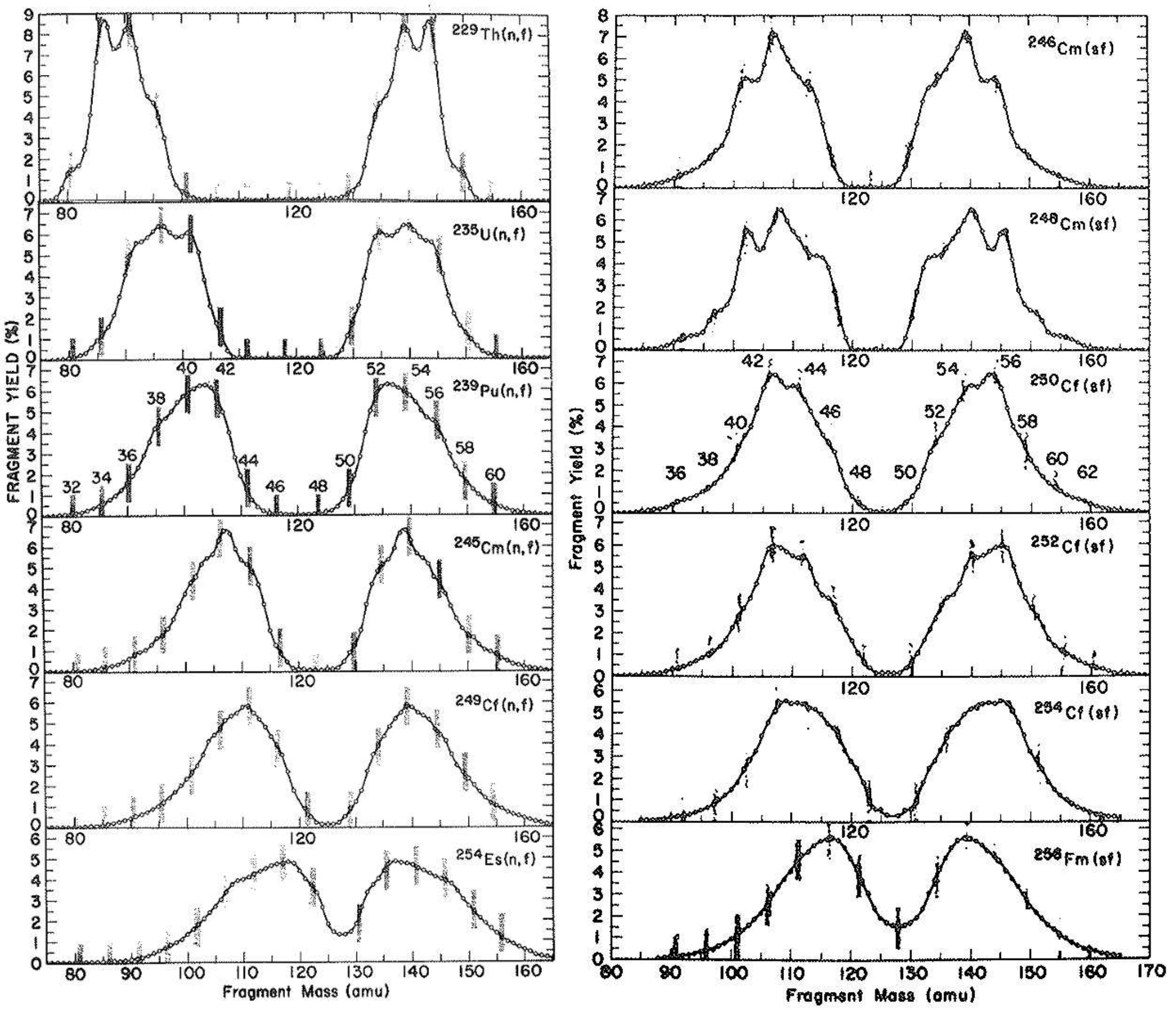

Figure 2: Fragment yield as a function of fragment mass number in neutron induced fission (left) and spontaneous fission (right). Vertical bars correspond to masses associated with even nuclear charges labeled in the figure for ^{239}Pu(n,f) and ^{250}Cf(sf), respectively. (Adapted from Unik et al.[27].)

The plot illustrates that there is a clear mass asymmetry between the fragments produced in both spontaneous and neutron induced fission of the actinides, pertaining to one light and one heavy fragment. As the fissioning system becomes heavier (or much lighter than shown in the figure), or its excitation energy higher, the mass split will become more symmetric. This is understood to be a consequence of shell-effects. The total kinetic energy of the fission fragments of a few systems are plotted in Fig. 3. The average total kinetic energy follows a Gaussian distribution, with higher energies for heavier fissioning system. The distributions are

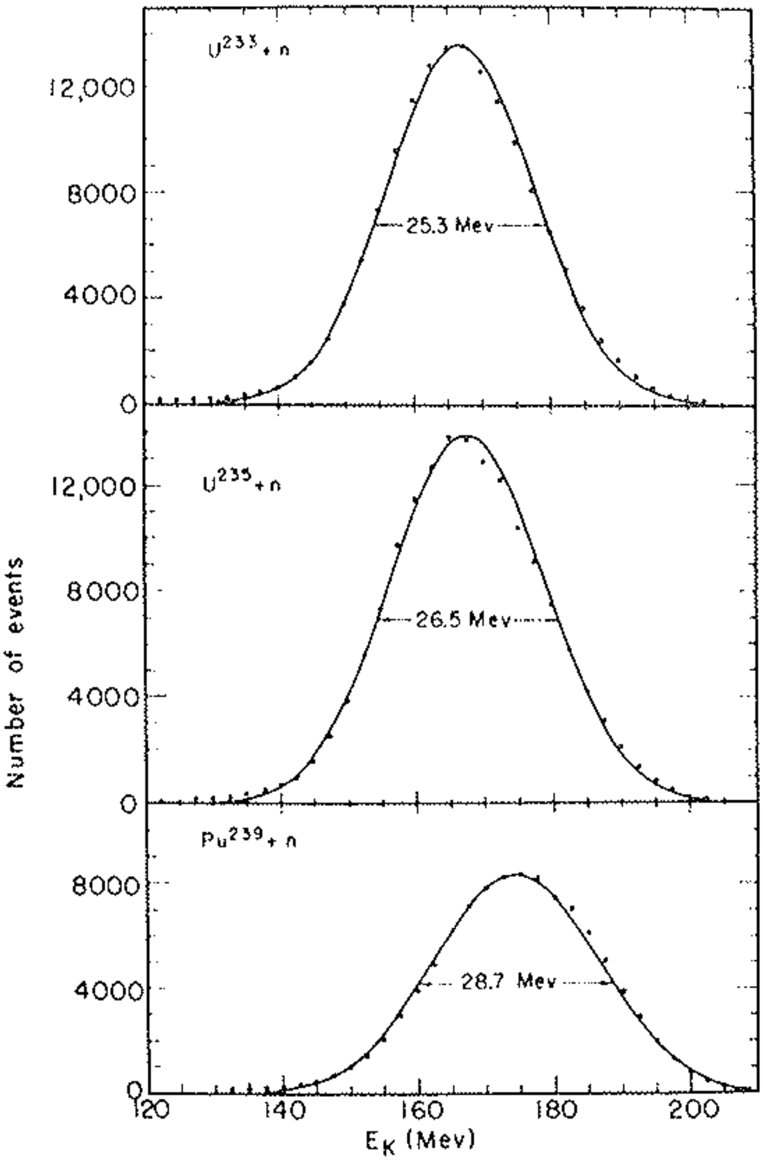

Figure 3: Total kinetic energy distribution (before neutron emission) in the thermal neutron induced fission of ^{233}U, ^{235}U and ^{239}Pu. (Adapted from Milton and Fraser[28].)

centered around 170 MeV and 184 MeV in ^{235}U(n_{th},f) and ^{252}Cf(sf), respectively. Subtracting these energies from the Q-values leaves roughly 30 MeV on average for fragment excitation energies and emission of neutrons and gamma radiation. Each emitted neutron requires around 10 MeV energy, while gammas carry away energies from tens of keV up to several MeV. On the average, about 2–4 neutrons are emitted in binary fission. The independent fission fragment kinetic energies follow Gaussian distributions as well. The light fragment will generally end up with a higher kinetic energy than the heavy fragment, which can be shown by applying momentum and energy conservation.

2.4 Ternary fission

Nuclear fission is usually a binary process, in the sense that two charged particles (the primary fragments) are formed from the fissioning nucleus. The possibility of ternary fission, in which three fragments are created, was proposed in 1941[29]. In 1946 it was found experimentally from tracks in nuclear emulsions photographs[30,31] (see Fig. 4), and was confirmed in 1947 from measurements with ionization chambers[32]. Analysis of the tracks showed that two of the fragments are emitted with similar angles and masses as the light fragment (LF) and heavy fragment (HF) of binary fission (see Fig. 5). The third fragment, called the ternary particle (TP), is much lighter and emitted under roughly right angles to the fission axis. Due to this similarity, ternary fission is also known as light charged particle (LCP) accompanied fission. Ternary fission occurs once every 250–500 fissions for the actinides, and it occurs 25% more often in spontaneous fission than in fission of the same system induced by thermal neutron capture. Although rare, ternary fission is still of interest since it

1. serves as a probe of the nuclear fission mechanism, yielding information about the configuration and dynamics at scission, and
2. produces tritium, helium and hydrogen in nuclear reactors, and thus of interest to the nuclear industry.

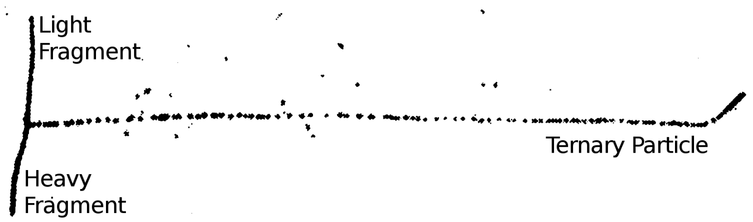

Figure 4: Nuclear emulsion tracks of three fission fragments, marking the first experimental evidence of ternary fission. (Adapted from San-Tsiang et al.[31].)

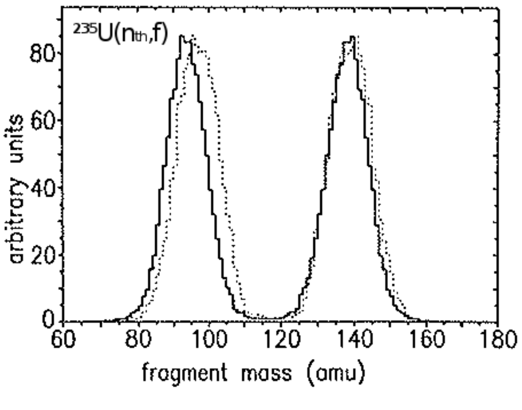

Figure 5: Light and heavy fragment mass yield in binary fission (dotted line) and ternary fission (solid line). The shift is due to the emission of a ternary alpha particle, mostly at the expense of the light fragment mass. (Adapted from Theobald[33].)

2.5 Ternary fission theoretical models

Ternary fission is a three-body decay, thus offering more degrees of freedom and a larger phase space than binary fission. As a result, the theoretical models of binary fission are insufficient at describing the physics of ternary fission. For example, the prerequisites of the liquid drop model and the shell-model are not met, since the surface to volume ratio is too large. The scission point model of Wilkins et al.[34] and the random neck rupture model of Brosa et al.[35] both fail to account for the formation of a ternary particle. There are numerous ternary fission models that account for this and several other aspects. A consistent model that combines all major aspects is however yet to be formulated, or one that can reproduce from first principle the energy distribution and individual yields of the ternary particles. A few key features of generally accepted models will now be presented. Reviews of individual theoretical models can be found in Wagemans[36], Köster[7], and in Börner, Gönnenwein, and Zimmer[37]. Most models are based on the premise that the ratio of ternary to binary events is governed by a factor $\exp(-E_C/T)$, where E_C is seen as the energy cost of emitting a ternary particle, and T a parameter describing how easily scission configurations that are energetically unfavourable can be accessed. The models use different geometrical configurations at scission, and interpret the parameter T differently (basically arguing if it represents a "nuclear temperature" or not). The geometrical configuration of most models can, however, be generalized with the parameterization presented in Fig. 6. The geometrical parameters differ slightly between the models, and they are obtained by doing trajectory calculations which are fitted to experimental results. Most models agree on how ternary fission is formed. The fissioning system is deformed into an elongated prolate shape as it makes it saddle-to-scission transition. As the system is deformed, the shape becomes unstable, and a ternary particle is formed between a light and a heavy fragment as a result of two random neck ruptures.

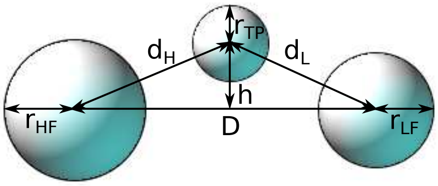

Figure 6: Generalization of most ternary fission models scission configuration.

2.6 Ternary fission yields

Detailed yield measurements show that the ternary particle is in 90% of the cases a ^{4}He and in 9% heavier helium and tritons. Only 1% of all ternary particles have $Z > 2$. The yield decreases rapidly for higher Z and neutron excess[6], and an odd-even Z effect is also observed[7] (see Fig. 7). Heavier fissioning systems more easily emit heavier ternary particles (see Fig. 8). The heaviest ternary particle found in ^{235}U(n$_{\mathrm{th}}$,f) is ^{22}O with yields of $3 \cdot 10^{-9}$[7].

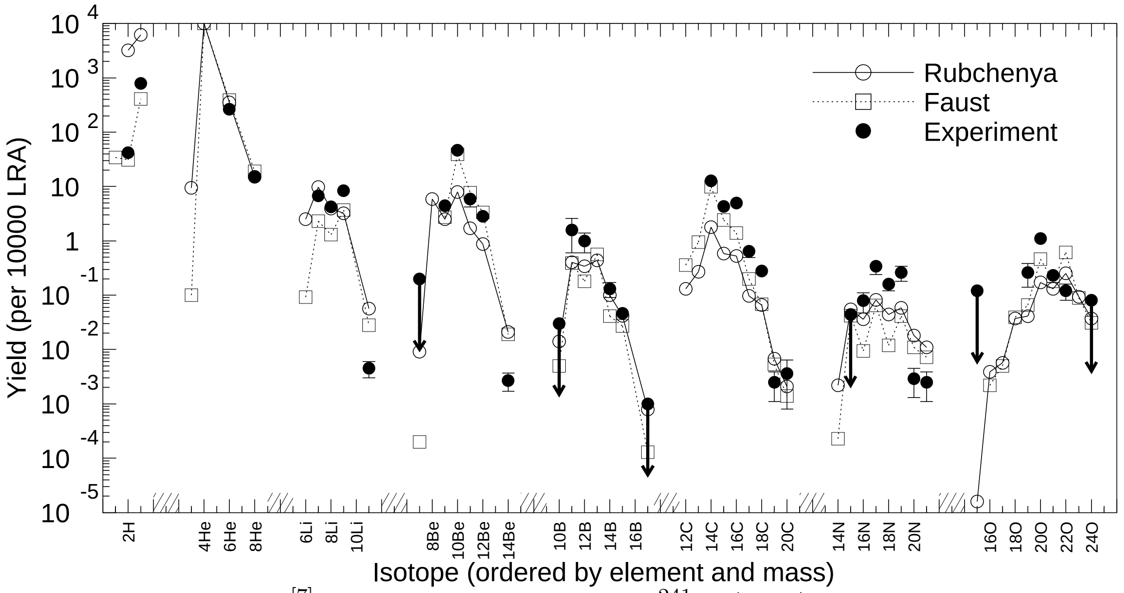

Figure 7: Experimental[7] ternary particle yields in ^{241}Pu(n_{th},f) compared with the theoretical double-neck rupture model of Rubchenya[38], and the Boltzmann model of Faust[39], normalized to 10^4 for ^{4}He. Arrows mark upper limits. (From Köster[7]. With Permission.)

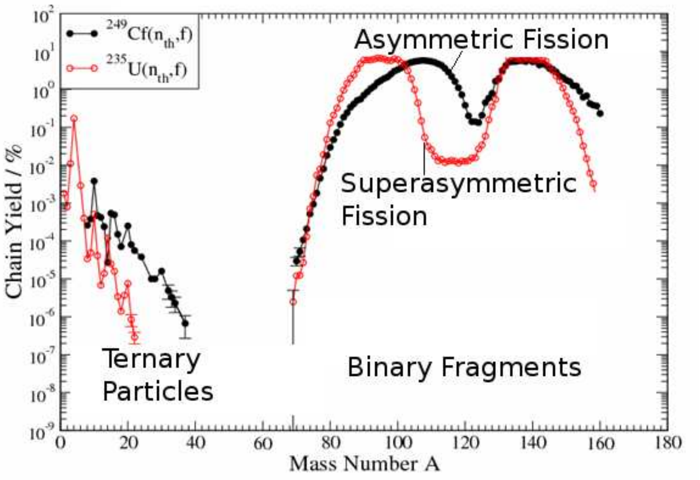

Figure 8: Ternary and binary yields for asymmetric and superasymmetric fission. Heavy fissioning systems are more prone to emit heavy ternary particles, which is illustrated in the figure. (Adapted from Gönnenwein[6].)

2.7 Ternary fission data

Apart from the yield, some of the most relevant observables in ternary fission are the final kinetic energies of the fragments and the emission angle between the light fragment and ternary particle. The kinetic energy of ternary particles generally follow a Gaussian distribution. Ternary alpha particles have a mean kinetic energy close to 16 MeV (see Fig. 9). This energy is significantly larger than that of alphas produced in radioactive alpha decay, giving longer tracks, which is why ternary alphas are often referred to as “long range alphas” (LRA). The mean kinetic energy of the other abundant ternary particles vary between 8 and 20 MeV. The total kinetic energy in ternary fission is different to that observed in binary fission (see Fig. 10). By subtracting the total kinetic energy from the Q-value, the total excitation energy is attained. The total excitation energy is much lower in ternary than in binary fission, on the average by about 10 MeV in ^{235}U(n$_{\mathrm{th}}$,f)[41]. The emission of a ternary particle therefore occurs at a great expense of the systems total excitation energy. The higher the ternary particle kinetic energy, the lower the total excitation energy becomes[33]. There is also a correlation between the kinetic energy and the emission angle of ternary alphas, as well as between the yield and the emission angle (see Fig. 11). A great majority of all ternary particles are emitted at roughly 90° with respect to the fission axis, shifted slightly towards the light fragment direction. Looking at the kinetic energy and angular distribution, it is concluded that the

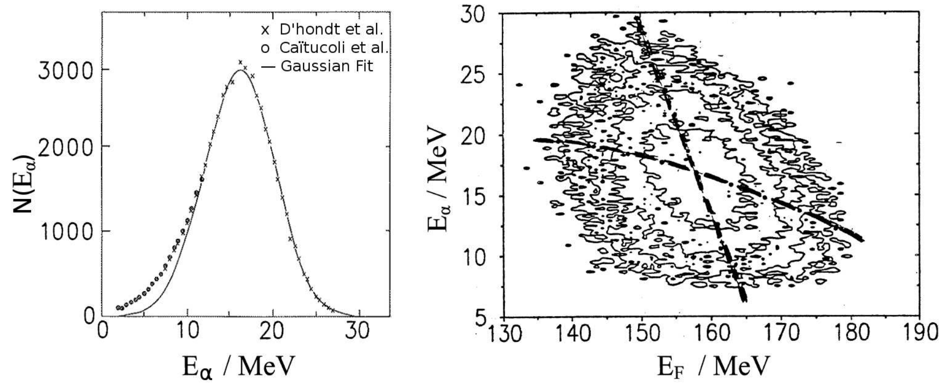

Figure 9: Left: Kinetic energy distribution of ternary alpha in ^{235}U(n$_{\mathrm{th}}$,f). The deviation from the Gaussian fit on the left tail is to a large extent caused by alpha particles originating from ^{5}He $\rightarrow ^4$ He + n. (Adapted from Wagemans[36].) Right: Ternary alpha kinetic energy versus the total kinetic energy of the corresponding fission fragments in ^{235}U(n$_{\mathrm{th}}$,f). (Adapted from Pannicke, J.[40].)

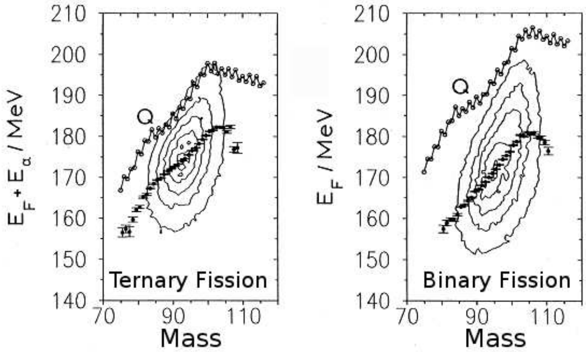

Figure 10: Total kinetic energy as a function of light fragment mass, in ternary fission (left) and binary fission (right) of ^{235}U(n$_{\mathrm{th}}$,f). Events with equal yield lie on the same contour line. The Q-value is represented by a solid line, and average experimental kinetic energies by scatter points with error bars. The total excitation energy equals the Q-value subtracted by the total kinetic energy, and as can be seen, is much higher in binary than in ternary fission. (Adapted from Theobald[33] and Pannicke, J.[40].)

ternary particles are born in the region between the other two fragments at scission, or emitted towards the middle from one of the fragments during the last stage of scission. The small yields at zero angles correspond to so-called polar emission[42]. These ternary particles were first thought to be born on the outside of the system, but detailed analysis points towards an entirely different mechanism in which such fragments are evaporated from the light fragment in-flight[43,44].

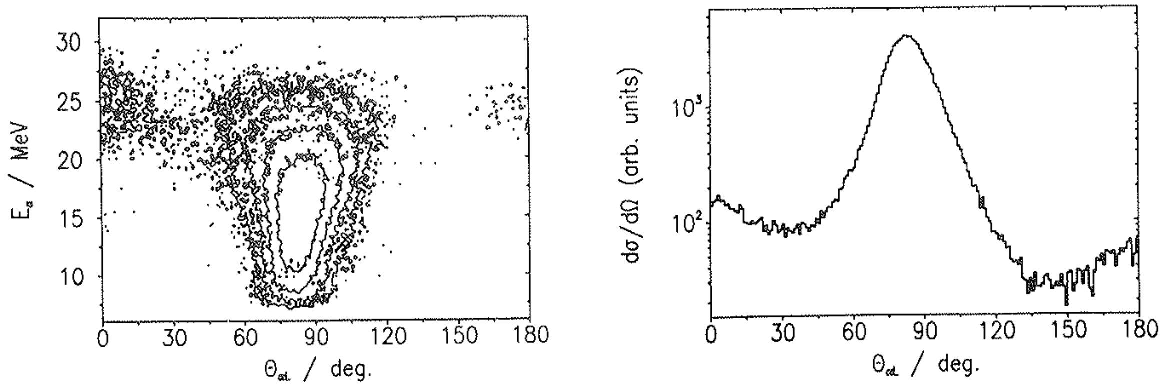

Figure 11: Correlation between ternary alpha kinetic energy and emission angle (left), and ternary alpha yield and emission angle (right) in ^{235}U(n$_{\text{th}}$,f). The emission angle is relative to the light fragment direction. Contour lines in the left figure mark equal yields. (Adapted from Theobald[33].)

2.8 True ternary fission and collinear cluster tri-partition

Theories have long suggested the existence of so-called true ternary fission, in which all three fragments have a similar mass. Experimentally, only upper limits exist in low-energy fission[8,9], of less than 10^{-8} to 10^{-11} events per fission. These experiments were designed to search for ternary particles emitted with angles $0° < \theta < 180°$ relative to the light fragment direction. A publication[45] from the FOBOS collaboration argued that these experiments could have failed to detect true ternary fission events if the three particles were emitted perfectly collinear, along the same fission axis. Such a configuration was dubbed Collinear Cluster Tri-partition (CCT). In practice such a decay is more difficult to detect, since two fragments entering a detector collinearly could be detected as a sum event that is interpreted as a single heavy fragment. In 2010, the FOBOS collaboration reported the observation of CCT with ternary particles of masses $A > 30$ and high yields of about 0.5% per fission in both ^{235}U(n$_{\text{th}}$,f) and ^{252}Cf(sf)[10]. Since then, several theoretical papers have tried to explain the observation[12,13,14,15], but the experimental results themselves are yet to be verified independently. An experiment with a similar setup reported a non-observation of CCT in 1999[46]. The FOBOS experiment was based on the missing-energy principle, by non-detection of the ternary particle, due to scattering in an asymmetry in the detector setup. A short summary of this experiment is given in Sec. 3. Looking more closely at the kinematics however, it is shown in Sec. 4 of this thesis that if CCT existed, it should be observable even without the asymmetry. It should have been detected by countless binary and ternary fission experiment setups alike, due to the low energy of the ternary particle.

3 FOBOS experiments

The claims of Collinear Cluster Tri-partition were published[10] based on experiments performed at the Flerov Laboratory of Nuclear Reactions (FLNR) of the Joint Institute for Nuclear Research (JINR) in Dubna, Russia. There are two experiments reported in this publication, measuring two different fissioning systems with the same detector modules in the double-armed spectrometer setup FOBOS[11], and the slightly modified setup mini-FOBOS[47]. This section will discuss the details of the setups and the reported results.

3.1 The FOBOS setup

FOBOS is a spectrometer designed for studying decay products from compound-like systems, which are created in nuclear reactions. In particular, it has detector modules placed at relative angles of 180° (with ±2° acceptance), which were used to study binary coincidences from nuclear fission (see Fig. 12). The detection of these fragments is based on the time-of-flight versus energy method (TOF-E), allowing the determination of individual fragment velocities (v) and kinetic energies (E). The time-of-flight is measured along a 50 cm flight path, as the difference between a start and a stop signal. The start signal is obtained from an avalanche counter, or a micro channel plate (MCP) detector, and the stop signal by a position-sensitive avalanche counter (PSAC). The energies of the fragments are measured in Bragg ionization chambers (BIC). Each BIC has a 1μm thick aluminized Mylar window with a 385 mm diameter. The window is supported by a heavy concentric carrier and a 1 mm thick Ni-mesh, with hexagonal holes of 2.7 mm diameter and 0.9 mm bulkhead between the holes. These support structures reduce the total transparency to 75%. The most important feature of the setup is the 50 μg/cm^2 thick Al_2O_3 target backing. It is positioned such that it creates an asymmetry, blocking the flight path towards one of the detectors. The backing creates an angular spread of the fission fragments, and lowers their kinetic energies. The detected

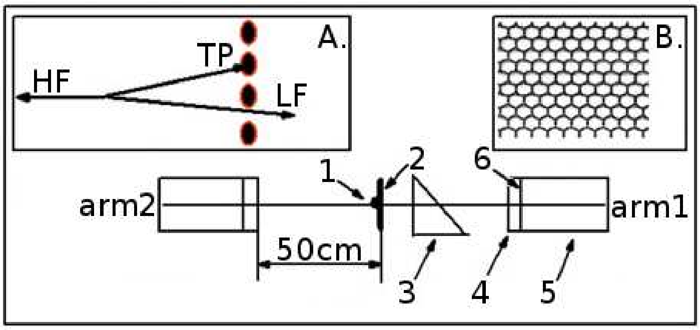

Figure 12: Schematic view of the FOBOS detector setup used to measure binary coincidences of a light (LF) and heavy (HF) fission fragment. The fission target (1) is deposited on an Al_2O_3 backing (2). The time-of-flight of fission fragments is measured over a 50 cm flight distance, as the time difference between a start and stop signal (from detectors 3 and 4, respectively). The fragment energies are measured in a BIC (5). The analysis of the FOBOS paper argued that a third ternary particle (TP) was scattered by the backing and implanted subsequently in the mesh of the BIC entrance window (6). A schematic view of such a process is seen in inset A, and an enlarged image of the mesh in inset B. (Adapted from Pyatkov et al.[10].)

velocity and kinetic energy can be converted into a fragment mass (m) through the relation $m = 2E/v^2$. For most of the detected events, the masses of the two fragments (labeled 1 and 2) should roughly add up to the mass of the fissioning system (FS), along the straight line $m_1 + m_2 = m_{\mathrm{FS}}$ in a mass-versus-mass spectrum. Significant deviations from this line could indicate the production of a third particle missing the detectors. It could also be due to missing energy of the detected fragments, or an anomalous time-of-flight. In this way, missing energy or anomalous time-of-flight could be misinterpreted as a "missing-mass" event.

3.2 Measurement, results and interpretation

Two fissioning systems were studied in detail in the FOBOS experiments, ^{252}Cf(sf) with $13{\cdot}10^6$ detected coincidences and ^{235}U(n_{th},f) with $2 \cdot 10^6$ detected coincidences. The latter used an additional detector module consisting of a belt of ^{3}He-filled detectors for measuring neutron coincidences, in the so-called modified mini-FOBOS setup. Apart from this, the same detector modules was used in both experiments (hence a systematic error would show up with the same signature in both experiments). The results show that the the derived masses (m_1, m_2) of the binary fragments in most reconstructed events add up to the mass of the fissioning system within the given mass resolution (for light fragments $\delta m \approx 6$ amu). The m_1-m_2 spectrum (see Fig. 13) however shows an "island" of apparently lower sum mass which is more pronounced on the side of the fission target where the fragments have to traverse the Al_2O_3 backing. The difference spectrum of both arms shows that these "missing-mass events" (translated from missing energy, or oddly measured time-of-flight) represent about 0.5% of all detected fission events (see Fig. 14), and are associated with the detection of fragments of mass $A \approx 68 - 70$ and charge $Z \approx 26 - 28$. This observation was interpreted as collinear tripartition where two of the fragments are emitted under an angle small enough for simultaneous detection in the detector arm opposite the target backing. If emitted in the direction of the backing however, one of the collinear fragments undergoes small-angle scattering in the backing and is implanted into the support grid of the ionization chamber, thus preventing the simultaneous detection. It was argued that the missing particles corresponded to ternary ^{48}Ca in ^{252}Cf(sf), and ternary $^{34\text{–}36}$Si in ^{235}U(n_{th},f).

3.3 Preliminary discussion of the FOBOS results

The exact relative CCT yields reported are $(4.7 \pm 0.2) \times 10^{-3}$ for ternary ^{48}Ca in ^{252}Cf(sf), and $(5.1 \pm 0.4) \times 10^{-3}$ for ternary $^{34\text{–}36}$Si in ^{235}U(n_{th},f). This is an extremely surprising result for several reasons. First of all, it contradicts all previous ternary fission experiments since the 1940s, which report on a rapidly decreasing yield for heavier ternary particles. The CCT yield is in fact even higher than that for ternary alpha particles. What is more astonishing is that the exact same signature with the same frequency is reported in both spontaneous and neutron-induced fission, for two ternary particles with very different nuclear charge and mass. These are two completely different kinds of reactions, with large differences in mass and energies involved. In fact, ternary fission is 25% more abundant in spontaneous fission and more abundant for heavier fissioning systems. Furthermore, at such high yields the decay ought to have been found in radiochemical analysis. It is also intriguing why the ternary particle is never observed in coincidence with the heavy fragment, corresponding to events where the light fragment nickel misses the detector.

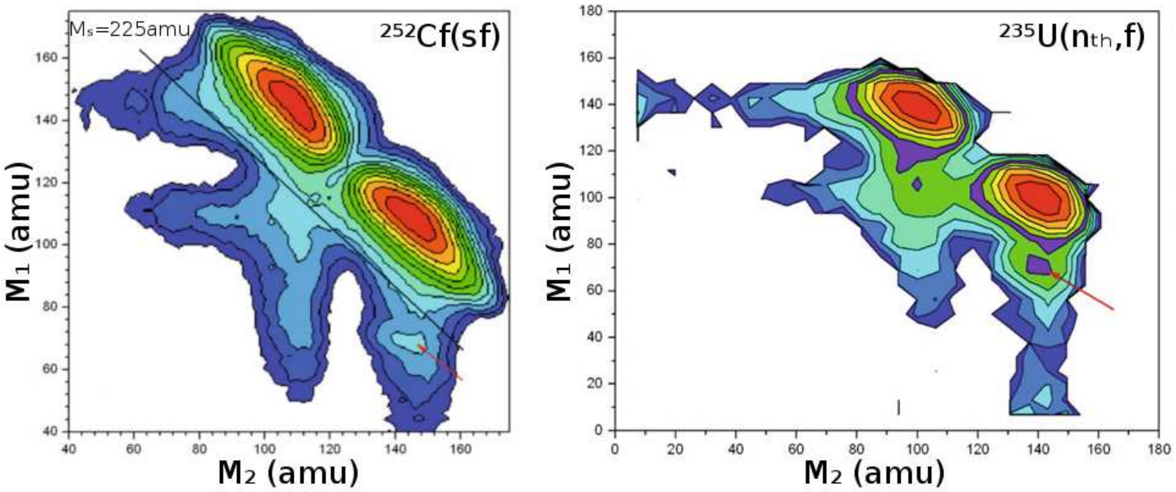

Figure 13: Mass-versus-mass coincidence spectrum of fission fragments from the reactions ^{252}Cf(sf) (left figure) and ^{235}U(n$_{\text{th}}$,f) (right figure), detected by the FOBOS spectrometer. The contour lines mark events with equal yields, with a logarithmic scale factor of approximately 2.5 between adjacent contours. The arrow marks “islands” of lower sum mass which are more pronounced on the side that the target backing is blocking. The analysis in the publication from the FOBOS collaboration argued that the islands correspond to a measured ^{132}Sn and ^{72}Ni in ^{252}Cf(sf), and a ^{132}Sn and $^{68–70}$Ni in ^{235}U(n$_{\text{th}}$), thus leaving a ^{48}Ca and $^{34–36}$Si undetected in each system, respectively. (Adapted from Pyatkov et al.[10].)

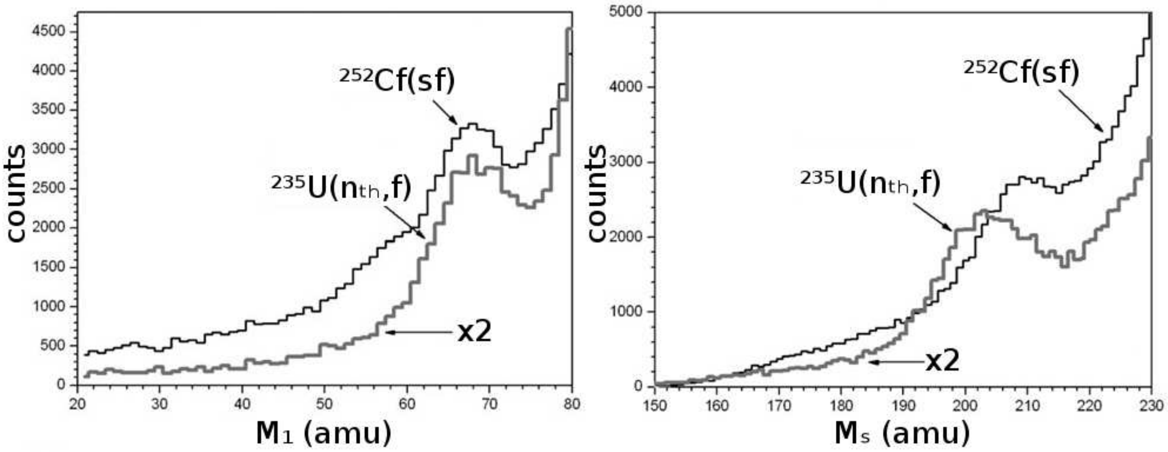

Figure 14: Projection of the island onto the m_1-axis (left figure) and the $m_s = m_1 + m_2$ direction (right figure). Note that the ^{235}U spectrum is amplified by a factor 2 for easier comparison, but that the effect is almost exactly as frequent in the two systems. (Adapted from Pyatkov et al.[10].)

4 CCT kinematics

This section is devoted to showing that the LOHENGRIN experiment covers a sufficient and representative range of kinetic energies for the CCT fission fragments reported by FOBOS[10]. The kinetic energies of such fission fragments are derived analytically from momentum and energy conservation. Monte Carlo trajectory simulations are done to further explore the phase space of possible kinetic energies, and they are in very good agreement with analytical results. Both results are also in agreement with Vijayaraghavan et al.[14]. The full analysis shows that the kinetic energies for the fission fragments compatible with CCT are covered well at the LOHENGRIN experiment. The calculations and simulations also highlight several problems with the CCT model. Although the full process has a high Q-value, the intermediate steps are energetically very unfavourable. In order for CCT to be possible, a set of implausible conditions has to be satisfied. Furthermore, it is shown that if these conditions are met then FOBOS and many other experiments based on double-armed spectrometers should have seen a clear signature of CCT in *both* detectors, due to the low energy of the ternary particle.

4.1 Fissioning system

Experiments and theory since the 1940s generally agree that ternary fission is a simultaneous decay with three fragments being born at roughly the same time. However, FOBOS claims to have observed CCT as a sequential decay, with three fragments being born from two perfectly collinear sequential binary fissions. Kinematically, these decay channels are two extremes of the same decay, where the time between the first and second scission is the parameter that varies. This time is infinitesimal in the extreme lower limit, which corresponds to the simultaneous decay. In the extreme upper limit the time approaches infinity, and the fission fragments are fully accelerated before the second break up. Note that the fission fragment acceleration time (to 90% of the final kinetic energy) is on the order of 10^{-20} s[36]. This is an extremely short time compared to the fission life time of the secondary fissioning system, since it is a low fissility nucleus, making intermediate times between the two extremes implausible. Either way, the kinetic energy distributions of the intermediate times are covered between the two extremes in a kinematical frame. The dynamical frame is much more advanced, and the two decay types (ternary and binary fisson) have to be described with completely different theoretical models (e.g. see Sec. 2). The kinematical frame is sufficient however to analyse which kinetic energies are possible, from an energy and momentum conservation standpoint. The kinetic energy phase space of the reported CCT fragments is derived from kinematics analytically, and dynamically through simulations. In the thermal neutron induced fission of uranium, the reported fragments are

$$\mathrm{n_{th}} + {}^{235}_{92}\mathrm{U} \quad \longrightarrow \quad {}^{A_{\mathrm{Sn}}}_{50}\mathrm{Sn} + {}^{A_{\mathrm{Mo}}}_{42}\mathrm{Mo} + \nu_1 \quad \longrightarrow \quad {}^{A_{\mathrm{Sn}}}_{50}\mathrm{Sn} + {}^{A_{\mathrm{Ni}}}_{28}\mathrm{Ni} + {}^{A_{\mathrm{Si}}}_{14}\mathrm{Si} + \nu_2, \qquad (2)$$

with $A_{\mathrm{Sn}} \approx 132$, $A_{\mathrm{Mo}} \approx 102$–$104$, $A_{\mathrm{Ni}} \approx 68$–$70$, $A_{\mathrm{Si}} \approx 34$–$36$ and $\nu = \nu_1 + \nu_2 \approx 0$–$2$ is the neutron multiplicity. In the spontaneous fission of californium, the reported fragments are

$${}^{252}_{98}\mathrm{Cf} \quad \longrightarrow \quad {}^{A_{\mathrm{Sn}}}_{50}\mathrm{Sn} + {}^{A_{\mathrm{Cd}}}_{48}\mathrm{Cd} + \nu_1 \quad \longrightarrow \quad {}^{A_{\mathrm{Sn}}}_{50}\mathrm{Sn} + {}^{A_{\mathrm{Ni}}}_{28}\mathrm{Ni} + {}^{A_{\mathrm{Ca}}}_{20}\mathrm{Ca} + \nu_2, \qquad (3)$$

with $A_{\mathrm{Sn}} \approx 132$, $A_{\mathrm{Cd}} \approx 120$, $A_{\mathrm{Ni}} \approx 72$, $A_{\mathrm{Ca}} \approx 48$ and $\nu = \nu_1 + \nu_2 \approx 0$. The LOHENGRIN experiment measured yields of ${}^{34,36}\mathrm{Si}$ and ${}^{68,70}\mathrm{Ni}$ in ${}^{235}\mathrm{U}(\mathrm{n_{th}},\mathrm{f})$. This section calculates the kinematics of these fragments, with an extended mass range. See App. A for ${}^{252}\mathrm{Cf}$ results.

4.2 Sequential decay kinematics

In the sequential decay of uranium, the fissioning system (FS) decays into a heavy fragment (HF) tin and an intermediate fragment (IM) molybdenum. The IM decays into the ternary particle (TP) silicon and the light fragment (LF) nickel (see Fig. 15). The fission axes of the two decays are perfectly collinear. If the first scission is similar to that of ternary fission (two necks, but only one rupture), the LF will predominantly be born on the outside due to an initial deformation in the IM[48]. If this is not the case, there should be no preference, and the LF should be born with equal probability in the middle as on the outside. In both cases the LF will appear on the outside, and an experiment only needs to cover the energies of this configuration to find CCT, if it exists. Both configurations are analysed in the following sections. The fragment born in the middle has a reduced kinetic energy. This is because the direction of its acceleration in the rest frame is opposite to the direction that the frame itself is moving. The acceleration of the outer fragment is in the same direction as the movement of the rest frame, and will obtain the highest boost in kinetic energy. The kinetic energy of the outer fragment is at its maximum if

- the IM excitation energy ($\mathrm{E}^{*}_{\mathrm{IM}}$) equals the total excitation energy of the system (TXE),
- all of the excitation energy is spent during the scission of the IM.

The outer fragment kinetic energy is at a minimum if there is instead a lot of excitation energy that is not used in this fashion, or if the IM is in a highly deformed state as it scissions. The problem with such a lower limit is however that for most decays ${}^{A_{\mathrm{Mo}}}\mathrm{Mo} \to {}^{A_{\mathrm{Ni}}}\mathrm{Ni} + {}^{A_{\mathrm{Si}}}\mathrm{Si}$, the Q-value is negative, sometimes as low as -20 MeV (see Fig. 18 in Sec. 4.5.1). Furthermore, due to energy conservation, the fragments have to be born at unphysically large distances (see the discussion in Sec. 4.6.2). Therefore, a large excitation energy is required for the decay to occur in the first place, which is why the lowest possible excitation energy determines the lower kinetic energy limit. The final fragment kinetic energies can be derived as a function of the excitation energies, mass split and number of prompt neutrons.

Taking the limit where the HF and IM are fully accelerated before the second scission means that all Coulomb potential energy has been converted into kinetic energy, and the energy balance is

$$Q_1 = E_{kin,1} + \mathrm{TXE}, \tag{4}$$

where TXE is the total excitation energy, $E_{kin,1}$ the total kinetic energy, and Q_1 the Q-value

$$Q_1 = M_{FS} - M_{HF} - M_{IM} - M_{\nu_1}, \tag{5}$$

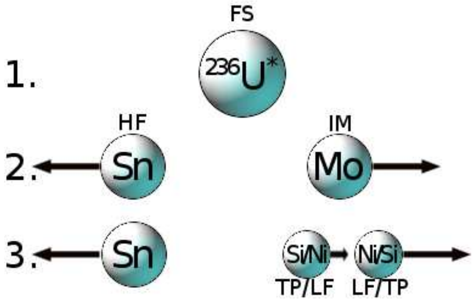

Figure 15: Schematic view of two sequential decays of ${}^{235}\mathrm{U}(\mathrm{n_{th}},\mathrm{f})$ into CCT.

where M are the mass excesses, and ν_1 prompt neutrons. Note that in the calculations, all neutrons are considered to be prompt, which means that they do not originate from evaporation in the fragments. The impact due to different kinds of neutrons will be handled in the discussion. The kinetic energy is then fully determined as a function of the parameter TXE. The momenta for the HF and IM can be determined from momentum conservation

$$p_{HF} + p_{IM} = 0 \tag{6}$$

and the relation

$$E_{kin,1} = E_{kin,HF} + E_{kin,IM} = \frac{p_{HF}^2}{2m_{HF}} + \frac{p_{IM}^2}{2m_{IM}}. \tag{7}$$

Solving for p_{IM} and p_{HF} gives

$$p_{IM} = \pm\sqrt{2E_{kin,1}\frac{m_{HF}m_{IM}}{m_{HF}+m_{IM}}} = \pm\sqrt{2\left(Q_1 - \mathrm{TXE}\right)\frac{m_{HF}m_{IM}}{m_{HF}+m_{IM}}}, \tag{8}$$

and

$$p_{HF} = -p_{IM} = \mp\sqrt{2\left(Q_1 - \mathrm{TXE}\right)\frac{m_{HF}m_{IM}}{m_{HF}+m_{IM}}}. \tag{9}$$

There are two solutions, corresponding to the two directions along the fission axis. The final system is fully accelerated when all the energy released in the second decay has gone into kinetic energy

$$E_{kin,2} = Q_2 + E^*_{\mathrm{IM}}, \tag{10}$$

where E^*_{IM} is the IM excitation energy, and the second scission Q-value is

$$Q_2 = M_{IM} - M_{LF} - M_{TP} - M_{\nu_2}. \tag{11}$$

The final momenta of the TP and the LF are related through the expressions

$$p_{LF} + p_{TP} = p_{IM}, \tag{12}$$

and

$$E_{kin,2} = \frac{p_{LF}^2}{2m_{LF}} + \frac{p_{TP}^2}{2m_{TP}} = \frac{p_{LF}^2}{2m_{LF}} + \frac{\left(p_{IM} - p_{LF}\right)^2}{2m_{TP}}. \tag{13}$$

Solving for p_{LF} and p_{TP} gives

$$p_{LF} = \frac{p_{IM}m_{LF} \pm \sqrt{m_{LF}m_{TP}\left[2\left(Q_2 + \mathrm{E}^*_{\mathrm{IM}}\right)\left(m_{LF}+m_{TP}\right) - p_{IM}^2\right]}}{m_{LF}+m_{TP}}, \tag{14}$$

and

$$p_{TP} = \frac{p_{IM}m_{TP} \mp \sqrt{m_{LF}m_{TP}\left[2\left(Q_2 + \mathrm{E}^*_{\mathrm{IM}}\right)\left(m_{LF}+m_{TP}\right) - p_{IM}^2\right]}}{m_{LF}+m_{TP}}, \tag{15}$$

where p_{IM} is given by Eq. (8). The two solutions corresponds to the LF being born on the outside while the TP is born in the middle, and vice versa. Finally, the kinetic energies are given as

$$E_{kin,LF} = \frac{p_{LF}^2}{2m_{LF}} \tag{16}$$

and

$$E_{kin,TP} = \frac{p_{TP}^2}{2m_{TP}}. \tag{17}$$

Figures 17, 19 and 20 in Sec. 4.5 present results attained using these equations for ^{235}U(n$_{\mathrm{th}}$,f), for varying excitation energies, mass splits between the HF and IM, mass splits between the TP and LF, and number of prompt neutrons. These results are compared to numerical results attained from Monte Carlo trajectory simulations, and there is a very good agreement. Analytical calculations for the simultaneous decay channel will now be presented.

4.3 Simultaneous decay kinematics

In usual ternary fission, the three fragments are all born more or less simultaneously, with the TP in the middle (see Fig. 16). The configuration that gives the highest kinetic energy for the LF is when the TP is born touching the HF, and the LF is as close to them as possible (constrained by energy conservation). This is because the TP is accelerated by the HF, and transmits momentum to the LF (see the results in Fig. 24). Usually in ternary fission, the TP is born in the center between the two main fragments, or in the electrostatic saddle point (where the Coulomb forces from the HF and LF cancel). If the angular momentum is zero, pre-scission kinetic energy is ignored, and energy conservation is invoked, then the configuration at scission can be described with one parameter, x_r, denoting the relative distance of the TP between HF and LF. Let $x_r = 0$ and $x_r = 1$ correspond to the TP touching the HF and LF respectively. This parameterization will now be derived. Energy conservation at scission reads

$$Q = E_{\mathrm{C}} + \mathrm{TXE}, \tag{18}$$

where TXE is the total excitation energy, the Q-value is

$$Q = M_{FS} - M_{HF} - M_{TP} - M_{LF} - M_{\nu}, \tag{19}$$

and the Coulomb potential energy is

$$E_{\mathrm{C}} = k\frac{e^2 Z_{TP} Z_{HF}}{x} + k\frac{e^2 Z_{TP} Z_{LF}}{d} + k\frac{e^2 Z_{HF} Z_{LF}}{D}, \tag{20}$$

where k is the Coulomb constant, e the elementary charge, and the center-to-center distances are x between the TP and HF, d between the TP and LF, D between the HF and LF. Let

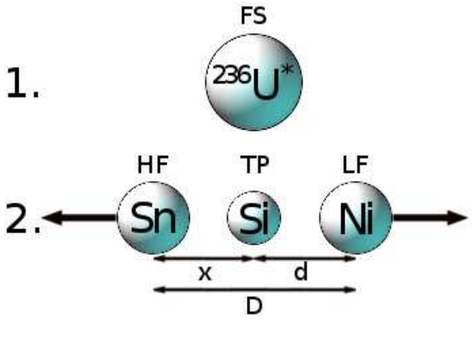

Figure 16: Schematic view of a decay of ^{235}U(n$_{\mathrm{th}}$,f) into simultaneous CCT.

r_{TP}, r_{HF} and r_{LF} denote the radii of the TP, HF and LF respectively. The center-to-center distances x and d can then be written in terms of the radii, D and the parameter x_r as

$$x = r_{TP} + r_{HF} + x_r \left(D - 2r_{TP} - r_{LF} - r_{HF}\right), \tag{21}$$

$$d = D - x. \tag{22}$$

Putting this into the Coulomb potential in Eq. (20), and substituting it into the energy balance in Eq. (18), D (and consecutively x and d) can be solved as a function of x_r. This is done by multiplying the denominators on the right hand side, and solving the resulting third degree polynomial for D. This polynomial only has one real (positive) root that satisfies the conditions that $(Q - TXE) > 0$ and that the HF is to the left, TP in the middle and LF to the right. For a given fissioning system, the scission configuration is then described by the single parameter x_r. To obtain the configurations yielding the maximum and minimum kinetic energies of the LF, x_r is set to 0 and 1 respectively. The final kinetic energies can then be attained in an analytically closed form, by performing the following steps:

1. define three new translation-invariant coordinates as functions of x, d and D,
2. describe the Coulomb potential and the particle momenta with the new coordinates,
3. write down the Lagrangian for the system,
4. solve the final kinetic energies when taking the time limit $t \to \infty$.

Instead of doing this, the final kinetic energies were attained by iteratively solving the equations of motion with the starting configurations described above. The system was iterated until most of the Coulomb potential energy was converted into kinetic energy. This is the method that the simulations are based upon, and they will now be described in more detail.

4.4 CCT dynamics with trajectory simulations

This section describes how the trajectory simulations were done to get a numeric estimate of the kinetic energy distributions. The initial particle configurations after scission were derived from energy and momentum conservation, and expressed as a function of the other parameters/degrees of freedom in the system. All possible starting configurations were generated with Monte Carlo calculations, by sampling the parameters over all possible values in the phase space. The generated configurations were used as input to simulate the trajectories of the fission fragments, by solving the equations of motion arising from a repulsive Coulomb interaction and an attractive Yukawa plus exponential nuclear interaction[49,50]. The trajectories were evolved until most of the potential energy was converted into kinetic energy. The size of the time step was 10^{-25} s, which is reasonable since fission fragments are accelerated on a time scale of 10^{-20}. The Coulomb potential has the form

$$V_{C,ij} = k\frac{e^2 Z_i Z_j}{r_{ij}}, \tag{23}$$

where k is the Coulomb constant and e the elementary charge. The Yukawa plus exponential nuclear attractive potential has the form

$$V_{N,ij} = -4\left(\frac{a}{r_0}\right)^2 \sqrt{a_{2i}a_{2j}}\Big(g_i g_j (4+\eta) - g_j f_i - g_i f_j\Big)\frac{\exp(-\eta)}{\eta}, \tag{24}$$

where $\eta = R^s_{ij}/a$, and the functions g and f are

$$g_k = \zeta \cosh \zeta - \sinh \zeta \tag{25}$$

and

$$f_k = \zeta^2 \sinh \zeta \tag{26}$$

where $\zeta = R_k/a$ with the radius of the nucleus as $R_k = r_0 A_k^{1/3}$, and $r_0 \approx 1.25$ fm. The diffusivity parameter is $a = 0.68$ fm, and the asymmetry parameter $a_{2k} = a_s(1 - \omega I^2)$ is given by $a_s = 21.13$ MeV, $\omega = 2.3$ and $I = \frac{N-Z}{A}$. The nuclear potential had little to no effect on the limits of the kinetic energy, as the particles were generally born far enough apart to make its influence vanish. Even for shorter distances, its effect was negligible. Note however that particles have to be put at initial distances where $F_{\text{nuclear}} < F_{\text{Coulomb}}$, since they would be absorbed into each other otherwise (which is either unphysical, or means that the fissioning system does not decay). This means that the upper and lower limits ($x_r = 0$ and $x_r = 1$) are hard to achieve in reality without a pre-scission kinetic energy. A specific description of the sequential and simultaneous decay simulations will now be given, followed by results.

4.4.1 Sequential decay trajectory simulations

In the sequential decay channel, the simulations started just after the second scission. The HF and IM are at that point fully accelerated, which is realized by reducing the Coulomb potential energy between the HF and IM to approximately zero MeV, and by setting their separation distance to some 1000 fm. The momentum distribution at this point was obtained from momentum conservation. The starting distance between the TP and LF was obtained based on energy and momentum conservation under the constraint that they should have the same center of mass as the IM. The final kinetic energies were attained by solving the equations of motion iteratively, until the Coulomb potential energy between all particles had been transformed into kinetic energy. The simulations reproduce the analytic results very well, as can be seen in Fig. 17 in Sec. 4.5.1.

4.4.2 Simultaneous decay trajectory simulations

In the simultaneous decay channel, the parameter x_r is varied between 0 and 1. The resulting center-to-center distances x, D and d were calculated as described in Sec. 4.3, and used as a starting configuration for the system. The final kinetic energies were attained by solving the equations of motion iteratively, until the Coulomb potential energy between all particles had been transformed into kinetic energy.

4.5 Results

This section presents the results of the analytic calculations and simulations for ^{235}U(n$_{\text{th}}$,f). Results on ^{252}Cf(sf) can be found in App. A. Those results are in very good agreement with the work of Vijayaraghavan et al.[14].

4.5.1 Sequential CCT results

In the sequential decay channel, the parameters that were varied are the IM excitation energy E^*_{IM}, the amount of prompt neutrons ν, the mass split between the HF and IM, as well as the mass split between the TP and LF. A comparison of analytic and simulated kinetic energies versus mass split for nickel and silicon is shown in Fig. 17. The figure also presents a comparison between the cases when nickel is born on the outside (left figure) and in the middle (right figure). The corresponding Q-values are shown in Fig. 18. There is a good agreement between analytic calculations and simulations. Small differences are due to the fact that simulations have to start and end at a finite potential energy. The mass range was chosen based on the mass resolution reported by FOBOS ($\delta M \approx 6$), centered around ^{68}Ni and ^{34}Si. The parabola-like shape follows directly the Q-value in the fission of the IM. The further away from $^{68-70}\mathrm{Ni} + ^{34-32}\mathrm{Si}$ the mass split is, the less energetically favourable it becomes. The sawtooth-shape is a direct consequence of odd-even staggering. Grids of similar plots with nickel on the outside are composed, where each plot in the horizontal direction varies the mass split between the HF and the IM (Fig. 19), or the amount of prompt neutrons ν (Fig. 20). The plots in the vertical direction vary the IM excitation energy E^*_{IM}. The purpose of these grid plots is to illustrate the difference in kinetic energy when varying all the parameters.

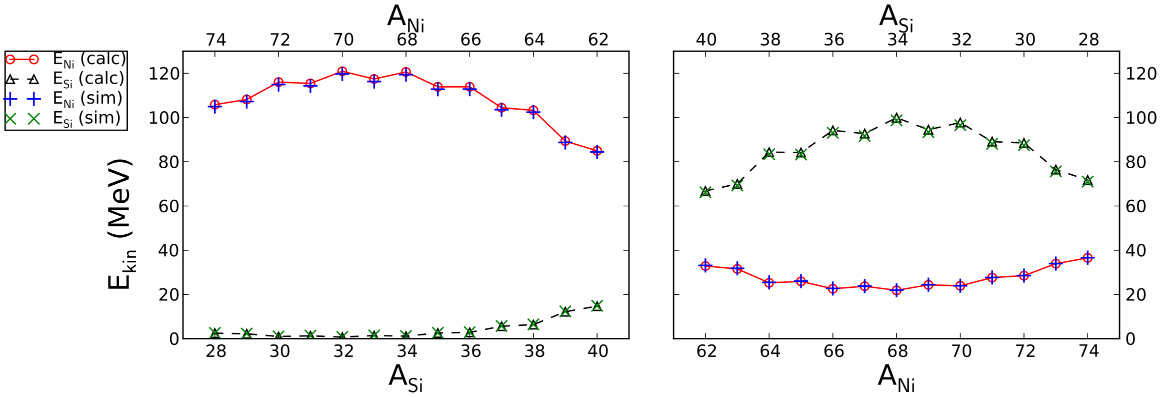

Figure 17: Kinetic energy of nickel (red solid line) and silicon (black dashed line) versus their mass split, in the sequential CCT $^{235}\mathrm{U(n_{th},f)} \rightarrow {}^{132}\mathrm{Sn}+{}^{102}\mathrm{Mo}+2\mathrm{n} \rightarrow {}^{132}\mathrm{Sn}+{}^{A_{\mathrm{Ni}}}\mathrm{Ni}+{}^{A_{\mathrm{Si}}}\mathrm{Si}+2\mathrm{n}$. The IM excitation energy is $E^*_{\mathrm{IM}} = \mathrm{TXE} = 30$ MeV. The kinetic energies were calculated analytically ($\bigcirc$,$\triangle$) and with Monte Carlo trajectory simulations ($+$,$\times$). The nickel is born on the outside (left figure) and in the middle (right figure) of the other two fission fragments.

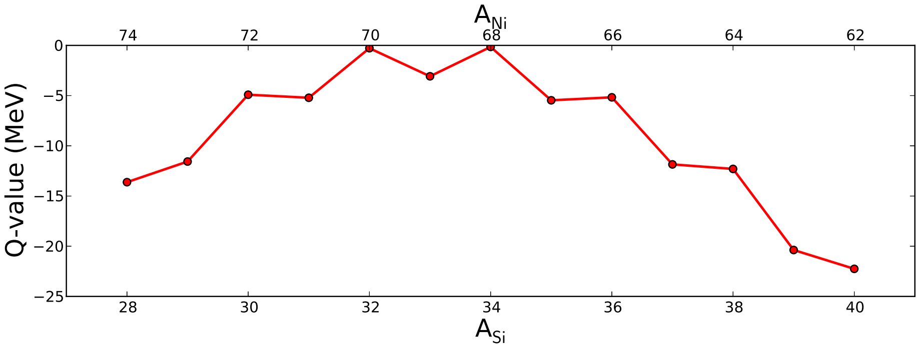

Figure 18: The Q-value versus the mass split between nickel and silicon in the spontaneous fission $^{102}\mathrm{Mo} \rightarrow {}^{A_{\mathrm{Ni}}}\mathrm{Ni} + {}^{A_{\mathrm{Si}}}\mathrm{Si}$. The shape matches the left part in Fig. 17 almost perfectly.

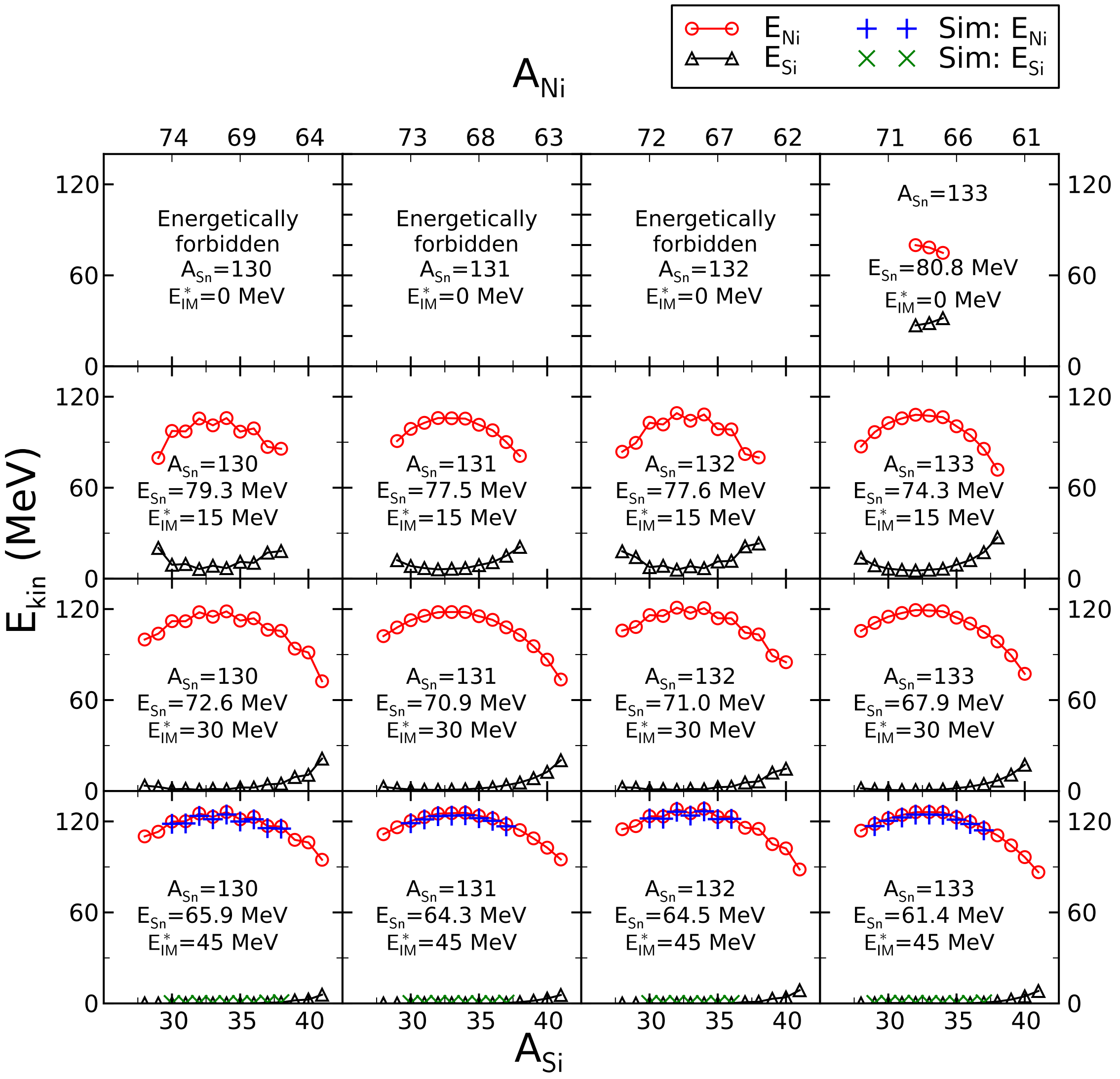

Figure 19: Kinetic energy of nickel (born on the outside) and silicon (born in the middle) versus their mass split, in the sequential CCT $^{235}\mathrm{U}(\mathrm{n_{th}},\mathrm{f}) \rightarrow {}^{A_{\mathrm{Sn}}}\mathrm{Sn} + {}^{A_{\mathrm{Mo}}}\mathrm{Mo} + 2\mathrm{n} \rightarrow {}^{A_{\mathrm{Sn}}}\mathrm{Sn} + {}^{A_{\mathrm{Ni}}}\mathrm{Ni} + {}^{A_{\mathrm{Si}}}\mathrm{Si} + 2\mathrm{n}$. The mass split between the HF and IM is varied in each plot horizontally, and the IM excitation energy $E^*_{\mathrm{IM}} = \mathrm{TXE}$ vertically. The energies are calculated analytically (◯,△) and with Monte Carlo trajectory simulations (+,×). Simulations only show results that are energetically allowed and have a tip distance (Sec. B) at the second scission of ≤ 7 fm.

When varying A_{Sn} or ν, the only noticeable difference is that the sawtooth-shape gets smaller for odd masses of A_{Mo}. When increasing the excitation energy, the TP and LF are allowed to be born closer together, yielding a higher acceleration in the rest frame of the IM. Since the frame itself is moving, the outside fragment will be further boosted, and the inside fragment will be further retarded. Values at the edges are sometimes missing due to negative Q-values or non-existing mass splits. Note that simulation results are missing where the decays are energetically forbidden ($Q_2 + E^*_{\mathrm{IM}} < 0$), or have an unrealistic tip distance (Sec. B) at the

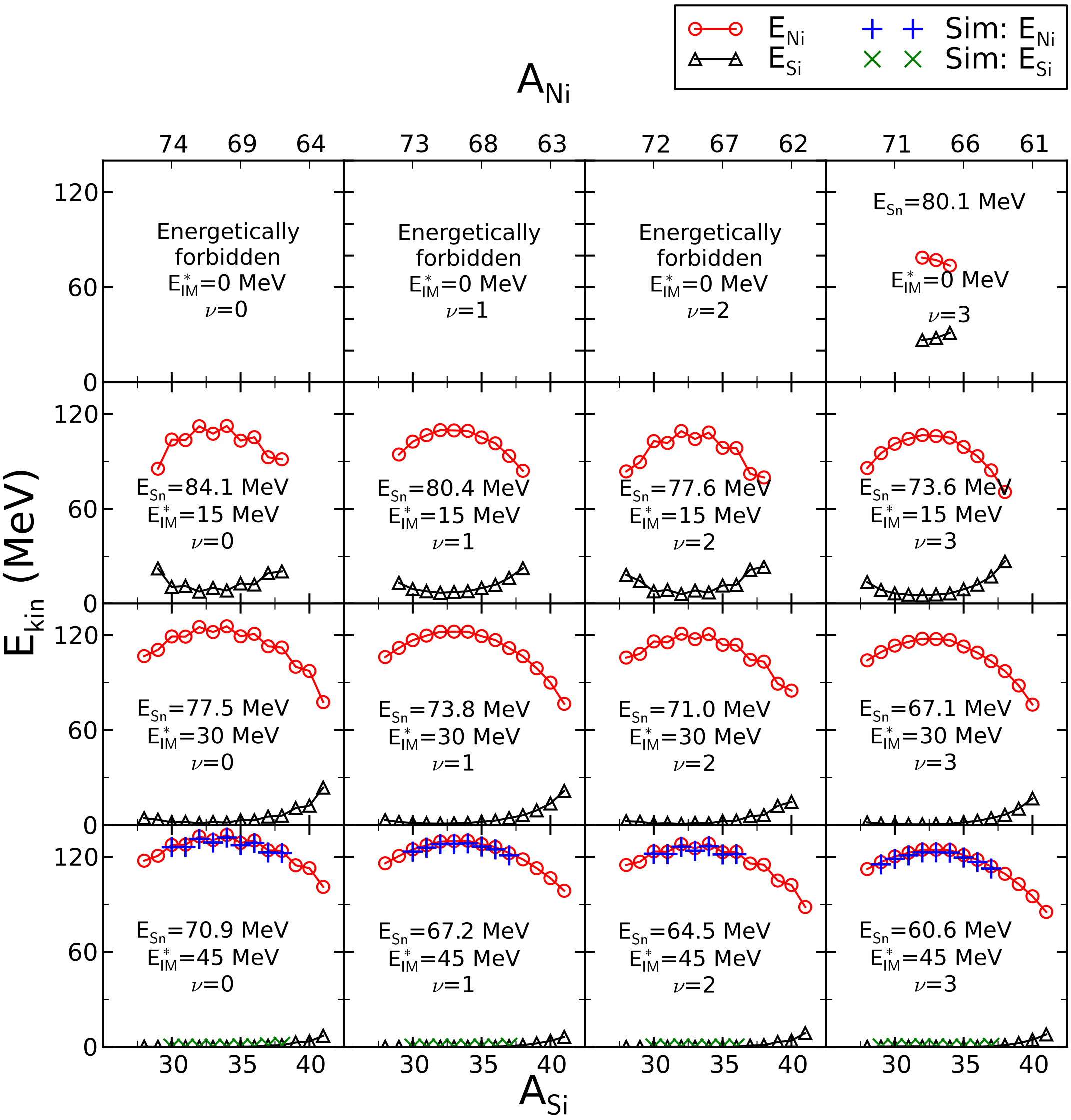

Figure 20: Kinetic energy of nickel (born on the outside) and silicon (born in the middle) versus their mass split, in the sequential CCT $^{235}\text{U}(\text{n}_{\text{th}},\text{f}) \rightarrow {}^{132}\text{Sn} + {}^{A_{\text{Mo}}}\text{Mo} + \nu \rightarrow {}^{132}\text{Sn} + {}^{A_{\text{Ni}}}\text{Ni} + {}^{A_{\text{Si}}}\text{Si} + \nu$. The number of prompt neutrons ν is varied in each plot horizontally, and the IM excitation energy $E^*_{\text{IM}} = \text{TXE}$ vertically. The energies are calculated analytically (○,△) and with Monte Carlo trajectory simulations (+,×). Simulations only show results that are energetically allowed and have a tip distance (Sec. B) at the second scission of ≤ 7 fm.

second scission (≥ 7 fm). A high excitation energy is therefore required for the decays to be allowed. The upper limit of $E^*_{\text{IM}} = 45$ MeV is chosen because at this value, the tip distance between the HF and IM at scission approaches 7–10 fm, an extreme scission configuration which has, to the best knowledge of the author, not been observed in fission[51]. Furthermore, it is very unlikely for one of the fragments to carry a higher excitation energy away, and other modes of de-excitation (especially neutron evaporation) start to become competitive, and shell-effects are vanishing. Most importantly however, at these values the kinetic energy of the silicon starts to become too low to even enter a detector and leave a signal. At such low kinetic energies, both a symmetric and an asymmetric double-armed detector setup would show a clear signature in both detectors, corresponding to the missing ternary particle. This is true both for spontaneous and thermal neutron induced fission. Such an effect was neither seen with the asymmetric setup of the FOBOS experiment, nor the symmetric setup in the experiment by Kravtsov and Solyakin[46]. In Fig. 21, all the results for ^{68}Ni and ^{70}Ni are gathered and shown as a function of mass splits $A_{\mathrm{Sn}} = 128$–134, prompt neutrons $\nu = 0$–4, and excitation energy $E^*_{\mathrm{IM}} = 0$–45 MeV. Missing data points in the lines correspond to $Q_2 + E^*_{\mathrm{IM}} < 0$. Even unphysical tip distances are displayed. In Fig. 22, the area that all the results for ^{68}Ni and ^{70}Ni spans is shown. The only data points missing are the energetically forbidden ones ($Q_2 + E^*_{\mathrm{IM}} < 0$). Again, even results for unphysical tip distance values are displayed. All the data series follow the same trend, quickly rising for low excitation energies but then leveling off. Prompt neutrons carry away energy, effectively lowering the curves. The system ^{132}Sn + ^{70}Ni + ^{34}Si has the highest kinetic energy, as it has the highest Q-value. In addition the figure shows the highest and lowest kinetic energies measured in the Lohengrin experiment (thick solid lines). The possible kinetic energies of nickel are well within these limits. A similar plot is shown in Fig. 23, but where the silicon is born on the outside and the nickel on the inside. Again, it has to be stressed that there is no reason to believe that this represents the majority of the CCT decays, should it exist. The nickel is hardly covered at all, but the majority of the silicon is covered. Low/high excitation energies are either energetically forbidden, or correspond to unphysical conditions (see Sec. 4.6.2). Due to high statistics and acceptance, Lohengrin would still detect the silicon. Quantum mechanical fluctuations are expected to further increase the acceptance (see Sec. 4.6).

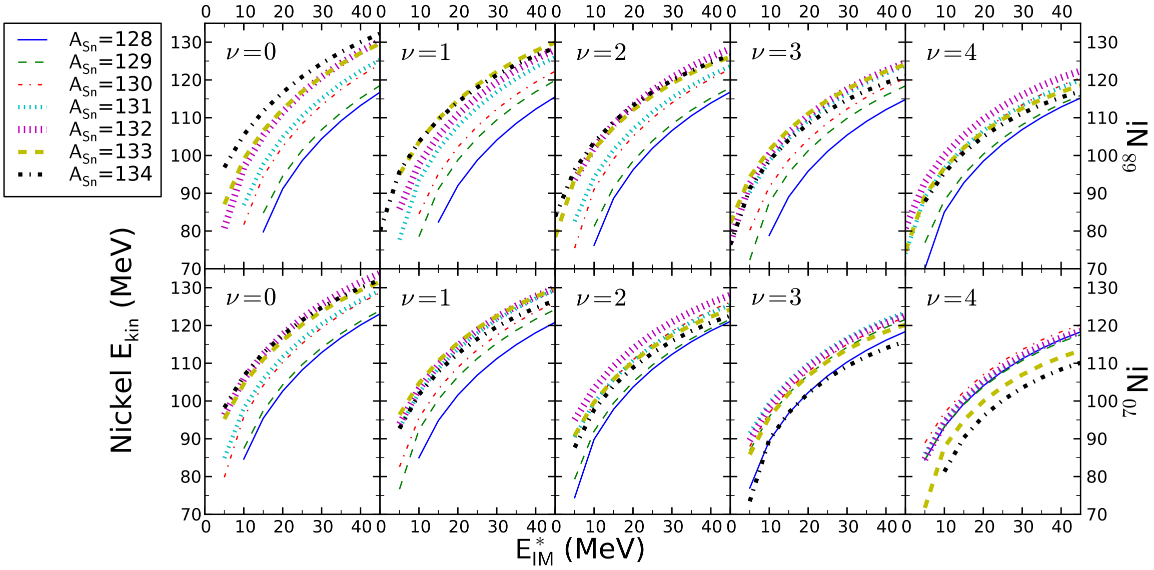

Figure 21: Nickel kinetic energy versus IM excitation energy, with varying mass splits, prompt neutron multiplicity and excitation energy. The results are for the sequential CCT model, when nickel is born on the outside. Note that the ordinate does not start at zero MeV.

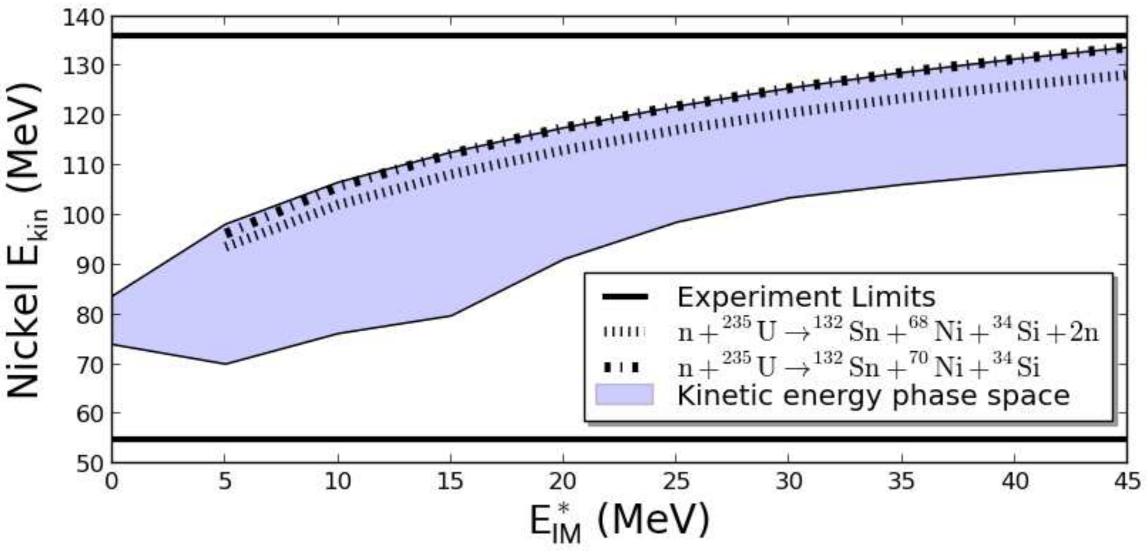

Figure 22: Area of all ^{68,70}Ni kinetic energies versus IM excitation energy. The area is spanned by varying the mass $A_{\mathrm{Sn}} = 128$–134, prompt neutron multiplicity $\nu = 0$–4 and IM excitation energy $E^*_{\mathrm{IM}} = 0$–45 MeV. The results are for the sequential CCT model, when nickel is born on the outside. The experimental limits of the Lohengrin measurements are shown. The corresponding silicon kinetic energies are plotted in Fig. 27 in Sec. 4.6.2. Note that the ordinate does not start at zero MeV.

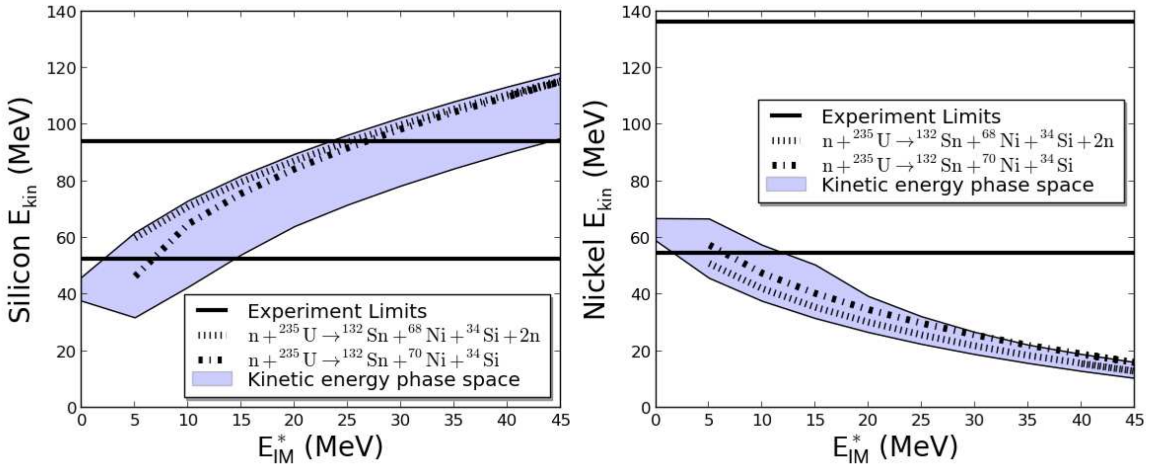

Figure 23: Area of all ^{34,36}Si (left) and ^{68,70}Ni (right) kinetic energies versus IM excitation energy. The area is spanned by varying the mass $A_{\mathrm{Sn}} = 128$–134, prompt neutron multiplicity $\nu = 0$–4 and IM excitation energy $E^*_{\mathrm{IM}} = 0$–45 MeV. The results are for the sequential CCT model, when nickel is born on the inside and silicon on the outside. The experimental limits of the Lohengrin measurements are shown. Low/high excitation energies are not expected, as they are either energetically forbidden, or correspond to unphysical conditions (see Sec. 4.6.2). Due to high statistics and acceptance, Lohengrin would still detect the silicon.

4.5.2 Simultaneous CCT results

In the simultaneous decay, the parameters varied are the TP relative starting position x_r, the systems total excitation energy TXE, the prompt neutron multiplicity ν, the mass split between the fragments. In Fig. 24, the fragment kinetic energies are plotted against x_r, which is varied between $x_r = 0$ and $x_r = 1$ corresponding to the TP touching the HF and LF respectively. The configuration leading to the highest and lowest nickel kinetic energies occur when the TP is born close to the HF and LF respectively. The silicon ends up with virtually no kinetic energy, since it is confined between the Coulomb potentials of the two other fragments. If CCT was a simultaneous decay, both a symmetric and an asymmetric double-armed detector setup would therefore show a clear signature in both detectors, corresponding to the missing ternary particle. In Fig. 25 the fragment kinetic energies are plotted versus the total excitation energy TXE of the system. By also varying the TP starting position x_r, the resulting kinetic energies are represented by areas. Note that for long range alphas (LRA), the average TXE is about 16 MeV and rarely higher than 17 MeV[52], and that it decreases with increased ternary particle mass[53]. In the present scenario, the TP ^{34}Si is heavier than any previously observed TP in ^{235}U(n$_{\mathrm{th}}$,f), thus a TXE over a few MeV is not expected. Furthermore, the LF and HF are born at unphysically large distances as TXE goes to 45 MeV. The kinetic energies decrease for increased TXE, since the particles are forced to be born further apart, and there is less energy in the system that can be converted into kinetic energy. In Fig. 26, the nickel kinetic energy is again plotted against the total excitation energy with varied x_r, but now the mass split and amount of prompt neutrons are also varied. This gives a kinetic energy area for each value of x_r. The physically reasonable configurations, when the TP is born at the geometric center between the HF and LF, or when it is born at the electrostatic saddle point (x_s), are well within the experimental limits. The limits include energy dispersion, as well as target and nickel foil losses. The kinetic energies are well covered even without taking these effects into account.

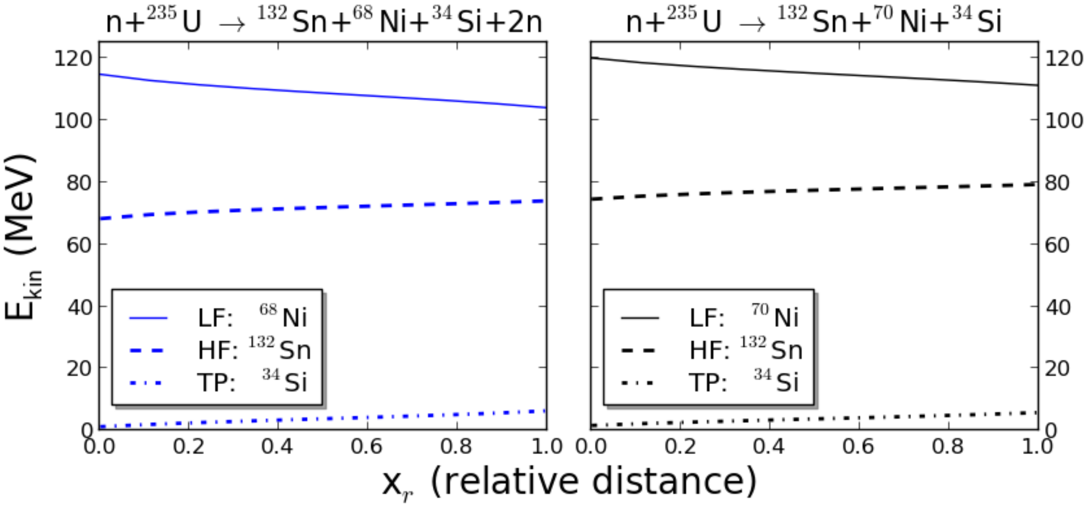

Figure 24: Fragment kinetic energies versus the TP relative starting position x_r. When $x_r = 0$ and $x_r = 1$, the TP starts touching the HF and LF respectively. The fissioning system in the right figure has a higher Q-value, which is why its total kinetic energy is also higher.

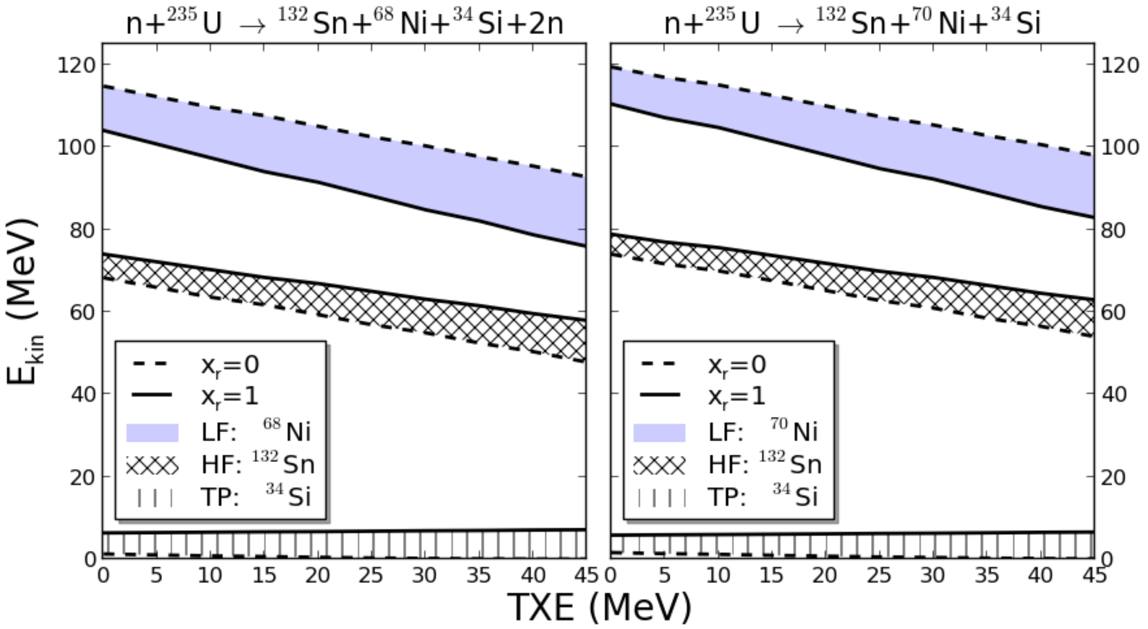

Figure 25: Fragment kinetic energies versus total excitation energy of the system. The areas are spanned by varying the TP relative starting position x$_r$ from 0 (dashed line) to 1 (solid line).

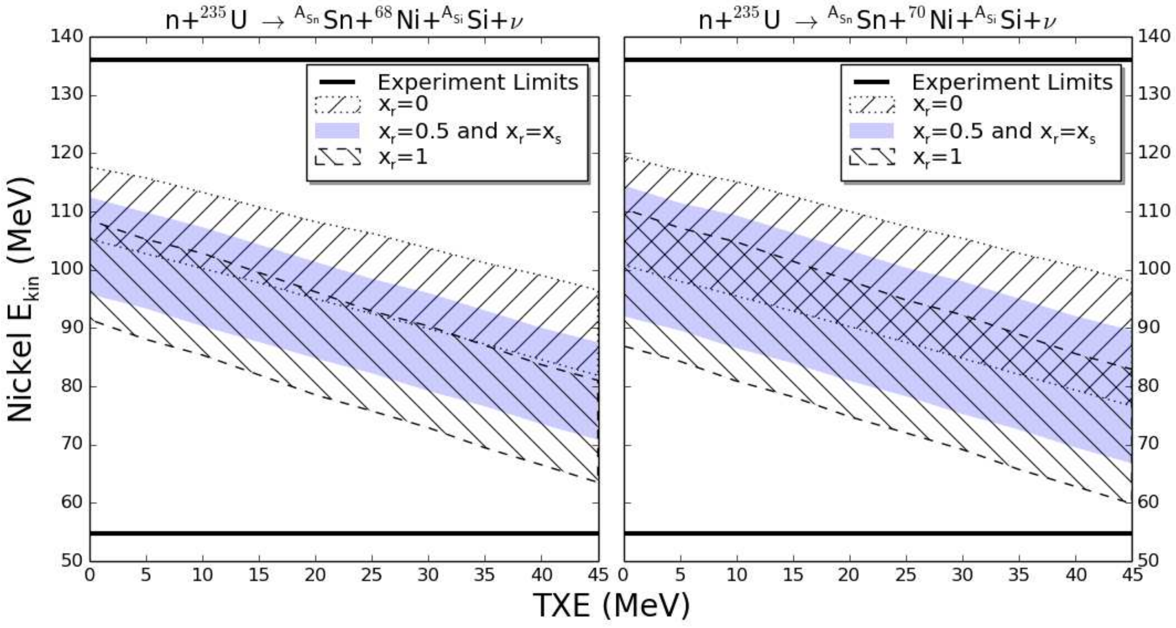

Figure 26: Nickel kinetic energy versus the total excitation energy of the system. The areas in the figure correspond to the TP being born touching the HF (x$_r$ = 0), at the geometric center and at the electrostatic saddle point (x$_r$ = 0.5 and x$_r$ = x$_s$), and born touching the LF (x$_r$ = 1). The areas span all the possible mass splits $A_{\mathrm{Sn}} = 128$–134, $A_{\mathrm{Si}} = 28$–42, and prompt neutron multiplicity $\nu = 0$–4. Note that the ordinate does not start at zero MeV.

4.6 Discussion

This section discusses the CCT kinematics results and their implications, as well as emphasizes some of the difficulties in the CCT model.

4.6.1 Discussion of the results

The sequential decay results show that the nickel kinetic energies are fully covered in the LOHENGRIN experiment, when the light fragment is born on the outside. When it is born on the inside, the majority of the silicon kinetic energy distribution is covered. If CCT existed in the latter decay channel, there should be a clear signature in the LOHENGRIN experiments due to the high statistics. The models used are purely classical, no mention of quantum mechanics is made. The models should still be valid, as they are based on momentum and energy conservation. Taking into account quantum mechanics should add a spread around the derived values, increasing the acceptance of the experiment, thus making it easier to detect the nickel and the silicon fragments. In the simultaneous decay channel, the nickel kinetic energy distribution is fully covered. In both the sequential and simultaneous decay channels, the TP kinetic energy is extremely low when the conditions for CCT are met (confirmed by von Oertzen and Nasirov[54]). The TP would not be able to leave a clear signal in a detector, or at the very least be very easy to discriminate from the light fragment in a correctly designed experiment, due to the highly differing energies and velocities. Both a symmetric and asymmetric double-armed detector setup would therefore show a clear signature in both detectors in a mass versus mass spectrum, corresponding to the missing energy of the non-observed ternary particle. An experiment with a similar setup to that of the FOBOS experiment was carried out by Kravtsov and Solyakin[46], which had no target backing, giving a fully symmetric setup. This experiment reported no indication of CCT.

4.6.2 CCT model inconsistencies

Although the CCT decay has a positive Q-value in the end, the second fission of the IM is highly unfavourable energetically, due to a negative Q-value. Even if this is compensated for by excitation energy, it does not mean that the IM will always fission. The IM also has to overcome a potential barrier, and the probability of the IM to fission depends on the barrier penetrability. The fissility of the IM is much lower than that of usual fissioning systems ($Z^2/A < 17$ for ^{104}Mo). In fact, fission of ^{102,104}Mo (or ^{120}Cd) has never been observed. Consequently a high excitation energy is required to enable fission of the IM, and the lowest E^*_{IM} shown in Fig. 21 would not lead to CCT. On the other hand, CCT poses very conflicting requirements on the excitation energy. At high excitation energies fission competes with other de-excitation modes like neutron emission, thus reducing the likelihood of CCT events considerably. A high excitation energy also effectively reduces the final kinetic energy of the ternary particle to close to zero MeV. This is seen throughout the results (in particular in Fig. 19 and Fig. 20, and it is confirmed by Vijayaraghavan et al.[14]). The reduction in kinetic energy as a consequence of increased excitation energy is seen in Fig. 27. For such low kinetic energies, the TP would either always be missing from the detectors, or at least be very easy to discriminate from the LF. In other words, if CCT existed, it should have been seen in countless experiments before. There are even more conflicting requirements on the excitation energy if the tip distance is taken into account. There is a competition between the first and the second fission to have a narrow configuration, as seen in Fig. 28 (calculated according to App. B). The figure illustrates that a high excitation energy is required for a physically reasonable tip distance at the second scission of the IM, but this increases the tip distance at the first scission of the FS. The nuclear potential could not be responsible for bringing the particles closer together at scission, as it vanishes quickly at about 2 fm.

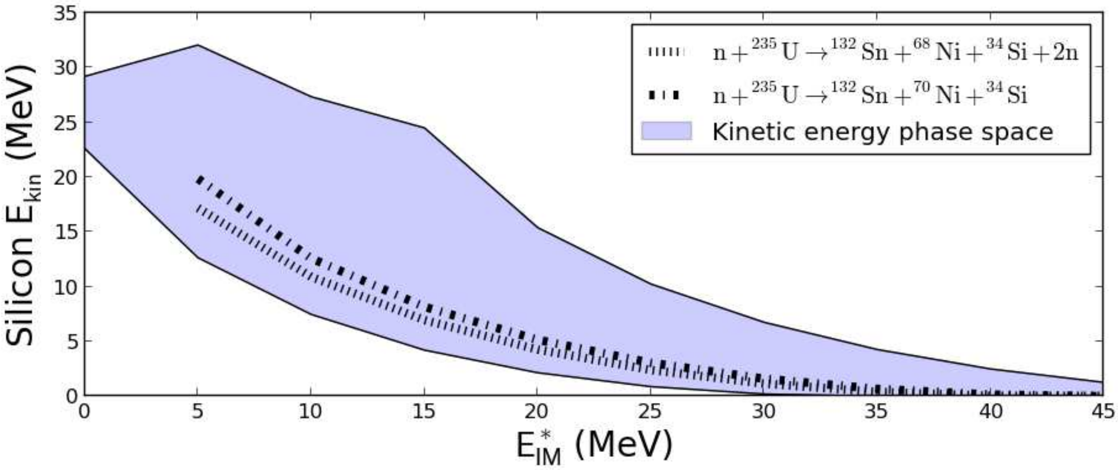

Figure 27: Area of all possible ^{34,36}Si kinetic energies versus IM excitation energy. The area is spanned by varying the mass split $A_{\mathrm{Sn}} = 128$–134, prompt neutron multiplicity $\nu = 0$–4 and IM excitation energy $E^*_{\mathrm{IM}} = 0$–45 MeV. The results are for the sequential CCT model, when nickel is born on the outside and silicon on the inside. For higher excitation energy, the ternary particle would barely be able to leave a signal in a regular detector.

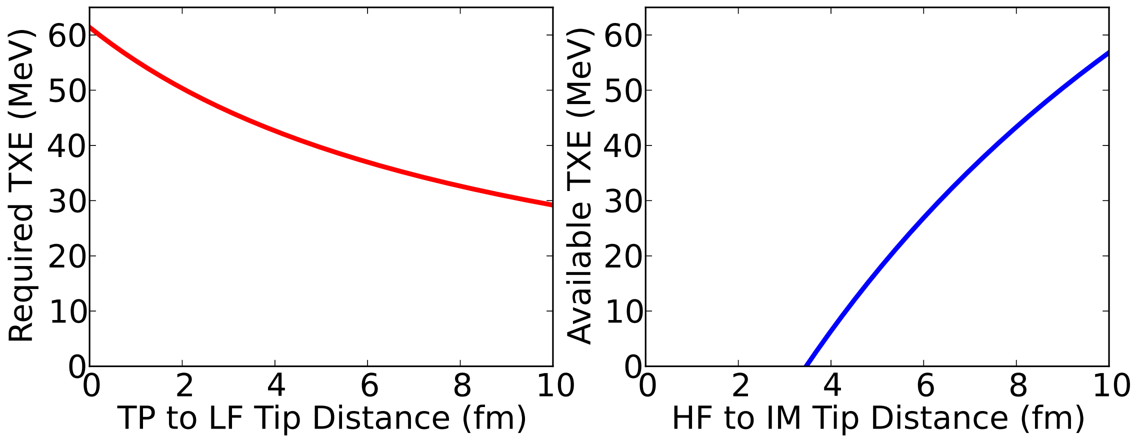

Figure 28: Required excitation energy versus tip distance at scission of the IM (left), and the available excitation energy versus tip distance at the first scission (right). The system is $^{235}U(n_{th},f) \rightarrow {}^{132}Sn + {}^{102}Mo + 2n \rightarrow {}^{132}Sn + {}^{68}Ni + {}^{34}Si + 2n$. The figure illustrates the difficulty in keeping both tip distances reasonable. Any pre-scission kinetic energy would raise the required/lower the available excitation energy accordingly.

Pre-scission kinetic energy poses another problem for CCT. If there is any pre-scission kinetic energy, energy conservation either forces the excitation energy to be lower, or the initial tip distance to be higher. Any of these conditions makes it harder to realize CCT. Furthermore, all neutrons were considered to be prompt neutrons in the calculations. If these neutrons should instead originate from evaporation, they would directly lower the excitation energy (by about 10 MeV per evaporated neutron), and possibly influence the collinearity of the system due to the small, but non-negligible, recoil. In binary fission, evaporated neutrons are responsible for spreading the fragments by approximately 2°. This lowering of the excitation energy would make it harder to realize CCT. The collinearity of the decay would be further threatened by angular momentum. In spontaneous fission, there is no initial angular momentum. In thermal neutron-induced fission of uranium, there is a small contribution of p-wave capture, with non-zero angular momenta. Such states could de-couple the fission axes of the first and the second sequential decays, leading to non-collinear events.

4.6.3 Instability of collinearity

The discussion so far has shown that the decay into CCT is improbable. Furthermore, collinearity itself is extremely improbable in a simultaneous three-body decay, since it occurs at an unstable equilibrium point. The slightest deviation in the TP position or momentum direction from the fission axis would break collinearity. The stability of collinearity is examined in Fig. 29 as a function of the TP offset from the fission axis (with zero initial momenta), and in Fig. 30 as a function of the TP kinetic energy perpendicular to the fission axis (when all fragments are born collinearly). For the final angle to be $\leq 2°$, the TP can deviate no more than $y_{\mathrm{max}} \approx 0.1$ fm from the fission axis, or have a kinetic energy above $E_{\mathrm{max}} \approx 10^{-4}$ MeV.

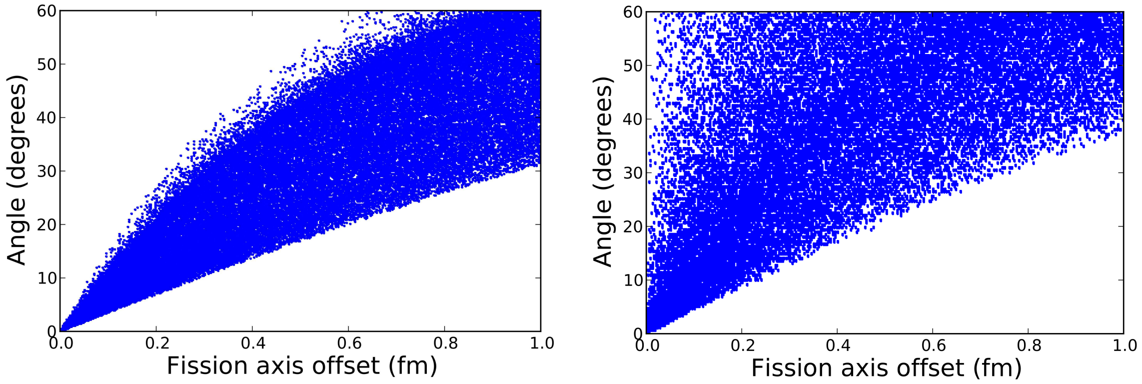

(a) TP initially closer to LF.

(b) TP initially closer to HF.

Figure 29: Scattering angle between the LF and TP, versus TP offset from the fission axis. The data was generated from $> 10^6$ particle trajectories simulated using a Monte Carlo approach (see Sec. 4.4 for details). The initial configurations were generated by varying the LF to HF distance between the energetically closest possible up to an additional 50 fm, the TP offset between the HF and LF, and the TP offset from the fission axis between 0–1 fm. All initial momenta was zero. The figure shows the extreme instability of collinearity, due to the dominantly repulsive interaction after scission. The region close to the HF is more unstable due to the stronger repulsion.

From a quantum mechanical perspective, it seems rather unlikely that both the position and momentum should be constrained in such a narrow region. The uncertainty principle gives

$$\frac{y_{\mathrm{max}}p_{\mathrm{y,max}}}{\hbar} = \frac{y_{\mathrm{max}}\sqrt{2E_{\mathrm{max}}M(^{34}\mathrm{Si})}}{\hbar} \approx 0.00128 \ll \frac{1}{2} \leq \frac{\Delta y \Delta p_y}{\hbar}. \tag{27}$$

Note that a combination of both offset and momentum at the same time reduces the threshold significantly, as does introducing the second off-axis dimension. This gives a hint that the required constraint imposed by collinearity is very improbable from a quantum mechanical point of view.

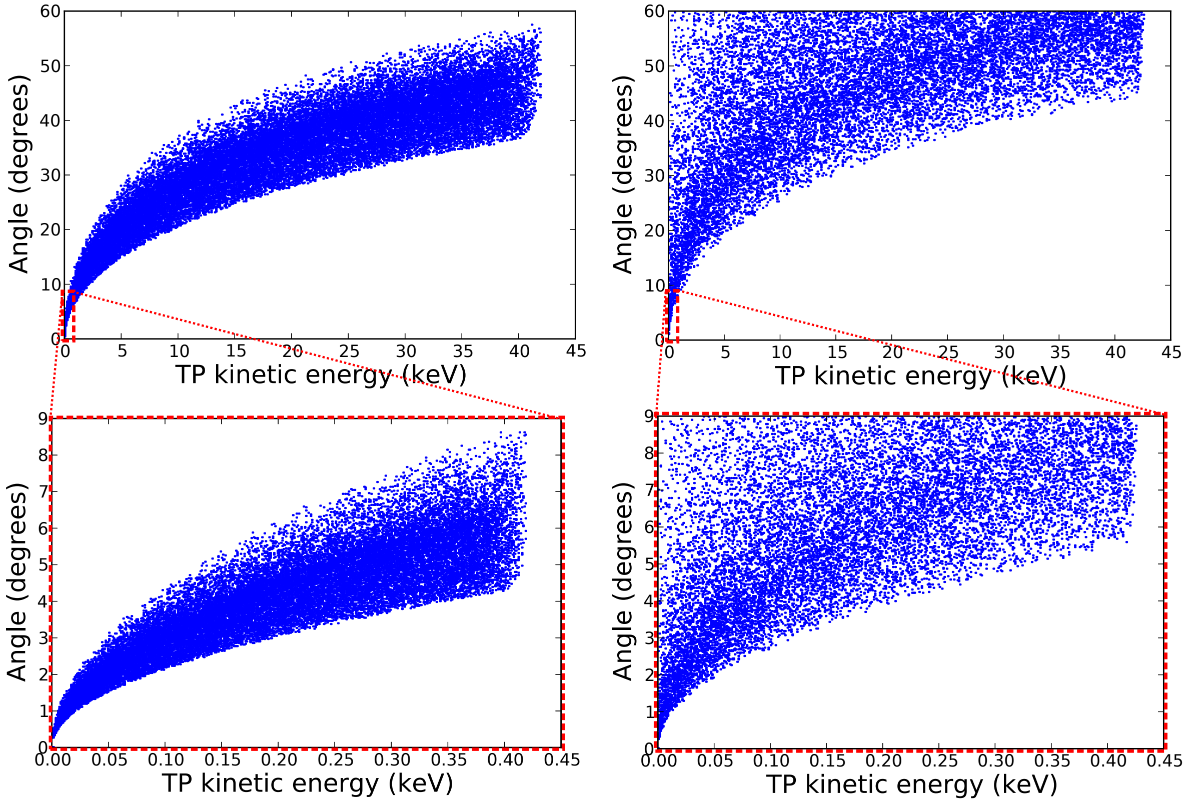

Figure 30: Final scattering angle between LF and TP, versus TP kinetic energy perpendicular to the fission axis. The data was generated from $> 10^6$ particle trajectories simulated using a Monte Carlo approach (see Sec. 4.4 for details). The initial configurations were generated by varying the total kinetic energy perpendicular to the fission axis between 0 and 0.05 MeV (top figures) and 0 and 0.0005 MeV (bottom figures). Note that the energy in the figure is given in keV. Initially, all particles were set collinearly, and the momenta along the fission axis were set to zero. Conservation of energy, linear momentum and angular momentum then fully determines the particle initial momenta away from the fission axis. Additionally, the LF to HF distance was varied between the energetically closest possible configuration up to an additional 50 fm, and the TP offset between the HF and LF was varied. The left and right figure shows events where the TP is born closer to the LF and HF, respectively. The figure shows the extreme instability of collinearity, due to the dominantly repulsive interaction after scission. The region close to the HF is more unstable due to the stronger repulsion.

5 LOHENGRIN experiments

Lohengrin[16,55] is to date the most sensitive spectrometer for measurement of neutron-induced fission products, enabling accurate studies of fission yields down to 10^{-10} [18,19]. It uses both electrostatic and magnetic fields to separate fission fragments of actinide targets exposed to neutrons from the high-flux reactor of the Institut Laue-Langevin (ILL) in Grenoble, France. Lohengrin (see Fig. 31) is used to determine the fission fragment yields[7,6,56], kinetic energy, mass and ionic charge distributions. It also acts as a radioactive ion beam facility for nuclear spectroscopy of exotic neutron-rich nuclei[57]. In this work, Lohengrin was used to determine upper limits of the yield of fission fragments compatible with CCT in ^{235}U(n$_{\text{th}}$,f).

5.1 Experimental setup and data acquisition

Lohengrin is a single-arm spectrometer that covers a small solid angle of a fission target. Fission fragments emitted under this angle goes through a static dipole magnet and an electrostatic dipole, which separate fragments according to their mass over ionic charge ratio, and kinetic energy over ionic charge ratio, respectively[58,17]. An ionization chamber (IC) is used to measure the nuclear charge and kinetic energy of the fission fragments. The total flight time from target to IC is below 2 μs, which is why decay losses of the studied fragments with half-lives longer than milliseconds can be neglected. This section covers a detailed description of the setup of the instruments, which is followed by calibration and data analysis.

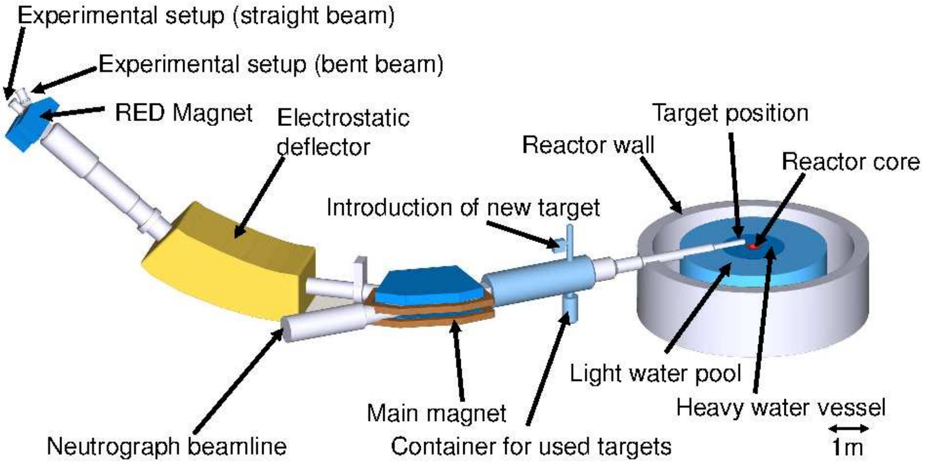

Figure 31: Schematic view of the Lohengrin recoil separator.

5.1.1 Target

A fissile actinide target[59] is placed in a vacuum tube 50 cm from the 58 MW ILL reactor core. There it is exposed to a thermal neutron flux of $5 \cdot 10^{14}$ s^{-1}cm^{-2}. The target is deposited as an oxide on a platinum-coated titanium backing. These backing materials were chosen for several reasons, in particular to

- decrease diffusion of actinide atoms into the backing,

- provide stability at high temperatures and
- provide high emissivity and low activation by thermal neutrons.

Apart from diffusion, it is also possible for target atoms to get sputtered by collision with fission products out into the vacuum. To reduce this effect, a 0.25 μm thick nickel foil is used to cover the target. The actinides chosen need to have a high isotopic purity to provide a clearly defined fissioning system. This is because measurements are not done of fission fragments in coincidence at LOHENGRIN, but rather of single fragments. Discrimination between fragments originating from binary and ternary fission is still possible due to the widely different kinetic energy distributions (see Sec. 2). In the present experiment $^{235}UO_2$ targets enriched to an abundance greater than 99% ^{235}U were used. Targets had a length of 7 cm, a width of $0.3 - 0.8$ cm, and a thickness of $144 - 240$ μg/cm^2. The size of the target greatly affects the resolution and performance of the measurements. This is further elaborated in Sec. 5.1.5.

5.1.2 Fission fragment ionic charge

Fission fragments are highly accelerated due to the large energy released. A fast moving atom loses electrons upon interaction with matter. Electrons occupying higher orbitals are stripped with a higher probability than electrons in lower orbitals, as are electrons in a faster moving fission fragment. Lighter fragments, like ternary helium for example, is completely stripped of electrons when going out of the target. A quantity known as the ionic charge is introduced, defined as

$$q = Z - n_e, \tag{28}$$

where Z is the number of protons and n_e the number of remaining (non-stripped) electrons. Binary fission fragments in the LOHENGRIN separator typically have an ionic charge of $q = 21$. It is vital to determine the ionic charge since it affects the fission fragment deflection in the electric and magnetic field. The ionic charge is not definite for one species of fission fragments, but rather a distribution since the electron stripping is a probabilistic process that depends on many variables. The average ionic charge $\bar{q}$ and its spread σ_q for a certain fission product is determined by measuring with several separator settings and by fitting to the empirical ionic charge distribution models of Nikolaev and Dimitriev[60] and Shima[61] [62]. In this experiment, the fitting parameters were extracted by reproducing the measured ionic charge-state of ^{80}Ge and ^{58}Ni.

5.1.3 Main magnet

The vacuum tube leads from the target to the main magnet[58,17] of LOHENGRIN, which is a static dipole magnet whose basic properties are illustrated in Fig. 32. A charged particle moves in a circular path in a magnetic field due to the Lorentz force. The curvature of this path is related to the magnetic rigidity of the particle, which is defined as the ratio p/q where $p = mv$ is the momentum and q the ionic charge of the particle. A stronger magnetic field or lower momentum over ionic charge leads to a higher curvature. By equating the Lorentz force with the centripetal force,

$$eqvB = \frac{mv^2}{\rho_m}, \tag{29}$$

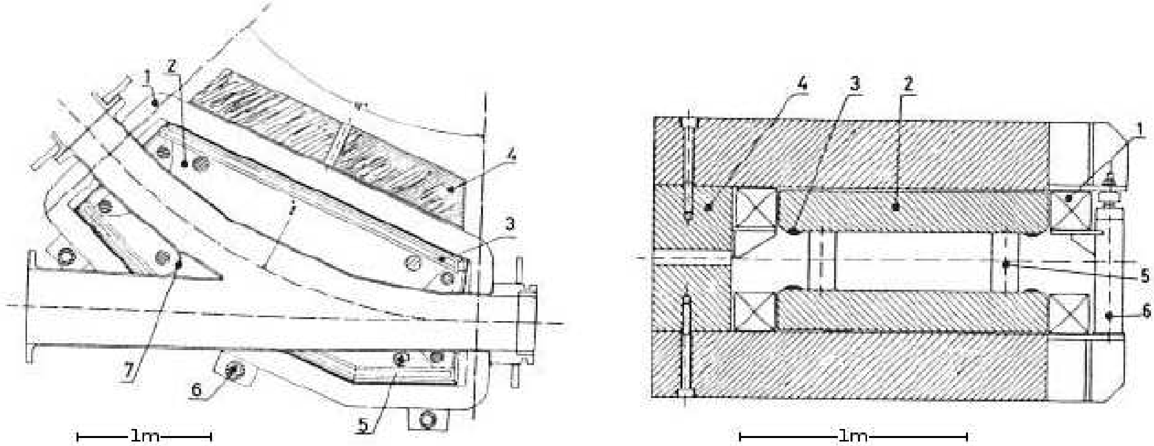

Figure 32: Longitudinal view (left) and cross-sectional view (right) of the main magnet. (1) Coils, (2) pole plates, (3) shims, (4) C-shaped yoke, (5) spacer for the pole plates, (6) support for the C-shaped yoke, (7) Y-Shaped vacuum chamber for the magnetic field.

and rewriting, the magnetic rigidity can be extracted as

$$B\rho_m e = \frac{mv}{q} \equiv \frac{p}{q}. \tag{30}$$

Here $\rho_m = 4$ m is the magnet bending radius, e is the elementary charge and B is the magnetic field strength. By adjusting the magnetic field, it is possible to separate particles according to their p/q ratio. Typical magnetic field strengths used are $B = 0.1 - 0.24$ T.

5.1.4 Electrostatic dipole

The fragments separated by the magnetic dipole enters an electrostatic dipole which consists of two cylindrical concentric electrodes[58,17] (illustrated in Fig. 33). An electric field is generated by applying a voltage difference between the electrodes. The electrostatic dipole separates particles according to their E/q ratio, where $E = E_{kin} \equiv \frac{mv^2}{2}$ is the kinetic energy. This is seen by setting the centripetal force equal to the Coulomb force

$$\frac{mv^2}{\rho_e} = eq\,|\vec{\epsilon}| = eq\frac{2U}{d}, \tag{31}$$

and rewriting as

$$\frac{E_{kin}}{q} = \phi U. \tag{32}$$

Here $\phi \equiv \frac{e\rho_e}{d}$ is a parameter to be calibrated for the precise plate separation distance d (≈ 0.3 m). The bending radius is $\rho_e = 5.6$ m, and $\vec{\epsilon}$ is the electrostatic field. The maximum theoretical potential is $U_\pm = \pm 380$ kV, but measurements rarely go over $U_\pm = \pm 330$ kV due to the increased difficulty in keeping the instrument stable at such voltages. The potential limits the E/q ratio directly. Setting $U = 330$ kV in Eq. (32) gives an upper limit of $E/q =$ 6.16 MeV/charge. Ions with higher energy per charge state cannot be measured at this voltage.

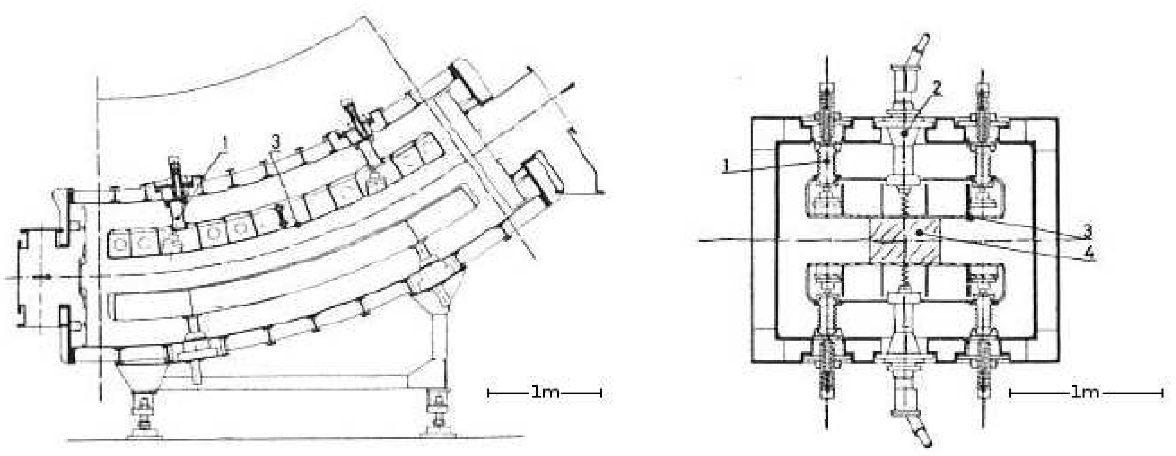

Figure 33: Longitudinal view (left) and cross-sectional view (right) of the electrostatic dipole. (1) Isolators supporting the deflection plates, (2) high voltage feed-throughs for ±400 kV, (3) deflection plates, (4) beam cross section (hatched area).

5.1.5 Combined field effects

The fringe fields of the magnet and electrostatic dipole act as a double focusing parabola spectrometer. The magnet and electrostatic dipole deflection are in the horizontal and vertical plane relative to the beam direction, respectively. The result is a 1:1 non-magnifying ion-optical system, where the focal lengths are matched to allow for the correct focusing (see Fig. 34). The resulting beam is thus an image of the target, which has the effect that the energy and mass resolution is directly linked to the length and width of the target respectively. Fragments with energy E_0 and $E_0 + \Delta E$, emitted from the same point in the target, are separated at the image by a distance Δx. For small values of the energy difference $\Delta E \ll E_0$, there is a linear relationship

$$\Delta x = D_e \frac{\Delta E}{E}, \tag{33}$$

where $D_e = 7.2$ m is the energy dispersion. The energy resolution is then

$$\frac{\Delta E}{E} = \frac{\Delta x}{D_e}. \tag{34}$$

A typical target length is 7 cm, which gives an energy resolution of 1%. A smaller target gives a higher resolution but a lower intensity, since the fission rate is lower. Similarly the mass dispersion relation is

$$\Delta y = D_m \frac{\Delta m}{m}, \tag{35}$$

where Δy is the spread in the image due to a mass difference Δm from the reference mass m, and $D_m = 3.24$ m is the mass dispersion. The mass resolution is

$$\frac{\Delta m}{m} = \frac{\Delta y}{D_m}. \tag{36}$$

Again, a narrower target gives a better mass resolution but a lower intensity. The conclusion is that a large target is chosen in cases where intensity is favoured over resolution.

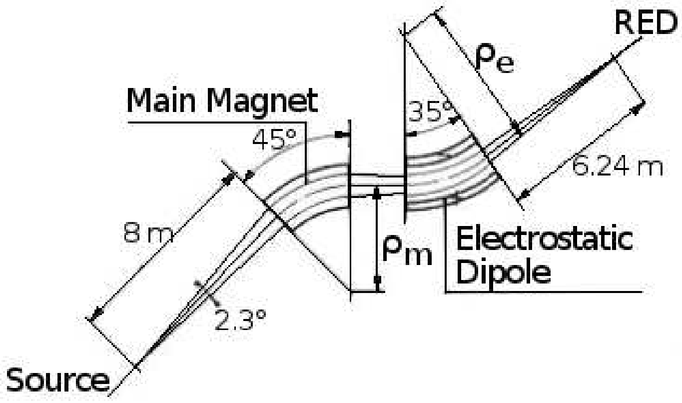

Figure 34: Ion-optical scheme of the spectrometer. The bending radius of the main magnet and electrostatic dipole are $\rho_m = 4$ m and $\rho_e = 5.6$ m, respectively. An additional refocusing magnet, called the Reverse Energy Dispersion (RED) magnet (Sec. 5.1.6), is placed in the image of the target.

An effect of the setup is that ions in the beam are constrained to parabolas. This is seen by combining Eq. (29) with Eq. (32) and plotting the electrostatic versus magnetic deflection (Fig. 35). The velocity of outgoing particles is constrained to

$$v = \frac{2\rho_e U}{B\rho_m d}, \tag{37}$$

and the mass over ionic charge to

$$\frac{m}{q} = \frac{(B\rho_m)^2 de}{2U\rho_e} = \chi\frac{B^2}{U}, \tag{38}$$

where χ is a parameter of the magnet, defined as

$$\chi \equiv \frac{\rho_m^2 de}{2\rho_e}. \tag{39}$$

This is a parameter that needs to be calibrated for the target position. More information about the field settings can be found in Appendix A.2 of U. Köster 2000[7].

5.1.6 Reverse Energy Dispersion magnet

A fission fragment that has an energy dispersion of 10 MeV is spread over a 70 cm length at the focal plane. For certain applications it is more important to have a high ion rate per area rather than the utmost energy resolution. For example, in decay spectroscopy the ions should arrive in a small area of a few cm^2 that can be covered more efficiently by detectors. For this purpose an optional second magnet has been added, which refocuses 40 cm^2 of the mass parabola to a smaller size of a few cm^2. Hence it is named Reverse Energy Dispersion (RED) magnet[63]. It operates up to $B = 1.6$ T, and was used in this experiment to increase the energy acceptance to $\Delta E/E = 2.4\%$.

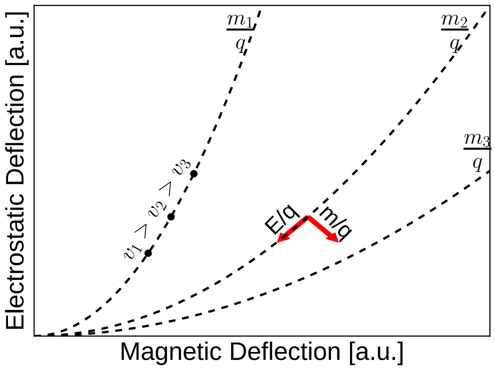

Figure 35: Electrostatic deflection (related to E/q) versus magnetic deflection (related to p/q). Particles with different m/q lie on different parabolas, where the higher ratios are located closer to the x-axis ($m_1/q < m_2/q < m_3/q$). The closer a point on a parabola is to the origin, the higher the velocity is. Therefore variations in E/q and m/q follow the parabola tangent and normal vectors, respectively (shown by arrows).

5.1.7 Ionization chamber

The main magnet and the electrostatic dipole constrain the speed v and the ratio m/q for the incoming fission fragments. Due to different ionic charges, the mass and energy are not uniquely defined, as different masses can satisfy the ratio with different q. An ionization chamber (IC) is placed in the focus of the spectrometer to measure the energy loss ΔE and the total energy E_{tot} with an intrinsic resolution below 1 MeV. The instrument is illustrated in Fig. 36. The IC has two electrodes separated by a gap filled by a "counting" gas (isobutane in this case), which is easily ionized by incoming radiation. A voltage difference is applied between the electrodes, generating an electric field across the gas. Disassociated electrons and ion pairs generated in the ionized gas are separated by this field and drift to the electrodes of opposite polarity. The current of the electrons collected on the anode is amplified, integrated and transformed into a voltage signal that is proportional to the collected charge, i.e. the

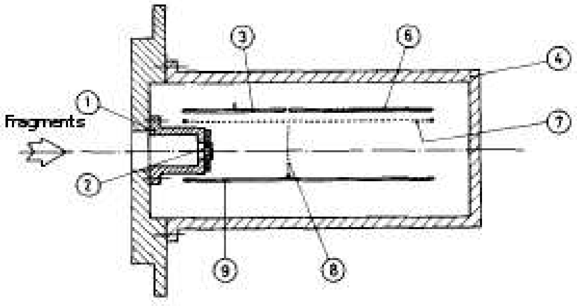

Figure 36: Side view of the ionization chamber. (1) Window holder, (2) entrance windows, (3) ΔE part of the anode, (4) IC housing, (6) E_r part of the anode, (7) Frisch grid, (8) separation grid located below the splitting of the anode, (9) cathode. (Adapted from Bocquet et al.[64] and Hesse et al.[65].)

number of created electron-ion pairs, and hence to the energy deposited in the counting gas. Corrected for the small energy loss in the entrance window, the energy measured in the ionization chamber is identical to the energy E selected by the LOHENGRIN spectrometer, provided the gas pressure is set sufficiently high to stop the ions in the IC completely. Hence this independently measured energy resolves the E/q ambiguity and defines for each incoming ion the charge q it had in the spectrometer. Consequently the mass m is also uniquely defined. The combination of LOHENGRIN with an ionization chamber (or another independent means to measure the ion energy) thus provides an energy and mass identification of the separated ions.

The ionization chamber shown in Fig. 36 has some additional features. A Frisch grid is mounted in front of the anode to screen the latter from the drifting electrons (and ions) until they pass the Frisch grid. The integrated signal thus becomes independent of the distance from the anode at which the ion-electron pairs were created. The ionization chamber also has a split anode. The energy deposited in the first part of the chamber, called ΔE, and the second part, called E_r, can be read out independently. The total energy is

$$E_{tot} = \Delta E + E_r, \tag{40}$$

and will be used to determine q and A as explained above. However, the ratio $\Delta E/E_{tot}$ provides additional information. It depends on the specific energy loss of the ions in the gas, which in turn depends on the nuclear charge Z of the incoming ion according to the Bethe-Bloch equation. For a particle with speed v, energy E, traveling a distance x into a target of electron number density n and mean excitation potential I, the Bethe-Bloch equation at low energy reads[66]

$$-\frac{dE}{dx} = \frac{4\pi n Z^2}{m_e v^2}\left(\frac{e^2}{4\pi\epsilon_0}\right)^2 \ln\left(\frac{2m_e v^2}{I}\right), \tag{41}$$

where ϵ_0 is the vacuum permittivity, m_e the electron rest mass and e the electron charge.

5.2 Instrument calibrations

5.2.1 Absolute energy calibration

The reaction ^{6}Li(n,α)t produces monoenergetic tritons (2.73 MeV) and alphas (2.05 MeV), and is used for calibration of the absolute energy measured. This is done by placing the ^{6}Li in the target position and simultaneously scanning the electric and magnetic fields for the intensity peaks corresponding to the triton and alpha energies.

5.2.2 Mass calibration

New fission targets are introduced into the beam tube by a dedicated target changing mechanism that has a lateral tolerance of a few mm for the exact target position. After introducing a new target, the ion optical image of it is matched with fixed diaphragms in the focal plane by scanning the magnetic field. Thus the calibration constant of the main magnet (χ) is defined.

The magnetic field setting of the RED magnet is a fixed multiple of the magnetic field in the main magnet

$$\kappa = \frac{\rho_{main}}{\rho_{RED}} = \frac{4\text{m}}{0.6\text{m}} \approx 6.67. \tag{42}$$

5.2.3 Ionization chamber calibration

The induced ionization current in the IC is very small, typically nanoamperes, and is therefore fed through a preamplifier (Ortec 142) and a main amplifier (Ortec 571) to facilitate measurement. The amplified signals from the ΔE and E_r parts are run through an analog to digital converter (ADC) and stored on a computer with a resolution of 1024 channels each. The readouts are saved independently in list mode, as well as combined in a correlated 2D histogram of 1024 × 2048 channels (see Fig. 37 for an example). By measuring the most abundant ternary particles (^{3}H, ^{6}He, etc.) and scattered stable isotopes (^{12}C, ^{24}Mg, ^{27}Al), the energy and nuclear charge measurement of the ionization chamber is calibrated. The pressure of the counting gas is set in a range of 15 to 160 mbar for best Z identification, and to ensure full stopping of the incoming ion beam. There is additional scattering and energy loss in the IC entrance window. A thorough account for the calibration with respect to this can be found in Appendix A.3 of U. Köster 2000[7]. By calibrating the IC, reference spectra are also obtained. An application of this is seen in Fig. 37. Abundant isotopes show up as big peaks. By identifying these from a reference spectrum, the channel numbers can be associated to nuclear charges and masses. Location of less abundant particles can then be inferred. The diagonal line in the figure corresponds to $\Delta E = E_{tot}$, which are events where the fragments are completely stopped in the grid separating the ΔE part from the E_r part, i.e. never entering the latter. The parabola line corresponds to ions that scatter in the entrance window, thus traversing the IC with large angle and reduced energy.

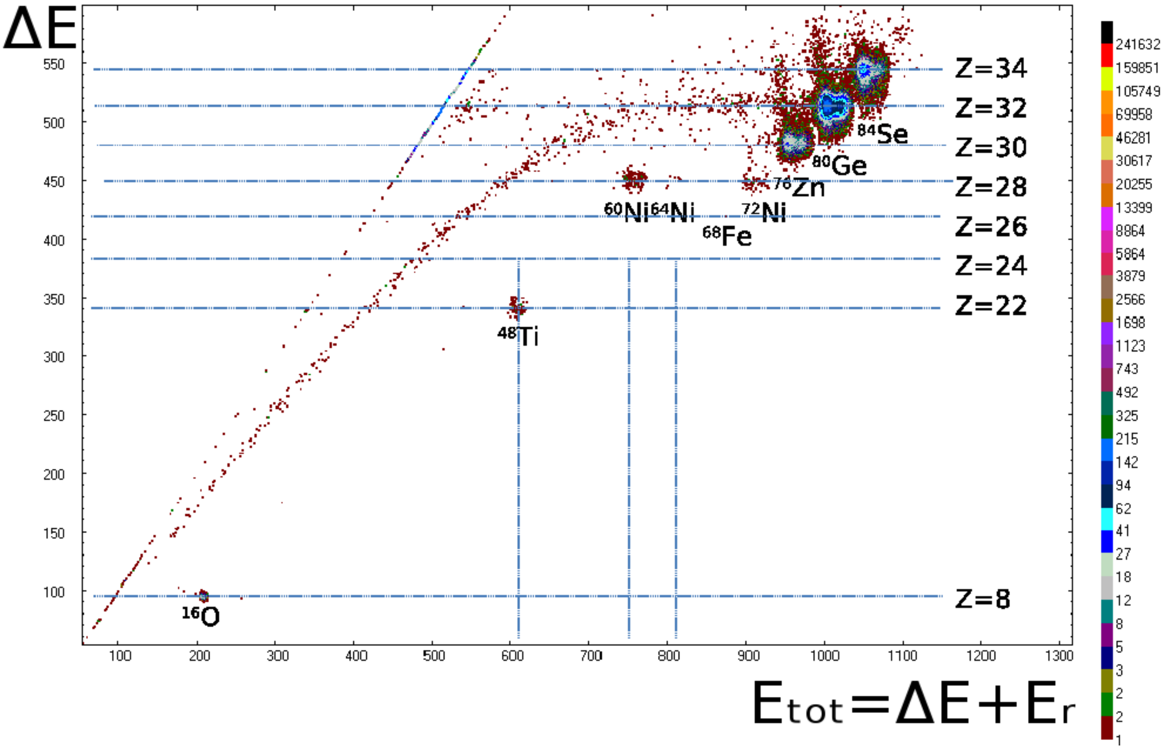

Figure 37: A typical ΔE versus E_{tot} spectrum from the IC. The color bar signify the number of counts. The data was taken with the separator settings $A/q = 4$, $E/q = 5.3$ MeV and a live time of 5.2 h.

5.2.4 Dead time

After a successfully registered event, the IC electronics cannot record another event for a certain period of time, called dead time. The measurement time (called real time) needs to be subtracted with the dead time to give the proper count rate. The result is called the live time (LT). This is automatically done in the data stored from the IC. An additional safeguard is also introduced by having a 66 Hz pulser give constant counts in the IC for measurement of the dead time.

5.3 Data analysis

The goal of the experiment at Lohengrin was to find the mass yields and average kinetic energies of fission fragments compatible with CCT, or an upper limit of the mass yield in case of a non-observation. In particular, the fragments ^{68,70}Ni and ^{34,36}Si from ^{235}U($\mathrm{n_{th}}$,f) were searched for, as these are the reported fragments in the FOBOS experiments[10]. The mass yield, denoted $M_A(Z)$, is defined as the fraction of fission fragments with nuclear charge Z and mass A produced per fission event. The steps in the data analysis consist of getting the count rates as function of kinetic energy and ionic charge, then correcting for spectrometer acceptance, nuclear burn-up of the target and energy losses. The mass and isotopic yields are determined from the integration of the ionic charge state and kinetic energy distributions. Both of the distributions generally follow a normal distribution, but due to the thick target, the energy distribution has a tail towards lower energies, which is well-desribed by a skew-normal distribution (Sec. C). To convert these relative measurements to absolute fission yields, these values have to be normalized to a reference mass with known fission yield, that is measured and analysed in the same way. For this purpose the mass yield ratio of $A = 80$ to $A = 98$ was determined. Since the fission yield of each of these masses are dominated by one isotope, namely ^{80}Ge and ^{98}Y, respectively, these measurements serve also for the determination of the ionic charge-state distribution $q = F(Z,v)$.

5.3.1 Independent isotopic yield determination

The mass yield $M_A(Z)$ of a fragment is obtained by integrating over its energy and ionic charge-state distribution,

$$M_A(Z) = \int \sum_q M_A(Z,q,E)dE. \tag{43}$$

Instead of measuring the kinetic energy distribution for each charge (as it would take too long time) the assumption is made that the two variables are independent[67,68,69]. The mass yield is then attained by measuring different q at E fixed close to the mean energy $\bar{E}$ (called a q-scan), and measuring different E at q close to the mean ionic charge $\bar{q}$ (called an E-scan). The total fragment yield is then calculated by integrating the E distribution and dividing it by the fractional q yield of q at E-mean in the q distribution, according to

$$M_A(Z) = \frac{\sum_q M_{A,\bar{E}}(Z,q)}{M_A(Z,\bar{E},\bar{q})} \int M_{A,\bar{q}}(Z,E)dE, \tag{44}$$

where $M_{A,\bar{E}}(Z,q)$ is the counts in the q-scan, $M_{A,\bar{q}}(Z,E)$ is the counts in the E-scan and $M_A(Z,\bar{E},\bar{q})$ the common data point where the data series intersect. Under the assumption of no correlation between the variables, Eq. (44) becomes exactly equal to Eq. (43). In reality the q distribution depends slightly on the kinetic energy, since more energetic ions are faster and easier stripped to higher charge states. However, absolute yield measurements are not done, but instead normalized to the known mass yield of a reference mass. The assumption is therefore that the q–E correlation for the measured mass is sufficiently similar to that of the reference mass that it cancels to first order and thus does not introduce a significant error in the integrated yield. Dedicated measurements of this effect have been performed at Lohengrin, and demonstrated that the assumption is valid and possible uncertainties introduced are on the percent level[70].

5.3.2 Mass yields of extremely rare isotopes

When measuring extremely rare masses even the simplified q scan would take too much time. The q distribution is purely given by atomic physics, meaning that it depends on the element (Z) but not a specific isotope (A). Thus measurements of the q distribution of more abundant isotopes of the element in question are representative for the rare one. The fragments of main interest are ^{68,70}Ni. Fission fragments kick out atoms from the nickel cover foil that can be separated by Lohengrin. Dedicated q scans were then done of ^{58}Ni at different energies to deduce $\bar{q}$ and σ_q as a function of velocity. These are then representative for the q distributions of ^{68,70}Ni at the same velocity.

5.3.3 Ion passage through foils

It would be cumbersome or impossible to add adequate cover foils for each element to be studied. Therefore a second, more universal approach is taken. Ionic charge-state distributions of a great variety of ions after passage through stripper foils have been measured experimentally. These data sets were used to develop semi-empiric formulae (Nikolaev-Dimitriev[60], Shima[61] [62], etc.) that describe the ionic charge-state distributions as function of Z, v and Z_{foil}. Z_{foil} is not set to $Z = 28$ for nickel, since the hot nickel foil is exposed to a finite rest gas pressure in the Lohengrin beam tube, and is therefore likely partially oxidized. Instead the q-scan of ^{58}Ni ions and those of other abundantly produced ions (^{80}Ge, ^{98}Y) are used to fit an effective Z_{foil}. Using the same formulae with the fixed Z_{foil} allows predicting the q distribution of other elements (Fe, etc.) nearby that could not be measured directly. Given that the q distributions show a slow and monotonous dependence on Z, no major error is introduced by this approximation.

5.3.4 Data corrections

The quantities that enters into the yield are corrected for nuclear burn-up, energy loss in the target/nickel foil and spectrometer acceptance. The energy loss is obtained from SRIM[20] or GEANT4[21,22] simulations of energy loss in the cover foil and (part of) the target. Due to the strong energy dispersion of the Lohengrin spectrometer, at a given separator setting only a small fraction of the kinetic energy distribution of a given mass will be transmitted through the analysis slit in the focal plane. The accepted energy range ΔE is proportional to the set energy E, hence the energy acceptance increases with energy E and has to be corrected for. This is done by simply dividing the raw count rate of ions by the set separator energy to obtain ions/(s MeV). Formally, the MeV in the denominator is later removed by integrating over E. The count rate is also corrected for the live time of the measurement, and the geometric acceptance that is proportional to the number of open shutters.

5.3.5 Nuclear burn-up and sputtering

A nuclear target will diminish over time as portions of it fissions and are sputtered. This is referred to as nuclear burn-up. Both of these effects need to be accounted for to give a proper count rate. This is achieved by doing a burn-up measurement in-between regular measurements, consisting of repeated measurements of the kinetic energy and/or ionic charge distributions for a given mass. Fig. 38 shows the result from a typical burn-up measurement. The burn-up data is fitted with two exponentially decaying functions

$$BU(t) = c_1 e^{-(\ln 2)t/t_1} + c_2 e^{-(\ln 2)t/t_2}, \tag{45}$$

a "slow" and a "fast", which empirically represents all observed target effects, namely nuclear transmutation, self-sputtering plus possible additional losses due to thermal stress (between target layer and backing when the target that is kept under vacuum heats to high temperatures). The countrate N_A at a time t corrected for target burn-up is then defined as

$$N_A = \frac{M_A(t)}{BU(t)}. \tag{46}$$

The measured burn-up data is compared to a theoretical exponential decay function $e^{-t\cdot\sigma\cdot\phi}$, where t is the time that the target has been in the reactor, σ is the neutron capture cross section and ϕ the neutron flux. The difference between the theoretical and measured burn-up is mainly due to the sputtering.

On a side note, this method is valid if the charge state and kinetic energy distributions stay the same throughout the experiment. In reality, they drift slightly with time. A shift from the reference q and E would then show up as a decrease/increase in intensity. To avoid this, a full burn-up scan over energy and/or charge states are done, and the separator settings are monitored by scanning the RED and main magnets. The drift is less than a 10^{-3} effect.

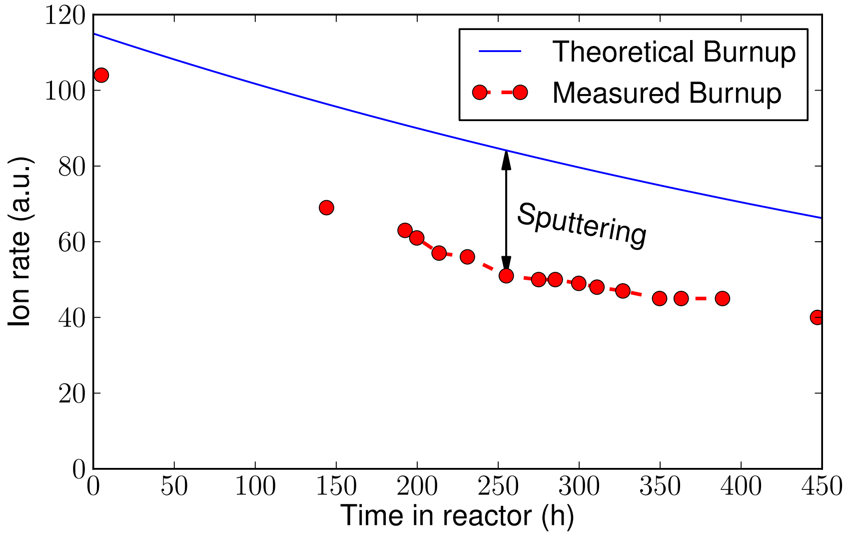

Figure 38: Theoretical burn-up (solid line) and measured burn-up including sputtering (circles) of the target.

5.4 Results

This section establishes experimental upper limits of CCT yields, by direct measurement with the fission fragment spectrometer LOHENGRIN, at the Institut Laue-Langevin. Results are presented for ^{68,70}Ni and ^{34,36}Si in ^{235}U(n$_{\text{th}}$,f). To validate the count-rate to yield conversion, the mass-yield ratio of the well-known reference masses $A = 80$ to $A = 98$ were measured and reproduced. The count rates of all other measured fission products were normalized to these reference masses. As a verification of the capability to measure extremely rare fission processes, the isotopic yield of binary ^{70}Ni in ^{235}U(n$_{\text{th}}$,f) was measured and reproduced. In addition, a new estimate of the upper limit of the ^{68}Ni yield in binary fission was established.

5.4.1 Verifying yields of reference masses

In ^{235}U(n$_{\text{th}}$,f), the tabulated yields of masses $A = 80$ and $A = 98$ are $Y(^{80}\text{X}) = 0.00129$ and $Y(^{98}\text{X}) = 0.0575$ fragments/fission, respectively[71]. This gives the mass yield ratio $Y(^{80}\text{X})/Y(^{98}\text{X}) \approx 0.0224$. The experimentally measured ratio in this work was

$$\frac{M_{80}}{M_{98}} = 0.0234(9). \tag{47}$$

5.4.2 Verifying the isotopic yield of ^{70}Ni in far asymmetric fission

Sida et al.[18] measured the mass yield of binary fragments with $A = 70$ in ^{235}U(n$_{\text{th}}$,f) to be 10^{-7} fragments/fission for even elements, with a mean kinetic energy of $\bar{E} = 96(2)$ MeV. The databases JEFF[71] and ENDF-349[72] tabulates a mass yield of $3.3 \cdot 10^{-8}$ for $A = 70$, and an isotopic yield of $2.5 \cdot 10^{-8}$ for ^{70}Ni. The current experiment measured the isotopic yield to be

$$Y_{\text{binary}}(^{70}\text{Ni}) = 2.8(7) \cdot 10^{-8} \quad \text{fragments/fission}, \tag{48}$$

and the mean kinetic energy was found to be $\bar{E} = 89(1)$ MeV (see the fit in Fig. 40). Note that the current experiment was optimized for higher acceptance, rather than energy resolution.

5.4.3 Isotopic yield of ^{68,70}Ni and ^{34,36}Si in CCT

Figures 39, 40 and 41 show the number of fission fragments/fission event/MeV as a function of kinetic energy for ^{68}Ni, ^{70}Ni and ^{34,36}Si, respectively. Each point is in general composed of several measurement series at different ionic charge states. Circles with arrows signify upper limits, while squares with error bars signify data points in the IC spectra. The bars in energy correspond to the intentionally widened acceptance of LOHENGRIN, rather than an uncertainty. Note that the plots have a logarithmic ordinate, which means that a Gaussian kinetic energy distribution will show up as a parabola. The yield is attained by integrating such a distribution over energy. Since no indication of CCT was found, the current spectra impose strict upper limits. To obtain the upper limit, a distribution must be fitted and integrated. In both binary and ternary fission, the kinetic energy distribution of fission fragments are Gaussian distributed. The theory section (Sec. 4) derived which kinetic energies CCT fragments are allowed to have according to energy and momentum conservation. This gives no prediction of the width or the mean of the kinetic energy distribution. As of such, the yield has to be presented as a function of these unknown parameters, which is done in Fig. 42 for ^{34,36}Si and ^{68,70}Ni. The global upper limit of the yield is given by the Gaussian with the largest area, which lie nowhere above the upper limits. The upper limits for the isotopic yields were found to be

$$Y(^{68}\mathrm{Ni}) < 4.2 \cdot 10^{-9} \quad \text{fragments/fission} \tag{49}$$
$$Y_{\mathrm{CCT}}(^{70}\mathrm{Ni}) < 1.3 \cdot 10^{-8} \quad \text{fragments/fission} \tag{50}$$
$$Y(^{34,36}\mathrm{Si}) < 3.2 \cdot 10^{-8} \quad \text{fragments/fission.} \tag{51}$$

^{36}Si was only measured for a small energy range. With the same conditions as that for ^{34}Si, the measurements of the two isotopes were found to have the same statistical significance, since no events were found. The same upper limit of ^{36}Si is then assumed at other energies. If the proposed CCT is akin to ternary fission, it is expected that ^{36}Si is orders of magnitude less abundant than ^{34}Si.

The lowest energy data point in Figs. 39 and 40 has lower statistical significance. At such low energies, the edge of the radius of integration of the sought fission fragments overlaps with the "parabola" of other fragments scattered in the IC window (Fig. 37 on page 47). All overlapping events were selected. An ongoing background analysis indicates that none of the selected events are expected to be anything else than scattered fragments.

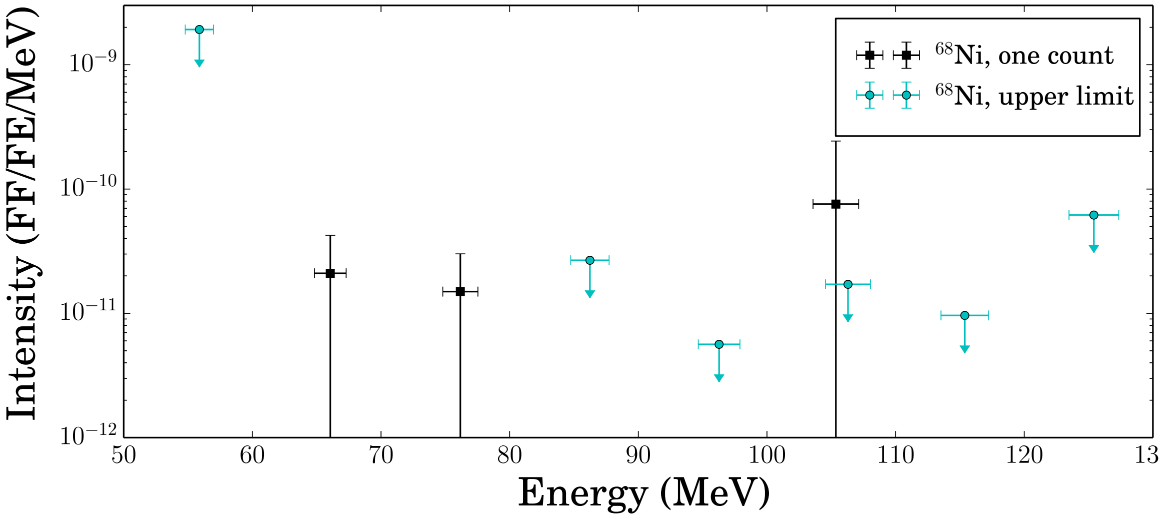

Figure 39: Measured intensity of ^{68}Ni in ^{235}U(n_{th},f) at different energies. The intensity is given as number of fission fragments/fission event/MeV. Each point is composed of several measurement series at different ionic charge states. Circles with arrows signify upper limits, while squares with error bars signify a total of one count. Note that the bars in energy correspond to the intentionally widened acceptance of LOHENGRIN, rather than an uncertainty. See the text for a comment about the point at the lowest energy.

5.4.4 New estimation of ^{68}Ni in binary fission

With the current experimental results, it is possible to derive a new estimate of the yield of ^{68}Ni in binary fission. Assuming a similar kinetic energy distribution as the one measured for ^{70}Ni, the upper limit is roughly

$$Y_{\mathrm{binary}}(^{68}\mathrm{Ni}) < 5 \cdot 10^{-10} \quad \text{fragments/fission.} \tag{52}$$

This follows the trend seen in the results of Sida et al.[18].

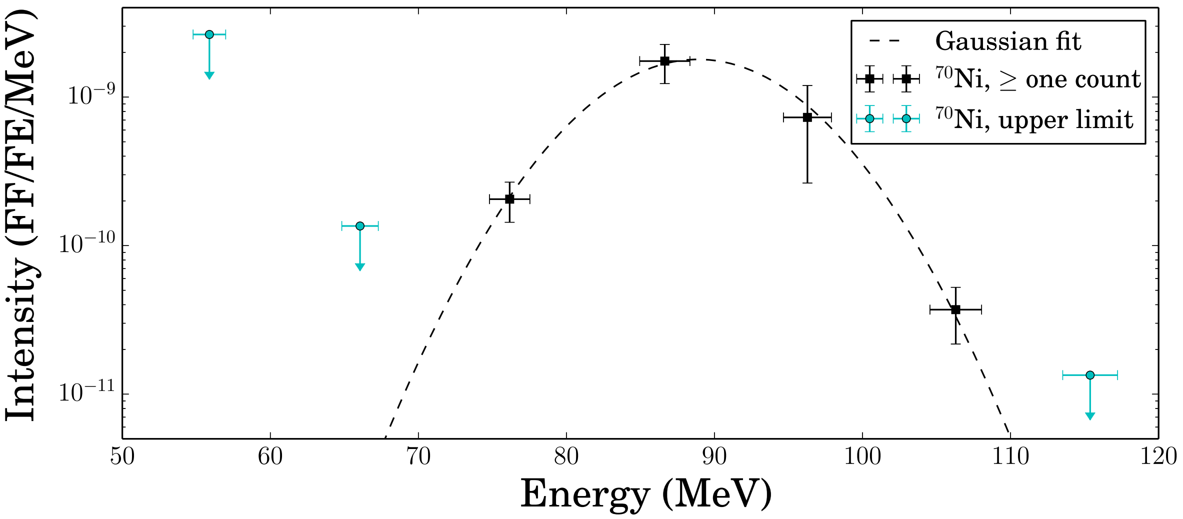

Figure 40: Measured intensity of ^{70}Ni in ^{235}U(n_{th},f) at different energies. The intensity is given as number of fission fragments/fission event/MeV. The Gaussian fit corresponds to far asymmetric fission, and the yield is attained by integrating the distribution. Each point is composed of several measurement series at different ionic charge states. Circles with arrows signify upper limits, while squares with error bars signify data points in the IC spectra. Note that the bars in energy correspond to the intentionally widened acceptance of Lohengrin, rather than an uncertainty. See the text for a comment about the point at the lowest energy.

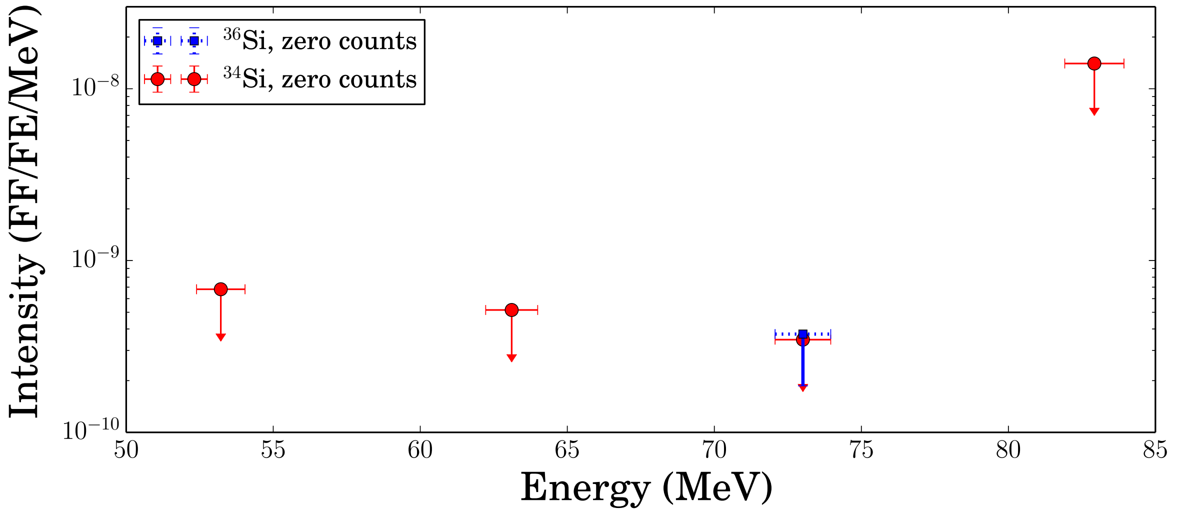

Figure 41: Measured intensity of ^{34,36}Si in ^{235}U(n_{th},f) at different energies. The intensity is given as number of fission fragments/fission event/MeV. All measurements are upper limits. The data point at the highest energy was measured further from the optimum ionic charge state, giving a lower statistical significance. Note that the bars in energy correspond to the intentionally widened acceptance of Lohengrin, rather than an uncertainty.

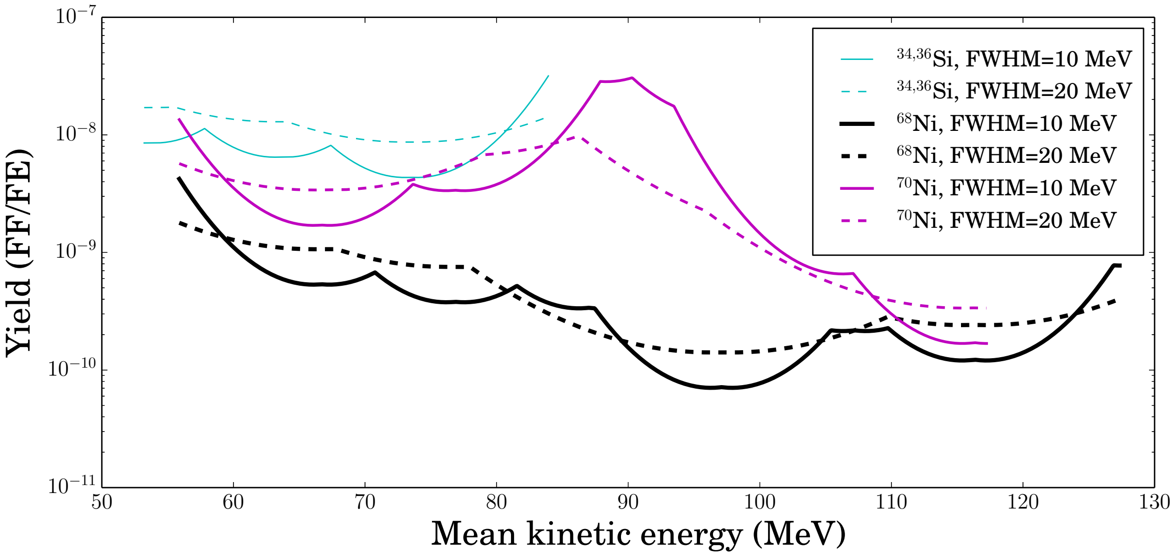

Figure 42: Upper limit of the yield, as a function of the location of the kinetic energy distribution and its FWHM. The location of the distribution is varied between the experimentally measured energies. The fission fragments are ^{34,36}Si and ^{68,70}Ni in ^{235}U(n$_{\text{th}}$,f). The local maxima arise when the distribution is "squeezed" to the highest possible amplitude between the data points of Figs. 39 to 41. The local minima generally arise when the mean of the energy distribution is the same as one of the data points. A distribution with smaller FWHM can squeeze higher between data points, but a wider distribution has a bigger area for roughly equal amplitudes. Note that the ^{68,70}Ni results at lower energies are gross over estimations, since they consist of background scatter (see full text).

5.5 Discussion

The experiments were designed to favour energy acceptance and high intensities rather than absolute energy resolution, by having a high geometric acceptance and thick targets, producing energy distributions with tails towards lower energies. This makes it easier to find potential CCT fragments, even at non-optimal energies. Still, the measurements of reference masses and far asymmetric fission yields show that the current experiments are fairly accurate as well. The results of the Lohengrin experiments and the existence of CCT will now be discussed, and a brief analysis of possible explanations for the FOBOS results will be presented.

5.5.1 Coverage of kinetic energies

The theory section (Sec. 4) derived the possible kinetic energies of CCT fragments, for different decay modes (simultaneous and sequential decay). This was done considering energy and momentum conservation, with varying mass distributions, neutron multiplicities, excitation energies and scission configurations. In case CCT is a simultaneous decay, the allowed kinetic energies of nickel are fully covered by the current experiments (compare Figs. 39 and 40 with Fig. 26 on page 35). In case CCT arises from two sequential and collinear binary fissions, either the silicon or the nickel can be born in the middle between the three fragments. As argued in the discussion (Sec. 4.6.1) and in other literature[14,48,54], it is more likely that the silicon is born in the middle. In this case, the allowed kinetic energies of nickel are fully covered (compare Figs. 39 and 40 with Fig. 22 on page 33). If silicon is born on the outside, most of the allowed kinetic energies of silicon are covered (compare Fig. 41 with Fig. 23 on page 33). If both the silicon and nickel were born on the outside (with the tin in the middle), the silicon and nickel kinetic energies could be slightly increased. Since the writing of this thesis, however, new experiments have been carried out at Lohengrin. The new experiments cover different kinetic energies over a wider range, in nickel up to 150 MeV, and in silicon between 30–100 MeV. So far, the analysis of these experiments shows no indication of CCT.

It is not expected that a narrow peak in the yield distribution is located between measurements. This is first of all due to the fact that the FWHM of the kinetic energy distribution of fission fragments is on the order of 10–20 MeV[36] (see Fig. 40). In addition, the energy dispersion of Lohengrin and the target increases the acceptance by roughly ±2 MeV. This means that a measurement at a kinetic energy of 100 MeV is sensitive to energies in the range 98–102 MeV. Most importantly however, the overall effect of the thick target is that it increases the FWHM by adding a low-energy tail to the energy distribution.

5.5.2 The existence of CCT

In the allowed phase space of CCT, the current experiments show no indication of events, other than that of far asymmetric fission. In this phase space, the upper limit of the yield of CCT was found to be on the order of 10^{-9} fission fragments per fission event. It is in principle possible for the kinetic energy distribution of ^{70}Ni from CCT to overlap with that from far asymmetric fission. This seems rather unlikely however, given that two completely different decays should have different kinematics. Even if the full peak would correspond to CCT rather than binary fission, it would still exclude FOBOS indirect measurement by more than 5 orders of magnitude.

Calculations[14] of Q-values and shell structure show that ^{68,70}Ni are the most energetically favourable CCT fragments. If CCT existed, a considerable excess of events around these masses would be expected. As the theoretical section shows, however (Sec. 4.6.2), even the most favourable CCT configurations are highly improbable, as they, for example, require fission of intermediate fragments which have never been observed to fission. The situation is similar in both ^{235}U(n$_{\mathrm{th}}$,f) and in ^{252}Cf(sf). The inability to connect the FOBOS result of ^{235}U(n$_{\mathrm{th}}$,f) to CCT, and the fact that the signature is identical in ^{252}Cf(sf) (which in itself is questionable given how different these decays are), points towards a systematic error.

In conclusion, the reported yield of 0.5% of FOBOS is excluded by 5–6 orders of magnitude by the Lohengrin experiment. In light of the experimental and theoretical results, it is therefore highly unlikely for CCT to occur in low-energy fission of the actinides.

5.5.3 Interpretation of the FOBOS result

It is relevant to question what the origin of the signature in the FOBOS experiments is, as it does not seem to be compatible with CCT. As alluded to in the discussion of the FOBOS setup (Sec. 3.3), it might be caused by events with missing energy or anomalous time-of-flight, which are then misinterpreted as missing-mass events. Missing energy could be due to scattering, for example in the target backing, the BIC window, the nickel mesh supporting the BIC window, the heavy concentric carrier (which noticably reduces the transparency of the setup), or in the start/stop detectors. Diffusion of target atoms into the backing will also give a different energy signature. Diffusion will also affect the time-of-flight of fragments, as does straggling in any of the elements of the setup. The peak interpreted as CCT was attained by subtracting two similar energy distributions. If one of the distributions is slightly wider, or has a low-energy tail (as the arm with the backing has), the result will always give rise to a new peak. The difference in distributions does not need to be large for the illusory peak to appear, and it can appear quite far from the mean of the two other distributions. Geant4 [21,22] simulations were performed (Sec. E) of binary fission in the FOBOS setup, to see how the energy profile differs with the addition of the target backing, and if there is an illusory peak when the signals are subtracted. The additional peak is indeed observed in the subtracted spectra from the simulations. The FOBOS experiments selected only events with similar momenta however, in order to reduce scattering effects. Without knowing how narrow the region of accepted events was, there is no way of knowing if this is the cause of the FOBOS signature.

SRIM [20] calculations were performed (Sec. D), to study the angular scattering of both the light fragment (nickel) and the ternary particle (silicon) in the target backing. The FOBOS signature was interpreted as events in which the ternary particle was scattered and implanted in the BIC support structure, missing the detector, while the light fragment was detected. The SRIM calculations show that if this signature was indeed CCT, then there should have been an identical signature for the reverse case, in which the light fragment misses the detector and the ternary particle is detected.

All the simulations assume perfect conditions. In reality, there is always some degree of impurities and problems in the experimental setup. For example, portions of the flight path with partially reduced transparency would give a missing-energy signature, as only a certain percentage of fragments passes through the portion.

Since the FOBOS experiments are based on simultaneous $v - v$ and $v - E$ identification, another possible explanation are events in which the energy but not the velocity significantly differs. This could occur in high-energy collision recoils, in which a binary fragment scatters and possibly knocks out another atom from the experimental setup, for example aluminum or oxygen from the target backing. The possibilities are many, and the simulations and analysis of the FOBOS results are ongoing.

6 Summary and conclusions

Once every few hundred fission events, three charged fragments are formed in a process known as ternary fission, as opposed to just two charged fragments in binary fission. Dedicated experiments since the 1940s shows that the third fragment, called the ternary particle, in the great majority of all cases is very light; 90% ^{4}He, 9% heavier helium or hydrogen, and 1% a particle with $Z > 2$. Experiments also show that the ternary particle is emitted at roughly 90° towards the fission axis[33], and that the yield is rapidly decreasing with increased Z and A[6]. For sizes comparable to the other two fragments, only upper limits of the yield existed prior to 2010, of roughly 10^{-10}[8,9].

In 2010 a paper[10] was published claiming the detection of Collinear Cluster Tri-partition, which is fission in which three heavy fragments are emitted perfectly collinear along the same fission axis. The paper reported ternary ^{48}Ca yields of $(4.7 \pm 0.2) \times 10^{-3}$ and ternary ^{34}Si yields of $(5.1 \pm 0.4) \times 10^{-3}$, in ^{252}Cf(sf) and ^{235}U(n$_{\mathrm{th}}$,f), respectively. This claim was based on non-detection of the ternary particles, measuring binary coincidences from the respective fissioning systems with the same detector setup, called FOBOS, at the Joint Institute for Nuclear Research in Dubna, Russia. A thin fission target had been deposited on a 50 μg/cm^{2} thick Al_2O_3 backing, placed between two detector units. The fragment velocities and energies were measured with the TOF-E method. The backing was positioned such that it created an asymmetry by blocking the flight path towards one of the detectors. The fragment masses were reconstructed from the measured velocities and energies, and compared in a mass-versus-mass spectrum, as well as a mass-difference spectrum. A peak lying far below the mass sum of the fissioning system was apparent in these spectra, which was interpreted as a missing particle. The explanation offered is that these events correspond to three fragments being emitted perfectly collinear, with two being in the same direction, and one of them being scattered by the target backing and implanted in the detector support structure, missing detection.

Any remarkable new discovery requires a verification with an independent experimental setup. Such a verification, or refutation, is possible with the LOHENGRIN fission fragment recoil separator, located at the high-flux neutron reactor of Institut Laue-Langevin in Grenoble, France. LOHENGRIN is a single-arm spectrometer that covers a small solid angle of a fission target, and separates the fission fragments according to their mass over ionic charge ratio and kinetic energy, with a combination of magnetic and electric fields[16,17]. The instrument is currently the most sensitive spectrometer for the measurement of neutron-induced fission products, enabling accurate studies of fission yields down to 10^{-10}[18,19] fragments per fission.

LOHENGRIN detects only one fragment per fission event, due to its small solid angle acceptance. Perfectly collinear fragments are separated from each other by magnetic and electric fields, since they do not simultaneously satisfy the given A/q and E/q separator conditions. The spectrometer is therefore not used to measure coincidence events. On the other hand, if at a given yield level no events are detected at LOHENGRIN, it provides a stringent upper limit on the production of these fragments in whatever fission configuration. Hence, a non-observation at LOHENGRIN allows refuting experimental claims of CCT.

The result of the LOHENGRIN experiments is a new upper limit for the yield of fragments compatible with CCT in ^{235}U(n$_{\mathrm{th}}$,f), on the order of 10^{-9}. This excludes the previously claimed yield by FOBOS by more than 5 orders of magnitude. The experiments also verify the far asymmetric fission yields of ^{70}Ni, and presents a new estimate of the production of

^{68}Ni in binary fission, as an upper limit of $5 \cdot 10^{-10}$.

Extended theoretical calculations and simulations demonstrate that the experiments cover a sufficient and representative range of kinetic energies of potential CCT fragments. The calculations also highlight several contradictions in the CCT hypothesis. The CCT interpretation of the FOBOS data is excluded as a likely origin since it assumes fission of low fissility nuclei, and because it is based on energetically unfavourable reactions under implausible conditions. It is further shown that if these conditions would somehow be alleviated, CCT would very easily have been detected by several experiments before.

Theoretical studies[14] of Q-values and shell structure support the idea that if something like CCT exists, it should populate most strongly ^{68}Ni and ^{70}Ni. Since no events are found with these fragments, or any neighbouring masses or isotopes, it is safe to say that CCT, in light of the current as well as previous studies, is a highly improbable event in all low-energy fission.

7 Outlook

This work demonstrates the power of a very sensitive instrument and of simple and comprehensible models, to verify, and refute new claims. Moreover it shows that binary fission yields on the 10^{-9} level can still be reliably measured at LOHENGRIN, i.e. the apparent local maximum that was observed at mass $A = 70$ in the far asymmetric binary fission of various actinides could be explored further to study the existence of an additional fission mode centered at this value.

True ternary fission could be further explored, in particular if the kinetic energy distribution of exotic ternary fragments is sufficiently well predicted by calculations so that a partial measurement of the kinetic energy distribution is sufficient to estimate the fission yields.

The results presented will enable more accurate ternary fission models with greater predictive power, by excluding CCT as a probable decay mode, leading to a greater understanding of the ternary fission process.

Glossary

(n_{th},f) Thermal neutron-induced fission.

(sf) Spontaneous fission.

a.u. Arbitrary unit.

amu Unified atomic mass unit, approximately the mass of one nucleon.

Binary Fission The most common kind of nuclear fission, in which two charged fragments are formed, possibly accompanied by neutron emission and gamma radiation.

Burn-up Loss and alteration of fission target atoms.

CCT Collinear Cluster Tri-partition, an alleged special kind of fission in which three charged fragments of similar mass are emitted perfectly collinear along the same fission axis.

Exo-energetic A reaction that is net exo-energetic releases energy, as opposed to requiring it (endo-energetic).

FOBOS Fission fragment spectrometer, positioned at the Flerov Laboratory of Nuclear Reactions of the Joint Institute for Nuclear Research in Dubna, Russia.

FS Fissioning System.

FWHM Full Width at Half Maximum of a distribution.

HF Heavy Fragment, the heavy main fission fragment.

ILL Institut Laue-Langevin, international research center focused on neutron science and technology, based in Grenoble, France.

IM Intermediate Fragment, a fission fragment which itself undergoes fission.

Ionic Charge Number of protons subtracted by the number of non-stripped electrons in an atom or ion.

LCP Light Charged Particle accompanied fission, a more correct name for ternary fission.

LDM Liquid Drop Model[5], macroscopic model which treats the nucleus as a charged liquid drop. Successful at describing gross features of the nucleus, like binding energies and Q-values. It fails at describing shell effects and super-heavy nuclei.

LF Light Fragment, the light main fission fragment.

LOHENGRIN A fission fragment recoil separator located at ILL. LOHENGRIN is currently the worlds most sensitive spectrometer for studying neutron-induced fission fragments, and also acts as a radioactive ion beam facility for nuclear spectroscopy of exotic neutron-rich nuclei.

LRA Long Range Alphas, another name for ternary alpha particles. This name was introduced since ternary alphas are more energetic than those from radioactive alpha decay, leading to longer tracks in detectors.

Pre-Scission Kinetic Energy The kinetic energy the fragments have at scission.

Q-value Amount of energy released in a reaction.

RED Reverse Energy Dispersion magnet, instrument in the LOHENGRIN setup that refocuses the beam of fission fragments.

SCM Shell-Correction Method, a model developed by V.M. Strutinsky[26], which combines the Liquid Drop Model with the nuclear shell model.

Ternary Fission A mode of fission in which three charged fragments are formed, possibly accompanied by neutron emission and gamma radiation. Two of the fragments are usually similar to the light and heavy fragments of binary fission, while the third usually is a lighter fragment like ^{4}He.

Ternary Particle Ternary fission is often viewed as a modified version of binary fission, with an additional particle called the ternary particle. The ternary particle is typically much lighter than the other fission fragments.

Tip Distance The center-to-center distance subtracted by the radii of two particles.

TKE Total kinetic plus Coulomb potential energy.

TOF-E Time-of-flight versus energy, a particle detection method which allows the individual measurement of velocity and energy of one or several fragments. The velocity is inferred from a time-of-flight measurement from a start and a stop signal over a known flight distance.

TP Ternary Particle, the lightest of the fragments in ternary fission.

True Ternary Fission Fission in which three fragments of comparable size are emitted, also known as "real" ternary fission.

TXE Total excitation energy.

Yield The fraction of a fission product produced per fission.

Acknowledgements

First and foremost, I wish to express my gratitude towards my supervisor Ulli Köster at Institut Laue-Langevin for making this project possible. The project was well designed and has provided me with invaluable experiences and several merits which will help me significantly in my future career. Working with Ulli was really fun, which owes to his positive spirit and warm personality.

A big thanks goes to everyone in the subatomic physics group at Chalmers for making me feel welcome, for the pointers on my thesis, and for all the help in general. In particular, thanks to Andreas Heinz for his excellent supervision, without which I would not have come as far as I have, Håkan Johansson for his great expertise with technical details, and Thomas Nilsson for sharing his wealth of knowledge.

I have benefited from fruitful discussions with Herbert Faust, Michael Jentschel and Olivier Serot, for which I am grateful. Thanks to the staff at ILL and all the friends I made in Grenoble for making my summer in the French Alps an amazing experience.

Thank you Saladin Grebovic for the proofreading and for your constructive feedback.

I wish to thank the developers of the free softwares I have used. I am especially thankful to the developers of NumPy, SciPy, SymPy, Matplotlib, OpenCL and PyOpenCL.

Last but not least, thanks to all my friends and to my family. You made my years at Chalmers truly wonderful.

A CCT Kinematics in ^{252}Cf(sf)

This section uses the theory and simulations of Sec. 4, and applies it to the spontaneous fission of ^{252}Cf. The results show a very good agreement with Vijayaraghavan et al.[14]

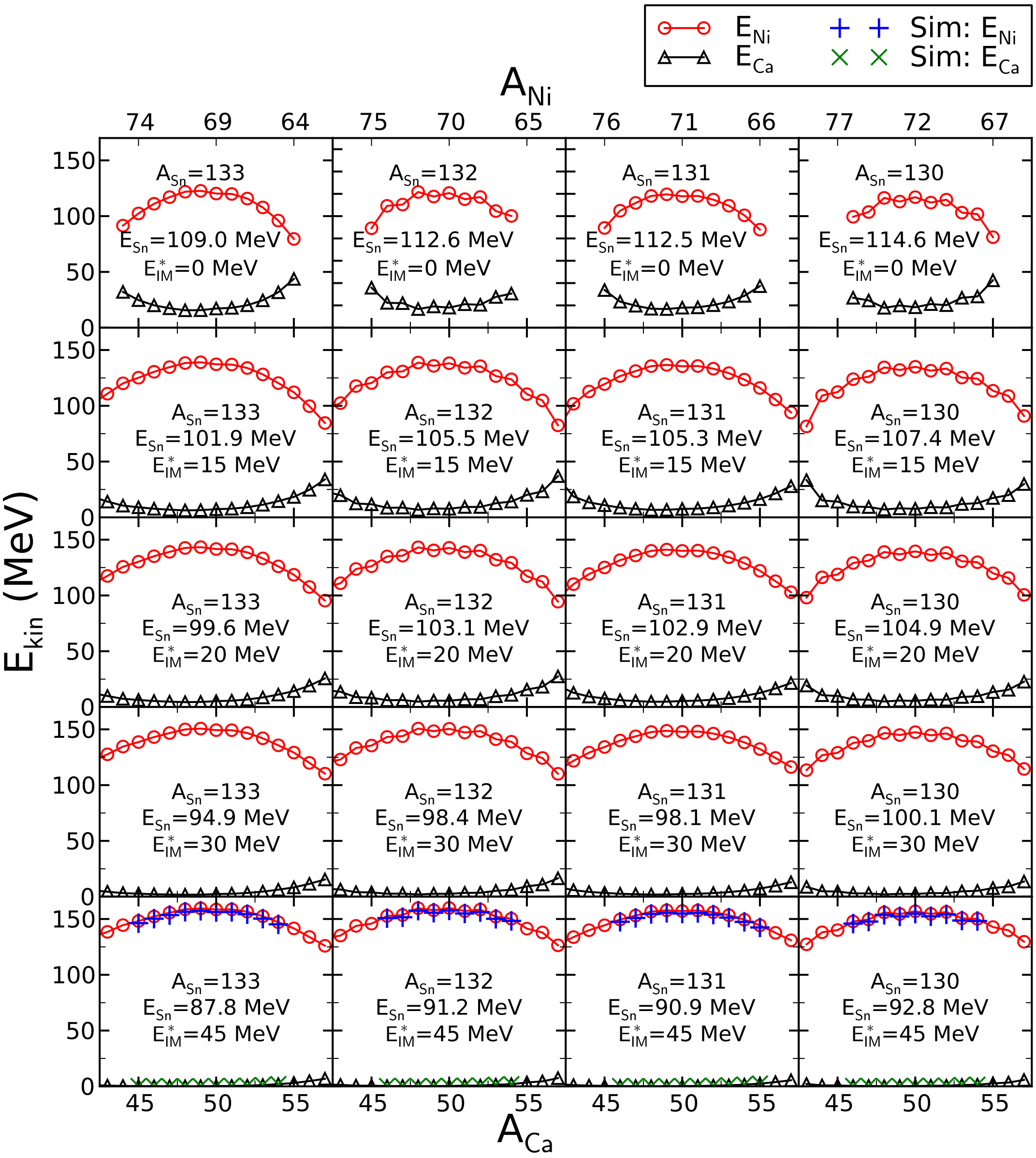

Figure 43: Kinetic energy of nickel (born on the outside) and calcium (born in the middle) versus their mass split, in the sequential CCT $^{252}\mathrm{Cf(sf)} \to {}^{A_{\mathrm{Sn}}}\mathrm{Sn} + {}^{A_{\mathrm{Cd}}}\mathrm{Cd} \to {}^{A_{\mathrm{Sn}}}\mathrm{Sn} + {}^{A_{\mathrm{Ni}}}\mathrm{Ni} + {}^{A_{\mathrm{Ca}}}\mathrm{Ca}$. The mass split between the HF and IM is varied in each plot going horizontally, and the IM excitation energy $E^*_{\mathrm{IM}} = \mathrm{TXE}$ vertically. The energies are calculated analytically (◯,△) and with Monte Carlo trajectory simulations (+,×). Simulations only show results that are energetically allowed and have a tip distance at the second scission of ≤ 7 fm.

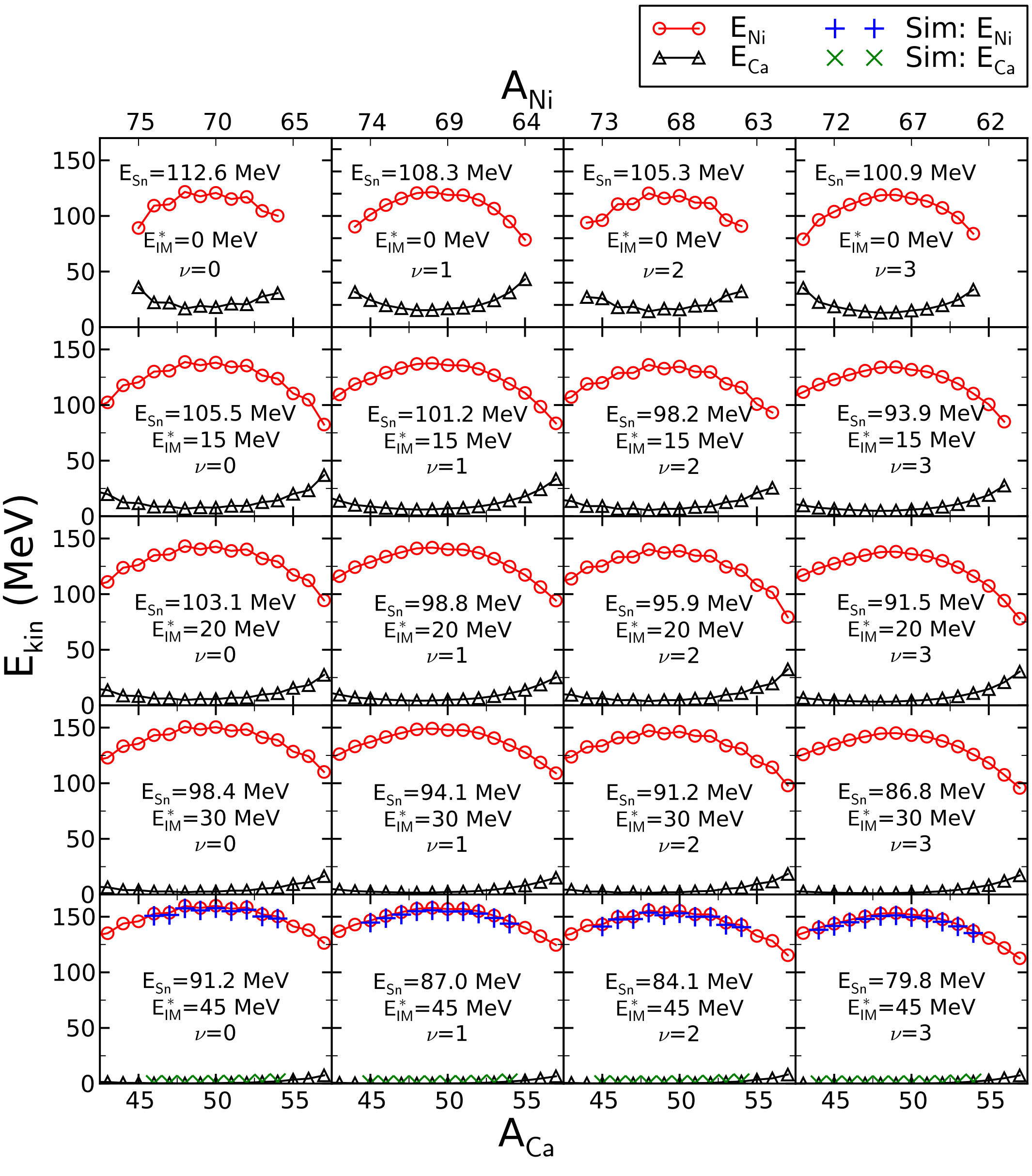

Figure 44: Kinetic energy of nickel (born on the outside) and calcium (born in the middle) versus their mass split, in the sequential CCT $^{252}\text{Cf(sf)} \rightarrow {}^{132}\text{Sn} + {}^{A_{Cd}}\text{Cd} + \nu \rightarrow {}^{A_{132}}\text{Sn} + {}^{A_{Ni}}\text{Ni} + {}^{A_{Si}}\text{Si} + \nu$. The prompt neutron multiplicity ν is varied in each plot going horizontally, and the IM excitation energy $E^*_{\mathrm{IM}} = \mathrm{TXE}$ vertically. The energies are calculated analytically (◯,△) and with Monte Carlo trajectory simulations (+,×). Simulations only show results that are energetically allowed and have a tip distance at the second scission of ≤ 7 fm.

B Tip distance and energy conservation

This section shows the relationship between tip distance and energy conservation. See Fig. 28 in Sec. 4.6.2 for application. The tip distance between two fragments, labeled 1 and 2, is defined as

$$r_{td} = r_{12} - R_1 - R_2, \tag{53}$$

where $R_i = r_0 A_i^{1/3}$ are the fragment sharp radii with $r_0 \approx 1.25$ fm, and r_{12} is the center-to-center distance. Typical tip distances at scission are close to ~ 2.5 fm, while tip distances over $3-4$ fm are generally not considered as physically possible[51]. The required excitation energy for physically valid configurations can be derived by considering the energy balance in the rest frame of the IM

$$Q_2 + E^*_{\mathrm{IM}} = k\frac{e^2 Z_{TP} Z_{LF}}{r_{td} + r_{TP} + r_{LF}}, \tag{54}$$

where r_{TP} and r_{LF} are the TP and LF radii, r_{td} is the tip distance, k is the Coulomb constant and e the elementary charge. Take for example the CCT in $^{235}\mathrm{U}(\mathrm{n_{th}},\mathrm{f}) \rightarrow {}^{\mathrm{A_{Sn}}}\mathrm{Sn} + {}^{\mathrm{A_{Mo}}}\mathrm{Mo} + \nu \rightarrow {}^{\mathrm{A_{Sn}}}\mathrm{Sn} + {}^{\mathrm{A_{Ni}}}\mathrm{Ni} + {}^{\mathrm{A_{Si}}}\mathrm{Si} + \nu$. In most of the fissioning systems ${}^{\mathrm{A_{Mo}}}\mathrm{Mo} \rightarrow {}^{\mathrm{A_{Ni}}}\mathrm{Ni} + {}^{\mathrm{A_{Si}}}\mathrm{Si}$, Q_2 is negative with values down to -20 MeV (see Fig. 18 in Sec. 4.5.1). By plotting $Q_2 + E^*_{\mathrm{IM}}$ versus the tip distance (Fig. 28 in Sec. 4.6.2), it is seen that a very high excitation energy is required for physically reasonable tip distances at the second scission, but that it is hard to obtain that much excitation energy without making the first scission configuration unphysically large.

C Area and uncertainty of the Normal and Skew Normal distributions

The skew normal distribution (SN) is a generalisation of the Normal distribution (N), allowing for non-zero skewness (α). In this work, it is used for fitting and integrating the data in the energy distribution scan for fission fragments going through the fission target. The additional skewness parameter α stayed constant within a small uncertainty for all data series, justifying the usage of the skew normal distribution. The normal distribution was used to fit the q distribution of said fission fragments. This section defines the probability density function (pdf) and cumulative distribution function (cdf) of the normal and skew normal distribution. The mean, standard deviation and area are also defined, and the uncertainty of these quantities is derived. To this end, the propagation of uncertainty is used. For a function $f(x_1, x_2, ..., x_n)$, where each of the individual variables x_1 to x_n has uncertainties σ_{x_1} to σ_{x_n} respectively, and covariances $\mathrm{cov}_{x_1x_2}$ etc., the uncertainty in f is attained as

$$\sigma_f = \sqrt{\sum_{i=1}^{n} \sigma_{x_i}^2 \left(\frac{\partial f}{\partial x_i}\right)^2 + 2\sum_{i\neq j} \left(\frac{\partial f}{\partial x_i}\right)\left(\frac{\partial f}{\partial x_j}\right) \mathrm{cov}_{x_ix_j}}. \tag{55}$$

The following relations between a pdf f and a cdf F will be used

$$\left.\begin{array}{l} \int_{-\infty}^{\infty} f(t)dt = 1 \\ \int_{-\infty}^{x} f(t)dt = F(x) \end{array}\right\} \Rightarrow \begin{aligned} \int_0^{\infty} f(t)dt &= \int_{-\infty}^{\infty} f(t)dt - \int_{-\infty}^{0} f(t)dt = \\ &= 1 - F(0). \end{aligned} \tag{56}$$

Definitions

The standard normal distribution has the probability density function

$$\phi(x) = \frac{1}{\sqrt{2\pi}} e^{\frac{-x^2}{2}} \tag{57}$$

and the cumulative distribution function

$$\Phi(x) = \int_{-\infty}^{x} \phi(t)dt = \frac{1}{2}\left[1 + \mathrm{Erf}(\frac{x}{\sqrt{2}})\right], \tag{58}$$

where Erf is the error function. The skew normal distribution with location μ, scale σ and skewness α has the pdf

$$f(x,\mu,\sigma,\alpha) = \frac{2}{\sigma}\phi\left(\frac{x-\mu}{\sigma}\right)\Phi\left(\alpha\frac{x-\mu}{\sigma}\right), \tag{59}$$

and the cdf

$$F(x,\mu,\sigma,\alpha) = \Phi\left(\frac{x-\mu}{\sigma}\right) - 2T\left(\frac{x-\mu}{\sigma},\alpha\right), \tag{60}$$

where $T(h,a)$ is Owen's T function[73], defined as

$$T(h,a) = \frac{1}{2\pi}\int_0^a \frac{e^{-\frac{1}{2}h^2(1+x^2)}}{1+x^2}dx, \quad (-\infty < h,a < \infty). \tag{61}$$

In this work, a slightly differently scaled skew normal distribution was used in order to allow for obtaining start values for fit parameters, defined as

$$\tilde{f}(x,A,\mu,\sigma,\alpha) = \frac{A}{2} e^{-(x-\mu)^2/2\sigma^2} \left[1 + \mathrm{Erf}\left(\alpha \frac{x-\mu}{\sigma\sqrt{2}}\right)\right] = A\sigma\sqrt{\frac{\pi}{2}} f(x), \tag{62}$$

where A is an amplitude fit parameter.

Area of the Normal Distribution

For a normal distribution, the mean is simply the location μ, and the standard deviation the scale σ. This is not true for a skew normal distribution. Let $\tilde{N}$ denote a differently scaled normal distribution

$$\tilde{N}(x,A,\mu,\sigma) = Ae^{\frac{-(x-\mu)^2}{2\sigma^2}} = A\sigma\sqrt{2\pi}N(x,\mu,\sigma) \tag{63}$$

where $N = \frac{1}{\sigma\sqrt{2\pi}} e^{\frac{-(x-\mu)^2}{2\sigma^2}}$ is the regular normal distribution (pdf). Using Eq. (56), the area of the scaled normal distribution becomes

$$\begin{aligned} a_{\tilde{N}} &= A\sigma\sqrt{2\pi}\int_0^\infty N(x,\mu,\sigma)dx = A\sigma\sqrt{2\pi}\left[1 - \Phi\left(-\frac{\mu}{\sigma}\right)\right] \\ &= A\sigma\sqrt{\frac{\pi}{2}}\left[1 + \mathrm{Erf}\left(\frac{\mu}{\sigma\sqrt{2}}\right)\right] \end{aligned} \tag{64}$$

Let σ_A, σ_μ and σ_σ be the uncertainties of the amplitude, mean and standard deviation respectively. The square of the uncertainty of the area is then

$$\begin{aligned} \sigma^2_{a,\tilde{N}} &= \sigma_A^2 \frac{\sigma^2}{2}\left[1 + \mathrm{Erf}\left(\frac{\mu}{\sigma\sqrt{2}}\right)\right]^2 + \\ &\quad \sigma_\mu^2 A^2 e^{\frac{-\mu^2}{\sigma^2}} + \\ &\quad \sigma_\sigma^2 A^2 \left[\frac{\mu}{\sigma} e^{\frac{-\mu^2}{2\sigma^2}} - \sqrt{\frac{\pi}{2}}\left(1 + \mathrm{Erf}\left(\frac{\mu}{\sigma\sqrt{2}}\right)\right)\right]^2 + \\ &\quad \mathrm{cov}_{A\mu} A\sigma\sqrt{2\pi} e^{\frac{-\mu^2}{2\sigma^2}} \left[1 + \mathrm{Erf}\left(\frac{\mu}{\sigma\sqrt{2}}\right)\right] + \\ &\quad \mathrm{cov}_{A\sigma} A\sigma\sqrt{2\pi}\left[1 + \mathrm{Erf}\left(\frac{\mu}{\sigma\sqrt{2}}\right)\right]\left[\sqrt{\frac{\pi}{2}}\left(1 + \mathrm{Erf}\left(\frac{\mu}{\sigma\sqrt{2}}\right)\right) - \right. \\ &\qquad\qquad\qquad\qquad\qquad\qquad \left. \frac{\mu}{\sigma} e^{\frac{-\mu^2}{2\sigma^2}}\right] + \\ &\quad \mathrm{cov}_{\mu\sigma} 2A^2 e^{\frac{-\mu^2}{2\sigma^2}} \left[\sqrt{\frac{\pi}{2}}\left(1 + \mathrm{Erf}\left(\frac{\mu}{\sigma\sqrt{2}}\right)\right) - \frac{\mu}{\sigma} e^{\frac{-\mu^2}{2\sigma^2}}\right] \end{aligned} \tag{65}$$

Mean of the Skew Normal Distribution

The mean of the skew normal distribution is defined as

$$\langle f \rangle_{SN} = \mu + \sigma\frac{\alpha}{\sqrt{1+\alpha^2}}\sqrt{\frac{2}{\pi}}. \tag{66}$$

One can easily see that the mean becomes identical to that of the normal distribution when $\alpha = 0$. Using the uncertainty propagation in Eq. (55), the square of the uncertainty of the mean is

$$\begin{aligned} \sigma^2_{\langle f\rangle,SN} &= \sigma^2_\mu + \sigma^2_\sigma \frac{2\alpha^2}{\pi(1+\alpha^2)} + \sigma^2_\alpha \frac{2\sigma^2}{(1+\alpha^2)^3} + \\ & \mathrm{cov}_{\mu\sigma} \frac{2\alpha}{1+\alpha^2}\sqrt{\frac{2}{\pi}} + \\ & \mathrm{cov}_{\mu\alpha} \frac{2\sigma}{\sqrt{(1+\alpha^2)^3}}\sqrt{\frac{2}{\pi}} + \\ & \mathrm{cov}_{\sigma\alpha} \frac{4\alpha\sigma}{\pi(1+\alpha^2)^2}. \end{aligned} \tag{67}$$

Standard Deviation of the Skew Normal Distribution

The standard deviation of the skew normal distribution is defined as

$$\sigma_{f,SN} = \sigma\sqrt{1 - \frac{2}{\pi}\frac{\alpha^2}{1+\alpha^2}}. \tag{68}$$

The square of the uncertainty of the standard deviation then is

$$\begin{aligned} \sigma^2_{\sigma_f,SN} &= \sigma^2_\sigma \frac{\pi + \alpha^2(\pi-2)}{\pi(1+\alpha^2)^2} + \\ & \sigma^2_\alpha \frac{4\alpha^2\sigma^2}{\pi(1+\alpha^2)^3(\pi+\alpha^2(\pi-2))} - \\ & \mathrm{cov}_{\sigma\alpha} \frac{4\alpha\sigma}{\pi(1+\alpha^2)^2}. \end{aligned} \tag{69}$$

Area of the Skew Normal Distribution

Let a denote the area of the skew normal distribution

$$a_{SN} = \int_0^\infty \tilde{f}(E,A,\mu,\sigma,\alpha)dE = A\sigma\sqrt{\frac{\pi}{2}}\int_0^\infty f(E,A,\mu,\sigma,\alpha)dE. \tag{70}$$

Using Eq. (56), Eq. (70) becomes

$$\begin{aligned} a_{SN} &= A\sigma\sqrt{\frac{\pi}{2}}\Big(1 - F(0,\mu,\sigma,\alpha)\Big) = \\ &= A\sigma\sqrt{2\pi}\left[1 + \mathrm{Erf}\left(\frac{\mu}{\sigma\sqrt{2}}\right) + 4T\left(\frac{\mu}{\sigma},\alpha\right)\right]. \end{aligned} \tag{71}$$

Using the uncertainty propagation in Eq. (55), the square of the uncertainty of the area becomes

$$
\begin{aligned}
\sigma_{a,SN}^2 \quad = \quad & \sigma_A^2 \frac{\sigma^2 \pi}{8} \left[1 + \mathrm{Erf}\left(\frac{\mu}{\sigma\sqrt{2}} \right) + 4T\left(\frac{\mu}{\sigma}, \alpha \right) \right]^2 + \\
& \sigma_\mu^2 \frac{A^2}{4} e^{\frac{-\mu^2}{\sigma^2}} \mathrm{Erfc}\left(\frac{\alpha\mu}{\sigma\sqrt{2}} \right)^2 + \\
& \sigma_\sigma^2 \frac{A^2}{16\sigma^2} e^{\frac{-\mu^2}{\sigma^2}} \left[2\mu \mathrm{Erfc}\left(\frac{\alpha\mu}{\sigma\sqrt{2}} \right) + \right. \\
& \qquad\qquad \left. e^{\frac{-\mu^2}{2\sigma^2}} \left(1 + \mathrm{Erf}\left(\frac{\mu}{\sigma\sqrt{2}} \right) + 4T\left(\frac{\mu}{\sigma}, \alpha \right) \right)^2 \right]^2 + \\
& \sigma_\alpha^2 \frac{A^2 \sigma^2}{\pi (1+\alpha^2)^2} e^{\frac{-\mu^2 (1+\alpha^2)}{\sigma^2}} + \\
& \mathrm{cov}_{A\mu} \frac{A\sigma}{2} \sqrt{\frac{\pi}{2}} e^{\frac{-\mu^2}{2\sigma^2}} \mathrm{Erfc}\left(\frac{\alpha\mu}{\sigma\sqrt{2}} \right) \left[1 + \mathrm{Erf}\left(\frac{\mu}{\sigma\sqrt{2}} \right) + 4T\left(\frac{\mu}{\sigma}, \alpha \right) \right] + \\
& \mathrm{cov}_{A\sigma} \frac{A}{4} \left[1 + \mathrm{Erf}\left(\frac{\mu}{\sigma\sqrt{2}} \right) + 4T\left(\frac{\mu}{\sigma}, \alpha \right) \right] \times \\
& \qquad \left[\sigma\pi \left(1 + \mathrm{Erf}\left(\frac{\mu}{\sigma\sqrt{2}} \right) + 4T\left(\frac{\mu}{\sigma}, \alpha \right) \right) - \right. \\
& \qquad \left. \mu\sqrt{2\pi} e^{\frac{-\mu^2}{2\sigma^2}} \mathrm{Erfc}\left(\frac{\alpha\mu}{\sigma\sqrt{2}} \right) \right] + \\
& \mathrm{cov}_{A\alpha} \frac{A\sigma^2}{2(1+\alpha^2)} e^{\frac{-\mu^2(1+\alpha^2)}{2\sigma^2}} \left[1 + \mathrm{Erf}\left(\frac{\mu}{\sigma\sqrt{2}} \right) + 4T\left(\frac{\mu}{\sigma}, \alpha \right) \right] + \\
& \mathrm{cov}_{\mu\sigma} \frac{A^2}{2\sigma} e^{\frac{-\mu^2}{\sigma^2}} \left[\sigma \sqrt{\frac{\pi}{2}} e^{\frac{\mu^2}{2\sigma^2}} \left(1 + \mathrm{Erf}\left(\frac{\mu}{\sigma\sqrt{2}} \right) + 4T\left(\frac{\mu}{\sigma}, \alpha \right) \right) - \right. \\
& \qquad\qquad \left. \mu \mathrm{Erfc}\left(\frac{\alpha\mu}{\sigma\sqrt{2}} \right) \right] \mathrm{Erfc}\left(\frac{\alpha\mu}{\sigma\sqrt{2}} \right) + \\
& \mathrm{cov}_{\mu\alpha} \frac{A^2 \sigma}{\sqrt{2\pi}(1+\alpha^2)} e^{\frac{-\mu^2(2+\alpha^2)}{2\sigma^2}} \mathrm{Erfc}\left(\frac{\alpha\mu}{\sigma\sqrt{2}} \right) + \\
& \mathrm{cov}_{\sigma\alpha} \frac{A^2}{2(1+\alpha^2)} e^{\frac{-\mu^2(2+\alpha^2)}{2\sigma^2}} \left[\sigma e^{\frac{\mu^2}{2\sigma^2}} \left(1 + \mathrm{Erf}\left(\frac{\mu}{\sigma\sqrt{2}} \right) + 4T\left(\frac{\mu}{\sigma}, \alpha \right) \right) - \right. \\
& \qquad\qquad \left. \mu \sqrt{\frac{2}{\pi}} \mathrm{Erfc}\left(\frac{\alpha\mu}{\sigma\sqrt{2}} \right) \right] . \qquad (72)
\end{aligned}
$$

D SRIM calculations

This section presents SRIM[20] calculations of the geometric distribution of fission fragments in the FOBOS experiment (Sec. 3). The purpose of the calculations is to show that the target backing spreads fragments over an area much larger than the millimeter nickel mesh holes. Figure 45 shows results for ^{34}Si at 10 and 70 MeV, and Fig. 46 for ^{68}Ni and ^{102}Mo at 100 MeV.

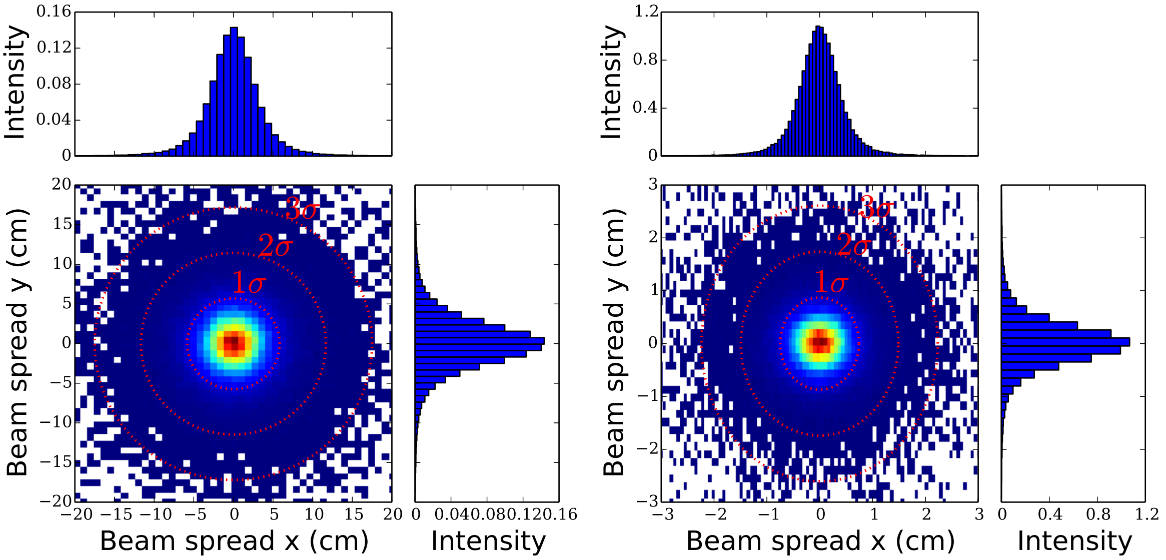

Figure 45: The figure shows the geometric distribution of ^{34}Si at 10 MeV (left) and 70 MeV (right), 50 cm after passing through a 50 μg/cm^2 thick Al_2O_3 target backing.

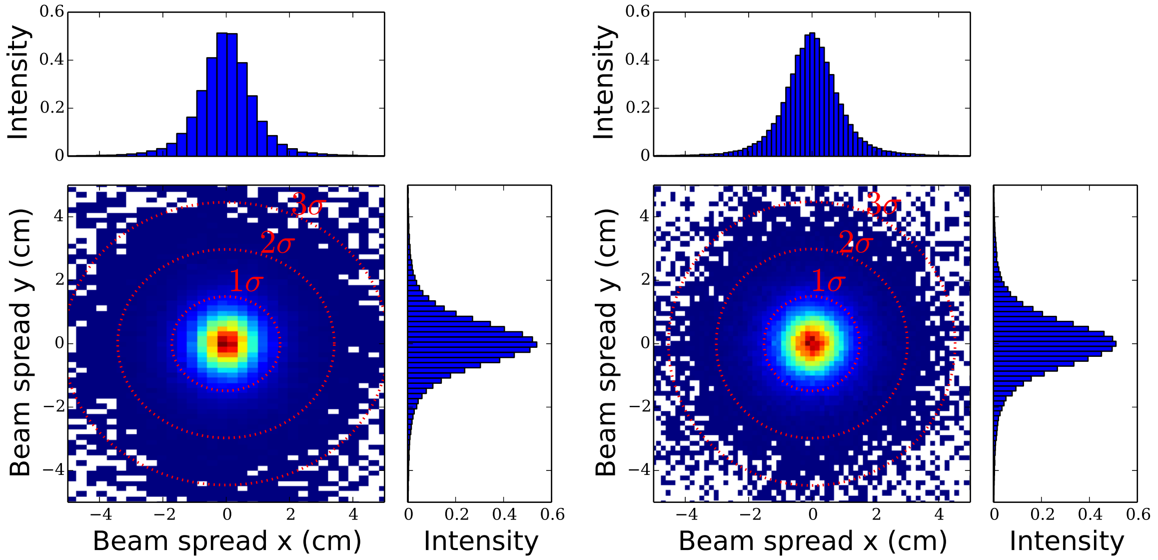

Figure 46: The figure shows the geometric distribution of a 100 MeV beam of ^{68}Ni (left) and ^{102}Mo (right), 50 cm after passing through a 50 μg/cm^2 thick Al_2O_3 target backing.

E Geant4 calculations

This section presents Geant4[21,22] simulations of binary fission fragments in the FOBOS experimental setup (Sec. 3). The purpose of the calculations is to show how the subtraction of two binary signals can give the illusion of a missing-energy event. The fragment used in the simulations is ^{102}Mo from the process

$$\mathrm{n_{th}} + {}^{235}_{92}\mathrm{U} \quad\longrightarrow\quad {}^{132}_{50}\mathrm{Sn} + {}^{102}_{42}\mathrm{Mo} + 2\mathrm{n}. \tag{73}$$

Simulations with two different setups were performed, with 10^6 events in each simulation. In both cases, a source ejecting ^{102}Mo was placed $\sim$ 50 cm from a detector covered by a nickel mesh, with a diameter of 40 cm. The nickel mesh had a thickness of 1 mm and was covered with 2.7×2.7 mm^2 size holes, separated by 0.9 mm. In one of the setups, an additional 50 μg/cm^2 thick Al_2O_3 piece was placed just next to the source, covering the flight path towards the detectors. The angle of the emitted particles were set to cover the entire detector. ^{102}Mo was ejected with kinetic energies following a Gaussian distribution with a FWHM of 10 MeV. The mean kinetic energy was set to be 113 MeV, which was derived from energy and momentum conservation of the process in Eq. (73). Fig. 47 shows the spectra of the detector in both simulations, and the difference of the spectra. As can be seen, the difference gives rise to a peak at lower energies.

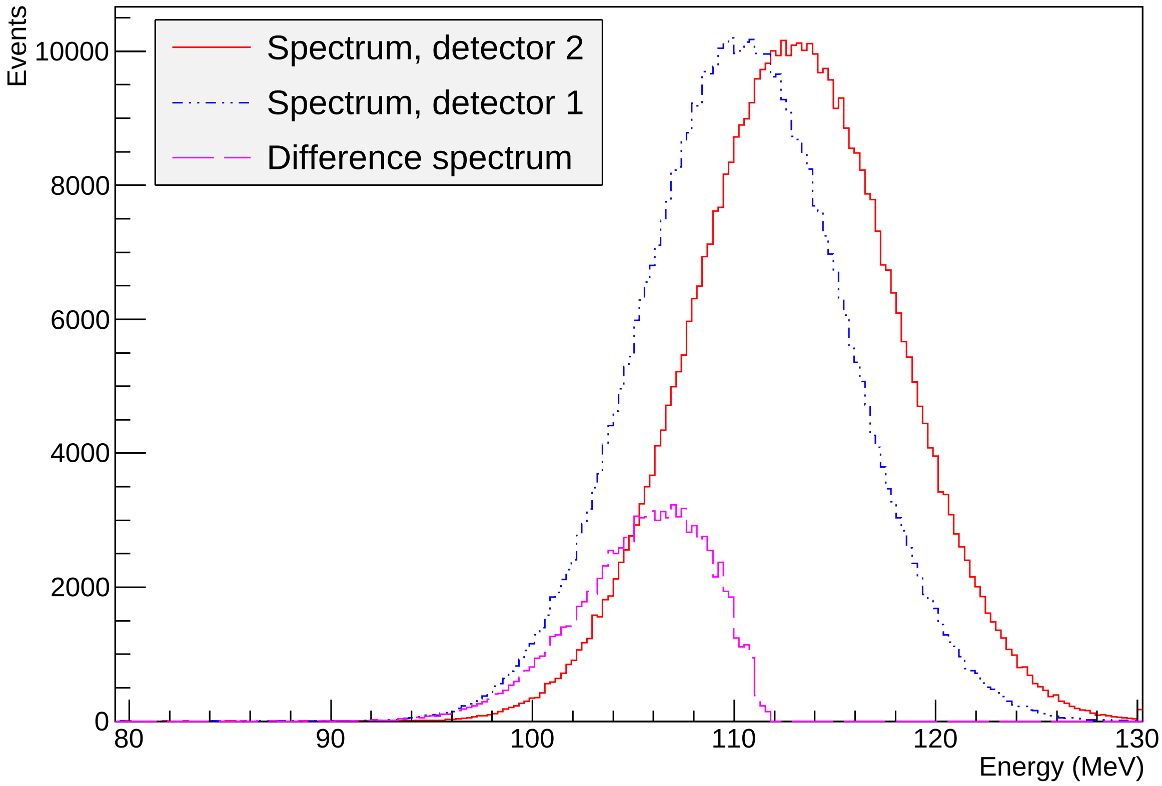

Figure 47: Spectra from Geant4 simulations of binary ^{102}Mo in the FOBOS detectors. Detector 1 and 2 corresponds to the directions with and without the target backing, respectively.

References

[1] Richard Shurtleff and Edward Derringh. The most tightly bound nucleus. *American Journal of Physics*, 57(6):552–552, 1989. doi: http://dx.doi.org/10.1119/1.15970. URL `http://scitation.aip.org/content/aapt/journal/ajp/57/6/10.1119/1.15970`.

[2] M. P. Fewell. The atomic nuclide with the highest mean binding energy. *American Journal of Physics*, 63(7):653–658, 1995. doi: http://dx.doi.org/10.1119/1.17828. URL `http://scitation.aip.org/content/aapt/journal/ajp/63/7/10.1119/1.17828`.

[3] O. Hahn and F. Strassmann. Über den nachweis und das verhalten der bei der bestrahlung des urans mittels neutronen entstehenden erdalkalimetalle. *Naturwissenschaften*, 27(1):11–15, 1939. ISSN 0028-1042. doi: 10.1007/BF01488241. URL `http://dx.doi.org/10.1007/BF01488241`.

[4] Otto Hahn and Fritz Strassmann. Nachweis der entstehung aktiver bariumisotope aus uran und thorium durch neutronenbestrahlung; nachweis weiterer aktiver bruchstücke bei der uranspaltung. *Naturwissenschaften*, 27(6):89–95, 1939. ISSN 0028-1042. doi: 10.1007/BF01488988. URL `http://dx.doi.org/10.1007/BF01488988`.

[5] L. Meitner and O.R. Frisch. Disintegration of uranium by neutrons: a new type of nuclear reaction. *Nature*, 143:239–240, February 1939. doi: 10.1038/143239a0.

[6] F. Gönnenwein. Ternary and quaternary fission. *Nuclear Physics A*, 734(0):213 – 216, 2004. ISSN 0375-9474. doi: http://dx.doi.org/10.1016/j.nuclphysa.2004.01.037. URL `http://www.sciencedirect.com/science/article/pii/S0375947404000429`. Proceedings of the Eighth International Conference On Nucleus-Nucleus Collisions.

[7] U. Köster. *Yields and spectroscopy of radioactive isotopes at LOHENGRIN and ISOLDE.* PhD thesis, TU München, Geneva, 2000.

[8] R. W. Stoenner and Manny Hillman. Search for Radiochemical Evidence for Ternary Fission of ^{235}U by Thermal Neutrons. *Phys. Rev.*, 142:716–719, Feb 1966. doi: 10.1103/PhysRev.142.716. URL `http://link.aps.org/doi/10.1103/PhysRev.142.716`.

[9] P. Schall, P. Heeg, M. Mutterer, and J.P. Theobald. On symmetric tripartition in the spontaneous fission of ^{252}Cf. *Physics Letters B*, 191(4):339 – 342, 1987. ISSN 0370-2693. doi: http://dx.doi.org/10.1016/0370-2693(87)90619-8. URL `http://www.sciencedirect.com/science/article/pii/0370269387906198`.

[10] Yu.V. Pyatkov, D.V. Kamanin, W. von Oertzen, A.A. Alexandrov, I.A. Alexandrova, O.V. Falomkina, N.A. Kondratjev, Yu.N. Kopatch, E.A. Kuznetsova, Yu.E. Lavrova, A.N. Tyukavkin, W. Trzaska, and V.E. Zhuhcko. Collinear cluster tri-partition of ^{252}Cf(sf) and in the ^{235}U(n_{th},f) reaction. *The European Physical Journal A*, 45(1):29–37, 2010. ISSN 1434-6001. doi: 10.1140/epja/i2010-10988-8. URL `http://dx.doi.org/10.1140/epja/i2010-10988-8`.

[11] H.-G. Ortlepp, W. Wagner, C.-M. Herbach, A.A. Aleksandrov, I.A. Aleksandrova, M. Andrassy, A. Budzanowski, B. Czech, M. Danziger, L. Dietterle, V.N. Doronin, S. Dshemuchadse, A.S. Fomichev, W.D. Fromm, M. Gebhardt, P. Gippner, K. Heidel, Sh. Heinitz, H. Homeyer, S.A. Ivanovsky, D.V. Kamanin, I.V. Kolesov, A. Matthies, D. May, S.I. Merzlyakov, W. von Oertzen, Yu.Ts. Oganessian, G. Pausch, Yu.E. Penionzhkevich, Yu.V. Pyatkov, S.V. Radnev, G. Renz, L.A. Rubinskaya, I.D. Sandrev, K.D. Schilling, W. Seidel, D.I. Shishkin, A.P. Sirotin, H. Sodan, O.V. Strekalovsky, V.G. Tishchenko, V.V. Trofimov, I.P. Tsurin, C. Umlauf, D.V. Vakatov, V.M. Vasko, V.A. Vitenko, E. Will, M. Wilpert, R. Yanez, V.E. Zhuchko, P. Ziem, and L. Zrodlowski. The 4π-fragment-spectrometer FOBOS. *Nuclear Instruments and Methods in Physics Research Section A: Accelerators, Spectrometers, Detectors and Associated Equipment*, 403(1):65 – 97, 1998. ISSN 0168-9002. doi: http://dx.doi.org/10.1016/S0168-9002(97)00777-8. URL `http://www.sciencedirect.com/science/article/pii/S0168900297007778`.

[12] V. Pashkevich, Yu.V. Pyatkov, and A Unzhakova. Collinear cluster tripartition in fission of actinide nuclei. *International Journal of Modern Physics E*, 19(04):718–724, 2010. doi: 10.1142/S0218301310015151. URL `http://www.worldscientific.com/doi/abs/10.1142/S0218301310015151`.

[13] K. Manimaran and M. Balasubramaniam. All possible ternary fragmentations of ^{252}Cf in collinear configuration. *Phys. Rev. C*, 83:034609, Mar 2011. doi: 10.1103/PhysRevC.83.034609. URL `http://link.aps.org/doi/10.1103/PhysRevC.83.034609`.

[14] K.R. Vijayaraghavan, W. Oertzen, and M. Balasubramaniam. Kinetic energies of cluster fragments in ternary fission of ^{252}Cf. *The European Physical Journal A*, 48(3):1–8, 2012. ISSN 1434-6001. doi: 10.1140/epja/i2012-12027-4. URL `http://dx.doi.org/10.1140/epja/i2012-12027-4`.

[15] Yu. V. Pyatkov, D. V. Kamanin, W. von Oertzen, A. A. Alexandrov, V. E. Zhuchko, O. V. Strekalovsky, N. A. Kondtatyev, E. A. Kuznetsova, and I. A. Alexandrova. *Collinear cluster tripartition: first steps in physical treating*, chapter 35, pages 253–260. 2013. doi: 10.1142/9789814508865_0035. URL `http://www.worldscientific.com/doi/abs/10.1142/9789814508865_0035`.

[16] P. Armbruster, M. Asghar, J.P. Bocquet, R. Decker, H. Ewald, J. Greif, E. Moll, B. Pfeiffer, H. Schrader, F. Schussler, G. Siegert, and H. Wollnik. The recoil separator lohengrin: Performance and special features for experiments. *Nuclear Instruments and Methods*, 139(0):213 – 222, 1976. ISSN 0029-554X. doi: http://dx.doi.org/10.1016/0029-554X(76)90677-7. URL `http://www.sciencedirect.com/science/article/pii/0029554X76906777`.

[17] E. Moll, H. Schrader, G. Siegert, H. Hammers, M. Asghar, J. Boguet, P. Armbruster, H. Ewald, and H. Wollnik. Aufbau und Arbeitsweise Spaltprodukt-Massenseparators LOHENGRIN am Hochflussreaktor in Grenoble. *Kerntechnik*, 19:374 – 381, 1977.

[18] J.L. Sida, P. Armbruster, M. Bernas, J.P. Bocquet, R. Brissot, and H.R. Faust. Mass, charge, and energy distributions in very asymmetric thermal fission of ^{235}U. *Nuclear Physics A*, 502(0): 233 – 242, 1989. ISSN 0375-9474. doi: http://dx.doi.org/10.1016/0375-9474(89)90664-7. URL `http://www.sciencedirect.com/science/article/pii/0375947489906647`.

[19] U. Köster, H. Faust, G. Fioni, T. Friedrichs, M. Groß, and S. Oberstedt. Ternary fission yields of ^{241}Pu(n$_{\mathrm{th}}$,f). *Nuclear Physics A*, 652(4):371 – 387, 1999. ISSN 0375-9474. doi: http://dx.doi.org/10.1016/S0375-9474(99)00115-3. URL `http://www.sciencedirect.com/science/article/pii/S0375947499001153`.

[20] J. F. Ziegler, M. D. Ziegler, and J. P. Biersack. Srim - the stopping and range of ions in matter (2010). *Nuclear Instruments and Methods in Physics Research B*, 268:1818–1823, June 2010. doi: 10.1016/j.nimb.2010.02.091.

[21] S. Agostinelli, J. Allison, K. Amako, J. Apostolakis, H. Araujo, P. Arce, M. Asai, D. Axen, S. Banerjee, G. Barrand, F. Behner, L. Bellagamba, J. Boudreau, L. Broglia, A. Brunengo, H. Burkhardt, S. Chauvie, J. Chuma, R. Chytracek, G. Cooperman, G. Cosmo, P. Degtyarenko, A. Dell'Acqua, G. Depaola, D. Dietrich, R. Enami, A. Feliciello, C. Ferguson, H. Fesefeldt, G. Folger, F. Foppiano, A. Forti, S. Garelli, S. Giani, R. Giannitrapani, D. Gibin, J.J. Gómez Cadenas, I. González, G. Gracia Abril, G. Greeniaus, W. Greiner, V. Grichine, A. Grossheim, S. Guatelli, P. Gumplinger, R. Hamatsu, K. Hashimoto, H. Hasui, A. Heikkinen, A. Howard, V. Ivanchenko, A. Johnson, F.W. Jones, J. Kallenbach, N. Kanaya, M. Kawabata, Y. Kawabata, M. Kawaguti, S. Kelner, P. Kent, A. Kimura, T. Kodama, R. Kokoulin, M. Kossov, H. Kurashige, E. Lamanna, T. Lampén, V. Lara, V. Lefebure, F. Lei, M. Liendl, W. Lockman, F. Longo, S. Magni, M. Maire, E. Medernach, K. Minamimoto, P. Mora de Freitas, Y. Morita, K. Murakami, M. Nagamatu, R. Nartallo, P. Nieminen, T. Nishimura, K. Ohtsubo, M. Okamura, S. O'Neale, Y. Oohata, K. Paech, J. Perl, A. Pfeiffer, M.G. Pia, F. Ranjard, A. Rybin, S. Sadilov, E. Di Salvo, G. Santin, T. Sasaki, N. Savvas, Y. Sawada, S. Scherer, S. Sei, V. Sirotenko, D. Smith, N. Starkov, H. Stoecker, J. Sulkimo, M. Takahata, S. Tanaka, E. Tcherniaev, E. Safai Tehrani, M. Tropeano, P. Truscott, H. Uno, L. Urban, P. Urban, M. Verderi, A. Walkden, W. Wander, H. Weber, J.P. Wellisch, T. Wenaus, D.C. Williams, D. Wright, T. Yamada, H. Yoshida, and D. Zschiesche. Geant4 - a simulation toolkit. *Nuclear Instruments and Methods in Physics Research Section A: Accelerators, Spectrometers, Detectors and Associated Equipment*, 506(3):250 – 303, 2003. ISSN 0168-9002. doi: http://dx.doi.org/10.1016/S0168-9002(03)01368-8. URL `http://www.sciencedirect.com/science/article/pii/S0168900203013688`.

[22] J. Allison, K. Amako, J. Apostolakis, H. Araujo, P.A. Dubois, M. Asai, G. Barrand, R. Capra, S. Chauvie, R. Chytracek, G. A P Cirrone, G. Cooperman, G. Cosmo, G. Cuttone, G. G. Daquino, M. Donszelmann, M. Dressel, G. Folger, F. Foppiano, J. Generowicz, V. Grichine, S. Guatelli, P. Gumplinger, A. Heikkinen, I. Hrivnacova, A. Howard, S. Incerti, V. Ivanchenko, T. Johnson, F. Jones, T. Koi, R. Kokoulin, M. Kossov, H. Kurashige, V. Lara, S. Larsson, F. Lei, O. Link, F. Longo, M. Maire, A. Mantero, B. Mascialino, I. McLaren, P.M. Lorenzo, K. Minamimoto, K. Murakami, P. Nieminen, L. Pandola, S. Parlati, L. Peralta, J. Perl, A. Pfeiffer, M.G. Pia, A. Ribon, P. Rodrigues, G. Russo, S. Sadilov, G. Santin, T. Sasaki, D. Smith, N. Starkov, S. Tanaka, E. Tcherniaev, B. Tome, A. Trindade, P. Truscott, L. Urban, M. Verderi, A. Walkden, J. P. Wellisch, D.C. Williams, D. Wright, and H. Yoshida. Geant4 developments and applications. *Nuclear Science, IEEE Transactions on*, 53(1):270–278, Feb 2006. ISSN 0018-9499. doi: 10.1109/TNS.2006.869826.

[23] N. Bohr and J.A. Wheeler. The mechanism of nuclear fission. *Phys. Rev.*, 56:426–450, Sep 1939. doi: 10.1103/PhysRev.56.426. URL `http://link.aps.org/doi/10.1103/PhysRev.56.426`.

[24] O. Haxel, J. Hans D. Jensen, and Hans E. Suess. On the "magic numbers" in nuclear structure. *Phys. Rev.*, 75:1766–1766, Jun 1949. doi: 10.1103/PhysRev.75.1766.2. URL `http://link.aps.org/doi/10.1103/PhysRev.75.1766.2`.

[25] Maria Goeppert Mayer. On closed shells in nuclei. ii. *Phys. Rev.*, 75:1969–1970, Jun 1949. doi: 10.1103/PhysRev.75.1969. URL `http://link.aps.org/doi/10.1103/PhysRev.75.1969`.

[26] V.M. Strutinsky. Shell effects in nuclear masses and deformation energies. *Nuclear Physics A*, 95 (2):420 – 442, 1967. ISSN 0375-9474. doi: http://dx.doi.org/10.1016/0375-9474(67)90510-6. URL `http://www.sciencedirect.com/science/article/pii/0375947467905106`.

[27] J.P. Unik, J.E. Gindler, L.E. Glendenin, K.F. Flynn, A. Gorski, and R.K. Sjoblom. In *Physics and Chemistry of Fission, Vol. 2*, Vienna, 1974. IAEA.

[28] J. C. D. Milton and J. S. Fraser. TIME-OF-FLIGHT FISSION STUDIES ON U^{233}, U^{235} AND Pu^{239}. *Canadian Journal of Physics*, 40(11):1626–1663, 1962. doi: 10.1139/p62-169. URL `http://dx.doi.org/10.1139/p62-169`.

[29] R. D. Present. Possibility of ternary fission. *Phys. Rev.*, 59:466, 1941.

[30] T. San-Tsiang, R. Chastel, Ho Zah-Wei, and L. Vigneron. Sur la tripartition de l'uranium provoqué par la capture d'un neutron. *C. R. Acad. Sci.*, 223:986–987, Dec 1946.

[31] T. San-Tsiang, Ho Zah-Wei, R. Chastel, and L. Vigneron. On the new fission processes of uranium nuclei. *Phys. Rev.*, 71:382–383, Mar 1947. doi: 10.1103/PhysRev.71.382.2. URL `http://link.aps.org/doi/10.1103/PhysRev.71.382.2`.

[32] G. Farwell, E. Segrè, and C. Wiegand. Long range alpha-particles emitted in connection with fission. preliminary report. *Phys. Rev.*, 71:327–330, Mar 1947. doi: 10.1103/PhysRev.71.327. URL `http://link.aps.org/doi/10.1103/PhysRev.71.327`.

[33] J.P. Theobald. *Ph.D. Thesis, TH Darmstadt preprint IKDA 85/22*. PhD thesis, Technische Hochschule Darmstadt, Darmstadt, FRG, 1985.

[34] B. D. Wilkins, E. P. Steinberg, and R. R. Chasman. Scission-point model of nuclear fission based on deformed-shell effects. *Phys. Rev. C*, 14:1832–1863, Nov 1976. doi: 10.1103/PhysRevC.14.1832. URL `http://link.aps.org/doi/10.1103/PhysRevC.14.1832`.

[35] Ulrich Brosa, Siegfried Grossmann, and Andreas Müller. Nuclear scission. *Physics Reports*, 197 (4):167 – 262, 1990. ISSN 0370-1573. doi: http://dx.doi.org/10.1016/0370-1573(90)90114-H. URL `http://www.sciencedirect.com/science/article/pii/037015739090114H`.

[36] C. Wagemans. *The Nuclear Fission Process*. Taylor & Francis, 1991. ISBN 9780849354342. URL `http://www.crcpress.com/product/isbn/9780849354342`.

[37] H.G. Börner, F. Gönnenwein, and O. Zimmer. *The Neutron: A Tool and an Object in Nuclear and Particle Physics*. World Scientific, 2012. ISBN 9789814273084. URL `http://books.google.se/books?id=z13QS_y6ALcC`.

[38] V.A. Rubchenya and S.G. Yavshits. Dynamic treatment of ternary fission. *Zeitschrift für Physik A Atomic Nuclei*, 329(2):217–228, 1988. ISSN 0939-7922. doi: 10.1007/BF01283778. URL `http://dx.doi.org/10.1007/BF01283778`.

[39] H. Faust and Z. Bao. *Calculation of relative LCP yields in ternary fission by a Boltzmann distribution: invited paper ; Seminar on Fission, Pont D'Oye III, 1995, pp. 220-231.* 1995.

[40] Pannicke, J. IX^e Journées d'ètudes sur la fission nucléaire. Technical Report D-13, Centre d'ètudes nucléaires de Bordaux-Gradignan, Talence, 1986.

[41] J.P. Theobald, P. Heeg, and M. Mutterer. Low-energy ternary fission. *Nuclear Physics A*, 502 (0):343 – 362, 1989. ISSN 0375-9474. doi: http://dx.doi.org/10.1016/0375-9474(89)90674-X. URL `http://www.sciencedirect.com/science/article/pii/037594748990674X`.

[42] E. Piasecki and L. Nowicki. Polar emission in fission. In *Physics and Chemistry of Fission 1979 - Vol. II, Proc. of an Int. Symp., Jülich*, pages 193–221, Vienna, January 1980. IAEA.

[43] W.-D. Schmidt-Ott, F. Meissner, P. Koschel, U. Bosch-Wicke, R. Kirchner, O. Klepper, H. Folger, E. Roeckl, A. Plochocki, K. Rykaczewski, and Z. Preibisz. Neutron-rich isotope production in reactions of ^{50}Ti with $^{\mathrm{nat}}$W and ^{238}U and in fission of ^{238}U with 13 MeV/u ^{20}Ne. *Nuclear Physics A*, 522 (3–4):610 – 620, 1991. ISSN 0375-9474. doi: http://dx.doi.org/10.1016/0375-9474(91)90084-J. URL `http://www.sciencedirect.com/science/article/pii/037594749190084J`.

[44] A. Schubert, J. Hutsch, K. Möller, W. Neubert, W. Pilz, G. Schmidt, M. Adler, and H. Märten. Light charged particle release in252cf spontaneous fission: Tripartition versus fragment de-excitation. *Zeitschrift für Physik A Hadrons and Nuclei*, 341(4):481–488, 1992. ISSN 0939-7922. doi: 10.1007/BF01301393. URL `http://dx.doi.org/10.1007/BF01301393`.

[45] Yu.V. Pyatkov, V.V. Pashkevich, Yu.E. Penionzhkevich, V.G. Tishchenko, and C.-M. Herbach. Collinear tripartition of ^{248}Cm and ^{252}Cf nuclei as a probe of clustering . In *International Conference on Nuclear Physics "NUCLEAR SHELLS - 50 YEARS", 49th Meeting on Nuclear Spectroscopy and Nuclear Structure*, pages 144–150, Dubna, April 1999. World Scientific.

[46] A. V. Kravtsov and G. E. Solyakin. Search for spontaneous collinear tripartition of ^{252}Cf nuclei. *Phys. Rev. C*, 60:017601, Jun 1999. doi: 10.1103/PhysRevC.60.017601. URL `http://link.aps.org/doi/10.1103/PhysRevC.60.017601`.

[47] DV Kamanin et al. Jinr preprint 15-2007-182, 2007.

[48] K. R. Vijayaraghavan, M. Balasubramaniam, and W. von Oertzen. Collinear versus triangular geometry: A ternary fission study. *Phys. Rev. C*, 90:024601, Aug 2014. doi: 10.1103/PhysRevC.90.024601. URL `http://link.aps.org/doi/10.1103/PhysRevC.90.024601`.

[49] H. J. Krappe, J. R. Nix, and A. J. Sierk. Unified nuclear potential for heavy-ion elastic scattering, fusion, fission, and ground-state masses and deformations. *Phys. Rev. C*, 20:992–1013, Sep 1979. doi: 10.1103/PhysRevC.20.992. URL `http://link.aps.org/doi/10.1103/PhysRevC.20.992`.

[50] Peter Möller and J.Rayford Nix. Nuclear mass formula with a Yukawa-plus-exponential macroscopic model and a folded-Yukawa single-particle potential. *Nuclear Physics A*, 361(1):117 – 146, 1981. ISSN 0375-9474. doi: http://dx.doi.org/10.1016/0375-9474(81)90473-5. URL `http://www.sciencedirect.com/science/article/pii/0375947481904735`.

[51] F. Gönnenwein and B. Börsig. Tip model of cold fission. *Nuclear Physics A*, 530(1):27 – 57, 1991. ISSN 0375-9474. doi: http://dx.doi.org/10.1016/0375-9474(91)90754-T. URL `http://www.sciencedirect.com/science/article/pii/037594749190754T`.

[52] J.P. Theobald. *Ternary fission: invited paper ; Seminar on Fission, 22-23 May 1986, Château du Pont D'Oye, Haby-la-Neuve, Belgique.* 1986.

[53] M. Mutterer, P. Singer, M. Klemens, Yu.N. Kopach, D. Schwalm, P. Thirolf, A. Hotzel, M. Hesse, and F. Gönnenwein. Recent results on the ternary fission of ^{252}Cf. Fission and Properties of Neutron-Rich Nuclei: Proceedings of the International Conference, Sanibel Island, Florida, 1997. Hrsg.: J.H. Hamilton (u.a.) - Singapore: World Scientific, 1998. S. 119-130, Singapore, January 1998. World Scientific. URL `http://tubiblio.ulb.tu-darmstadt.de/13979/`. Zeichendarst. im Sachtitel teilw. nicht vorlagegemäß wiedergegeben.

[54] W. von Oertzen and A.K. Nasirov. True ternary fission, the collinear decay into fragments of similar size in the ^{252}Cf(sf) and ^{235}U(n$_{\mathrm{th}}$,f) reactions. *Physics Letters B*, 734(0): 234 – 238, 2014. ISSN 0370-2693. doi: http://dx.doi.org/10.1016/j.physletb.2014.05.067. URL `http://www.sciencedirect.com/science/article/pii/S0370269314003773`.

[55] U. Köster. Nuclear data measurements with slow neutrons at Institut Laue Langevin. In *Proceedings of the 2nd EFNUDAT workshop on Neutron Measurements, Theory and Applications*, pages 65–73, Normafa Hotel, Budapest, Hungary, September 2009. Institute of Isotopes, Hungarian Academy of Sciences.

[56] C. Sage, F. Martin, G. Kessedjian, A. Bidaud, A. Billebaud, N. Capellan, S. Chabod, O. Méplan, C. O. Bacri, X. Doligez, R. Cywinski, H. Faust, U. Köster, A. Letourneau, T. Materna, S. Panebianco, L. Mathieu, and O. Sérot. Measurements of the Mass and Isotopic Yields of the ^{233}U(n$_{\mathrm{th}}$,f) Reaction at the LOHENGRIN Spectrometer. In *Proc. of 7th International Conference on Dynamical Aspects of Nuclear Fission*, volume A paraitre, Slomenice, Slovakia, 2011. URL `http://ieeexplore.ieee.org/xpls/abs_all.jsp?arnumber=6172920`. LPSC11316.

[57] G. S. Simpson, J. C. Angelique, J. Genevey, J. A. Pinston, A. Covello, A. Gargano, U. Köster, R. Orlandi, and A. Scherillo. New information on excited states below the μs isomer in ^{136}Sb. *Phys. Rev. C*, 76:041303, Oct 2007. doi: 10.1103/PhysRevC.76.041303. URL `http://link.aps.org/doi/10.1103/PhysRevC.76.041303`.

[58] E. Moll, H. Ewald, H. Wollnik, P. Armbruster, G.Fiebig, and H. Lawin. A mass spectrometer for the investigation of fission products, int. conf. on electromagnetic isotope separators and the techniques of their applications. pages 241 – 255, Marburg, 1970.

[59] U. Köster, H. Faust, T. Materna, and L. Mathieu. Experience with in-pile fission targets at LOHENGRIN . *Nuclear Instruments and Methods in Physics Research Section A: Accelerators, Spectrometers, Detectors and Associated Equipment*, 613(3):363 – 370, 2010. ISSN 0168-9002. doi: http://dx.doi.org/10.1016/j.nima.2009.09.078. URL `http://www.sciencedirect.com/science/article/pii/S0168900209018361`. Target and Stripper Foil Technologies for High Intensity Beams Proceedings of the 24th World Conference of the International Nuclear Target Development Society.

[60] V.S. Nikolaev and I.S. Dmitriev. On the equilibrium charge distribution in heavy element ion beams. *Physics Letters A*, 28(4):277 – 278, 1968. ISSN 0375-9601. doi: http://dx.doi.org/10.1016/0375-9601(68)90282-X. URL `http://www.sciencedirect.com/science/article/pii/037596016890282X`.

[61] K. Shima, T. Ishihara, and T. Mikumo. Empirical formula for the average equilibrium charge-state of heavy ions behind various foils. *Nuclear Instruments and Methods in Physics Research*, 200(2–3): 605 – 608, 1982. ISSN 0167-5087. doi: http://dx.doi.org/10.1016/0167-5087(82)90493-8. URL `http://www.sciencedirect.com/science/article/pii/0167508782904938`.

[62] K. Shima, T. Mikumo, and H. Tawara. Equilibrium charge state distributions of ions ($Z_1 \geq 4$) after passage through foils: Compilation of data after 1972. *Atomic Data and Nuclear Data Tables*, 34 (3):357 – 391, 1986. ISSN 0092-640X. doi: http://dx.doi.org/10.1016/0092-640X(86)90010-0. URL `http://www.sciencedirect.com/science/article/pii/0092640X86900100`.

[63] G. Fioni, H.R. Faust, M. Gross, M. Hesse, P. Armbruster, F. Gönnenwein, and G. Münzenberg. Reduction of energy dispersion on a parabola mass spectrometer. *Nuclear Instruments and Methods in Physics Research Section A: Accelerators, Spectrometers, Detectors and Associated Equipment*, 332 (1–2):175 – 180, 1993. ISSN 0168-9002. doi: http://dx.doi.org/10.1016/0168-9002(93)90756-8. URL `http://www.sciencedirect.com/science/article/pii/0168900293907568`.

[64] J.P. Bocquet, R. Brissot, and H.R. Faust. A large ionization chamber for fission fragment nuclear charge identification at the lohengrin spectrometer. *Nuclear Instruments and Methods in Physics Research Section A: Accelerators, Spectrometers, Detectors and Associated Equipment*, 267(2–3): 466 – 472, 1988. ISSN 0168-9002. doi: http://dx.doi.org/10.1016/0168-9002(88)90487-1. URL `http://www.sciencedirect.com/science/article/pii/0168900288904871`.

[65] M. Hesse, H. Faust, G. Fioni, M. Groß, F. Gönnenwein, and H. Märten. Proc. Workshop on High Resolution Spectroscopy of Fission Fragments. Neutrons and γ-rays, report FZR-93-08. pages 31 –, Dresden, 1993. Rossendorf Fachinformations-Zentrum. Zentral-Inst., Rossendorf Fachinformations-Zentrum. Zentral-Inst.

[66] W.R. Leo. *Techniques for Nuclear and Particle Physics Experiments: A How-to Approach.* Springer Berlin Heidelberg, 1994. ISBN 9783540572800. URL `http://books.google.se/books?id=hDEbAQAAIAAJ`.

[67] T. Materna, A. Bail, L. Mathieu, U. Köster, H. Faust, O. Serot, and F. Michel-Sendis. Indirect identification of nanosecond isomers using the fission fragment separator LOHENGRIN. In A. Chatillon, H. Faust, G. Fioni, D. Goutte, and H. Goutte, editors, *American Institute of Physics Conference Series*, volume 1175 of *American Institute of Physics Conference Series*, pages 367–370, October 2009. doi: 10.1063/1.3258253.

[68] Bail, A., Serot, O., Faust, H., Koester, U., Materna, T., AlMahamid, I., and Kuzmina, T. E. Mass yield, isotopic yield and kinetic energy distributions for heavy masses in thermal neutron induced fission. In *Proc. of the Int. Conf. on Nuclear Data for Science and Technology*, EDP Sciences, pages 100–, April 2007.

[69] A. Bail, O. Serot, L. Mathieu, O. Litaize, T. Materna, U. Köster, H. Faust, A. Letourneau, and S. Panebianco. Isotopic yield measurement in the heavy mass region for ^{239}Pu thermal neutron induced fission. *Phys. Rev. C*, 84:034605, Sep 2011. doi: 10.1103/PhysRevC.84.034605. URL `http://link.aps.org/doi/10.1103/PhysRevC.84.034605`.

[70] F. Martin, C. Sage, G. Kessedjian, C. O. Bacri, A. Bidaud, A. Billebaud, N. Capellan, S. Chabod, R. Cywinski, X. Doligez, H. Faust, U. Koster, A. Letourneau, T. Materna, L. Mathieu, O. Meplan, S. Panebianco, and O. Serot. Measurements of the mass and isotopic yields of the ^{2}33U($\mathrm{n_{th}}$, f) reaction at the LOHENGRIN spectrometer. In *Advancements in Nuclear Instrumentation Measurement Methods and their Applications (ANIMMA), 2011 2nd International Conference on*, pages 1–7, June 2011. doi: 10.1109/ANIMMA.2011.6172920.

[71] M.A. Kellett, O. Bernillon, and R.W. Mills. The Jeff-3.1/63.1. 1 radioactive decay data and fission yields sub-libraries. Jeff report 20. NEA, 2009.

[72] T.R. England and B.F. Rider. LA-UR-94-3106. ENDF-349. Evaluation and Compilation of Fission Product Yields, 1994.

[73] Donald B. Owen. Tables for computing bivariate normal probabilities. *The Annals of Mathematical Statistics*, 27(4):1075–1090, 12 1956. doi: 10.1214/aoms/1177728074. URL `http://dx.doi.org/10.1214/aoms/1177728074`.